UNIVERSITÀ DEGLI STUDI DI MILANO

FACOLTÀ DI SCIENZE MATEMATICHE FISICHE E NATURALI
Dipartimento di Chimica Inorganica, Metallorganica e Analitica
"Lamberto Malatesta"

DOTTORATO DI RICERCA IN CHIMICA INDUSTRIALE

XXIII CICLO

ADVANCED MATERIALS: PREPARATION, STUDY AND OPTIMIZATION OF THIN FILM FOR OPTOELECTRONIC DEVICES

CHIM 03

Tutor: Prof.ssa Elena CARIATI
Co-Tutor: Dott.ssa Elena LUCENTI
Dott. Vojislav SRDANOV
Coordinatore: Chiar.ma Prof.ssa Dominique ROBERTO

Michele SCARPELLINI

Matricola R07879

Anno Accademico 2009/20010

Index

General Introduction 1

1. Introduction to OLED devices 2

1.1 History of organic electroluminescence 3

1.1.1 Advantages and disadvantages of OLEDs 3

1.1.2 Basic OLED structure and operation 5

1.1.3 "Small Molecular" OLED Devices 7

1.2 Introduction to Fluorescence 8

1.3 Introduction to non linear optics (NLO) 11

1.3.1 Basic concepts of non-linear optic phenomena 12

1.3.2 The most important quadratic or cubic NLO effects with molecular origin 15

1.3.3 Requirements of materials for significant second order NLO properties. 17

1.3.3.1 Requirement for high second order electrical susceptibilities $\chi^{(2)}$ 17

1.3.3.2 Requirements of organic molecules for significant second order (β) NLO properties 17

1.4 References 20

2 Preparation, study and optimization of thin films 21

2.1 Introduction 21

2.2 Results and Discussion 23

2.3 Conclusion 34

2.4 Experimental sections 35

2.4.1 General methods 35

2.4.2 Synthesis of 4,4'-Bis[(*p*-bromophenyl)phenylamino)]biphenyl 36

2.4.3 Synthesis of 4,4'-Bis[(*p*-allylphenyl)phenylamino]biphenyl 38

2.4.3 Synthesis of 4,4'-Bis[(*p*-trichlorosilylpropylphenyl)phenylamino]-biphenyl 40

2.4.4 Synthesis of the self-assembled monolayer 41

2.4.5 Preparation of thin TPD thin films 41

2.4.6 Instrumental 42

2.5 References 43

3 Synthesis of new fluorene derivatives as UV-Vis emitters for OLED application 44
3.1 Introduction 44
3.2 Results and discussion 47
3.3 Optical properties 50
3.4 Conclusion 54
3.5 Experimental section 55
3.5.1 General methods 55
3.5.2 Synthesis of 3,3'-dimethoxybiphenyl 56
3.5.3 Synthesis of 2-Bromo-3,5-dimethoxybiphenyl 58
3.5.4 Synthesis of 3,5-Dimethoxy-[1,1-biphenyl]-2-carboxylic Acid 60
3.5.5 Synthesis of 3,6-Dimethoxy-9-fluorenone 62
3.5.6 Synthesis of 9-(3-bromo-5-(3,9-dimethoxy-9H-fluoren-9-yl)phenyl)-3,6,9-trimethoxy-9H-fluorene 64
3.5.7 Synthesis of 1,3,5-tris(3,6,9-trimethoxy-9H-fluoren-9-yl)benzene 66
3.6 References 68

4 Synthesis and characterization of pyrene chromophores for NLO applications and optical devices 69
4.1 Introduction 69
4.2 Experimental procedure for the synthesis of pyrene derivatives 70
4.3 Conclusion 76
4.4 Experimental section 77
4.4.1 General methods 77
4.4.2 Synthesis of 4-(2-Pyren-1-yl-vinyl)-pyridine 78
4.5 References 81

5 Synthesis of new inorganic/organic hybrids with enhanced linear optical properties .. 82
5.1 Organic Cromophore: Perylene 83
5.1.1 Synthesis of perylene bisimides 84
5.2 Inorganic scaffolds: Silsesquioxanes 87
5.2.1 Definitions, Structures, and Nomenclature 88
5.2.2 Synthesis of Silsesquioxane Silanols 89
5.2.3 Mechanism of Formation of Silsesquioxane Cages and Networks 90
5.3 Inorganic/organic POSS hybrids for optoelectronics 92

5.4 Discussion of Results and Analysis 95
5.4.1 Synthesis of POSS 95
5.4.2 Synthesis of perylene bis-imides 95
5.4.3 Synthesis of Perylene-POSS hybrids 99
5.5 Conclusions 103
5.6 Experimental section 104
5.6.1 General methods 104
5.6.2 Synthesis of Octa(cyclohexylsilsesquioxane) (*c*-$C_6H_{11})_8Si_8O_{12}$ 105
5.6.3 Synthesis of *endo*-$_{C3}$-(*c*-$C_6H_{11})_7Si_7O_9(OH)_3$ 107
5.6.4 Synthesis of (*c*-$C_6H_{11})_7Si_8O_{12}$ CH=CH_2 109
5.6.5 Synthesis of Tridecan-7-one oxime 111
5.6.6 Synthesis of Tridecan-7-amine 113
5.6.7 Synthesis of *N*,*N*-Bis(1-hexylheptyl)perylene-3,4,9,10-tetracarboxylbisimide 115
5.6.8 Synthesis of *N*-(1-Hexylheptyl)perylene-3,4,9,10-tetracarboxyl-3,4-anhydride-9,10-imide 117
5.6.9 Synthesis of 2-Allyl-9-(1-hexylheptyl)anthra[2,1,9-def;6,5,10-d'e'f']diisoquinoline-1,3,8,10-tetraone 119
5.6.10 Synthesis of 2-(1-Hexyl-heptyl)-9-(4-iodo-phenyl)-anthra[2,1,9-def;6,5,10-d'e'f']diisoquinoline-1,3,8,10-tetraone 121
5.6.11 Synthesis of 2-(1-Hexyl-heptyl)-9-(4-bromo-phenyl)-anthra[2,1,9-def;6,5,10-d'e'f']diisoquinoline-1,3,8,10-tetraone 123
5.6.12 Synthesis (*c*-$C_6H_{11})_7Si_8O_{12}$-2-Propyl-9-(1-hexyl-heptyl)-anthra[2,1,9-def;6,5,10-d'e'f']diisoquinoline-1,3,8,10-tetraone 125
5.6.13 Synthesis of vynilsilsesquioxane-4-[2-(1-Hexyl-heptyl)-9-(phenyl)-anthra[2,1,9-def;6,5,10-d'e'f']diisoquinoline-1,3,8,10-tetraone] 128
5.7 References 132

General Introduction

The term “optoelectronic devices” is by now used for devices in which both electrons and photons are essential for their operation, as a natural evolution from the definitions of electronic devices that involved only electrons and holes in their operation and of photonic devices that involved only photons in their operation.

One of the new lighting technologies which emerged within the past two decades and has the potential of becoming more energy-efficient then the existing light sources, is the Solid State Lighting technology of Organic Light Emitting Diodes (OLEDs). In general, the basic OLED structure consists of a stack of fluorescent organic layers sandwiched between a transparent conducting anode and metallic cathode. When an appropriate current is applied to the device, holes are injected from the anode and electrons from the cathode; some of the recombination events between the holes and electrons result in electroluminescence (EL).

The first part of this PhD Thesis surveyed different aspect in OLED technology that are currently under debate. In particular *chapter 2* is devoted to the study, preparation and optimization of thin films between the organic hole transport layer and the anode surface while *chapter 3* deals with the synthesis of trifluorene compound, with methoxy substituents, as possible UV-blue emitter.

The second part of this PhD work is dedicated to the synthesis and study of new materials with interesting emissive and second order NLO properties. In particular pyrene based chromophores are investigated in *chapter 4*, while *chapter 5* deals with the synthesis of organic-inorganic perylene-POSS hybrids with enhanced emissive properties.

1. Introduction to OLED devices

The available data about OLEDs and technical projections indicate that the amount of energy needed to generate the same amount of light can be eventually reduced by up to 50%. If the consumption of electric energy used for lighting is reduced by the desired 50%, the savings to the society would amount to approximately $25B per year[1]. In addition to the savings, less consumed energy would amount to less produced energy and, consequently, less pollution of water and air. According to the latest estimates, the use of electricity may be reduced by 50% by the year 2020, sparing the atmosphere some 45 million tons of carbon emissions annually. The potential savings also depends on how quickly and to what extend these developments occur[2]. This study also indicates that it is primarily the price breakthrough that will facilitate the market penetration of the new sources of light. In other words, even though the technological advances may lead to significant reduction of energy, the market will not accept SSL unless the cost is reduced as well. If SSL achieves a price breakthrough, far more energy will be saved.

The Lighting industry has been dominated by incandescent light bulbs until recently and only in the past few years fluorescent lamps started being used in residential and commercial sector.

OLEDs are unconventional, large area thinfilm, nearly two-dimensional devices. They are diffused light sources, distinctly different from point sources such as light bulbs. Also, OLEDs will operate at very low voltages, of the order of 3-5 V. Therefore, the introduction of OLEDs as sources of light for general lighting applications will cause a major paradigm shift in the lighting industry. Not only a new lighting infrastructure will be required, but also many new jobs will be created. While significant research is still needed, OLEDs will soon achieve the efficiency to compete directly with incandescent sources (light bulbs). Experimental OLEDs are already more energy-efficient than incandescent lamps. The luminous efficiency of light bulbs is about 13-20 lm/W but the latest experimental greenemitting OLEDs already have luminous efficiency of 76 lm/W, albeit at low luminances[3]. The development is on track for OLEDs to effectively compete even with fluorescent lamps, which have the luminous efficiency of 50-100 lm/W.

1.1 History of organic electroluminescence

The first EL from a an organic molecule, anthracene, was reported by Pope and coworkers in 1963[4]. They reported EL from a thick anthracene crystal (10μm-5mm), when a bias of several hundred volts was applied across it. The achievement did not stimulate much interest as the applied bias was very high. However, Vincent *et al*[5] achieved bright blue EL from vacuum-deposited 0.6 mm thick anthracene crystal films with an applied bias of less than 100V. The breakthrough was achieved by Tang and VanSlyke in 1987[2], who made a bilayer structure by thermally evaporating the small molecular weight organic materials, N,N'-diphenyl-N,N'-bis(3-methylphenyl)1,1'-biphenyl-4,4'diamine(TPD) and tris(8-hydroxyquinoline)aluminum (Alq3) to achieve a total thickness of ~100 nm. They achieved a very bright green emitting OLED with a brightness higher than 1000 cd/m2 and an external quantum efficiency of ~1% when a low bias of 10V was applied across the structure[1]. Following this achievement Adachi *et al*.[6] al succeeded in fabricating stable multilayer devices by inserting hole and electron transport layers between the two electrodes. In 1989, Tang *et al.*[2] al developed a laser-dye doped Alq3 multilayer structure, in which the fluorescent efficiency was improved and the emission color varied from the original green to the dopant emission color. Following the success of fabricating small molecular OLEDs, Burroughs et al[7] discovered the first polymer LED (PLEDs) by spin coating a precursor polymer of the luminescent poly-(para-phenlene vinylene) (PPV) onto a indium tin oxide (ITO) coated glass. Compared to small molecular devices, polymer light emitting devices (PLEDs) have several potential advantages, *e.g.* , fabrication by spin coating[9,8] or inkjet printing[9] from solutions and subsequent thermal treatment. Fluorescent emission of singlet excitons are the main mechanism of OLED light emission. As the probability of forming spin singlet states and spin triplet states are 25% and 75% respectively, the ideal maximum fluorescent yield is, therefore, limited to 25% by spin statistics. To overcome this theoretical limit Baldo *et al*[10] fabricated and demonstrated phosphorescent OLEDs, by doping phosphorescent molecules, where the EL is due to triplet emission, into a fluorescent host layer.

1.1.1 Advantages and disadvantages of OLEDs

OLEDs are already commercialized and they are making ways to the display markets. Currently OLEDs are used in low information displays with limited size such as mobile

phones, MP3 players, digital cameras and some laptop cameras. The driving force behind this success is some advantages that the OLEDs enjoy.

Advantages

Self-luminous: The efficiency of OLEDs is better than that of other display technologies without the use of backlight, diffusers, and polarizers.

Low cost and easy fabrication: Roll-to-roll manufacturing process, such as, inkjet printing and screen printing, are possible for polymer OLEDs.

Color selectivity: There are abundant organic materials to produce blue to red light.

Lightweight, compact and thin devices: OLEDs are generally very thin, measuring only ~100nm.

Flexibility: OLEDs can be easily fabricated on plastic substrates paving the way for flexible electronics.

High brightness and high resolution: OLEDs are very bright at low operating voltage (White OLEDs can be as bright as 150,000 cd/m2).

Wide viewing angle: OLED emission is lambartian and so the viewing angle is as high as 160 degrees.

Fast response: OLEDs EL decay time is < 1us.

Disadvantages

Highly susceptible to degradation by oxygen and water molecules: organic materials are very sensitive to oxygen and water molecules which can degrade the device very fast[11]. So the main disadvantage of an OLED is the lifetime. With proper encapsulation, lifetimes exceeding 60,000 hours have been demonstrated.

- Low glass transition temperature Tg for small molecular devices (>70°C). So the operating temperature cannot exceed the glass transition temperature.
- Low mobility due to amorphous nature of the organic molecules.

1.1.2 Basic OLED structure and operation

The OLED structure is similar to inorganic LEDs: an emitting layer between an anode and a cathode. Holes and electrons are injected from the anode and cathode; when the charge carriers annihilate in the middle organic layer, a photon is emitted. However, there is sometimes difficulty in injecting carriers into the organic layer from the usually inorganic contacts. To solve this problem, often the structure includes an electron transport layer (ETL) and/or a hole transport layer (HTL), which facilitate the injection of charge carriers. All of these layers must be grown on top of each other, with the first grown on a substrate (see Figure 1.1).

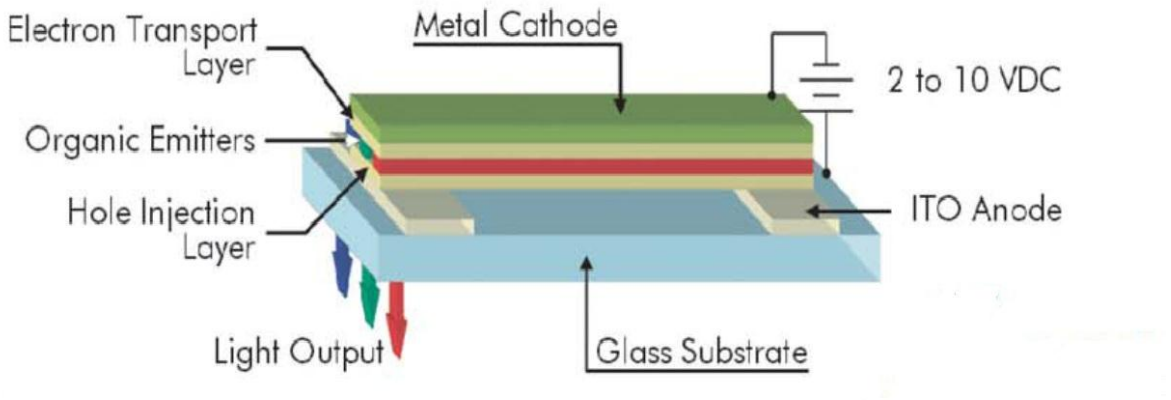

Figure 1.1

There are many choices of materials for each layer, depending upon the application. The substrate is usually glass but may also be made of Polyethylene for a flexible device or even a thin metal foil for a flexible yet protective and durable layer. The anode is usually transparent ITO but may be —for example—porous polyaniline, and the cathode is often calcium or another low work function metal. The anode, of course, must be transparent so that the emitted photons can exit the device. Example materials of ETL and HTL are Alq3 and TPD, respectively (Scheme 1). Small molecular organic materials are normally thermally evaporated and polymers are spin coated on a transparent ITO coated glass substrate to a thickness of about 100 nm in case of small molecular OLEDs. When a forward bias is applied to this structure, holes (h+) are injected from the anode and the electrons (e-) are injected from the cathode. These injected carriers recombine, form excitons and some of them decay radiatively to give the EL. Thus, for injection EL the fundamental physical processes include carrier injection, transport, recombination and radiative exciton decay. Normal operating voltage is about 2-20 V, corresponding to average electric field of 0.1-2 MV/cm, which is

very high compared to the typical fields ~10 kV/cm of inorganic semiconductor devices. The resistivity ρ of the devices ranges over eight order of magnitude, with very high values of 105-1013 Ω.cm in forward bias. In reverse bias, ρ is also very high (109 Ω.cm). The ITO, a wide band gap (Eg = 3.5-4.3 eV) semiconductor, is composed of indium oxide (In_2O_3) and a small amount of tin oxide (SnO_2) (~5 wt%). Most OLEDs use ITO as the anode due to its relatively high work function and high transparency (90%) to visible light. The conductance and transparency of ITO are mostly dependent on the film thickness and composition ratio of two components. The resistivity of a 200 nm thick ITO is about 10-3 Ω.cm with mobility μ ~ 10 cm^2/V_s. With increased ITO thickness the conductance increases, but the transparency decreases. Another very important parameter is its work function (Φ_0) or Fermi energy (E_f) relative to the organic materials. Because the highest occupied molecular orbital level (HOMO) energies of organic materials are typically E_{HOMO} = 5-6 eV, a high Φ_0 is needed for the anode to efficiently inject holes to the organic layers.

For the cathode, low work function materials such as Ca (Φ_0 ~3 eV), Mg (Φ_0 ~3.7 eV), Al (Φ_0 ~4.3 eV) are used to minimize the energy barrier for e- injection from E_f of the cathode to the lowest unoccupied molecular orbital (LUMO) level of organic materials. The problem of many low work function metals is extreme reactivity to oxygen and water, hence Ca and Mg should be protected by an additional layer, such as Al. Another way to minimize the barrier from electron injection is to insert a very thin (~1 nm) insulating layer of LiF, CsF or AlOX between the top organic layer and the Al cathode. These buffer layers generate a dipole layer and thus reduce the barrier for electron injection to the organic layers. The hole and electron transport layers (HTL and ETL, respectively) are the layers favorable for hole and electrons respectively. When the applied bias V_{app} is less then the built in voltage V_{bi}, the injected current is negligible and most of the current is caused by free carriers in the organic layers or leakage current. At high forward applied field the injected holes and electrons hop from site to site through the organic layers. Some of the carriers may accumulate in a specific area, called the charge accumulation zone, usually at the organic-organic interface of the multi-layer structure. If the density of electrons and holes are sufficiently high, then the distance between them becomes sufficiently low for recombination to radiative singlet excitons (SEs).

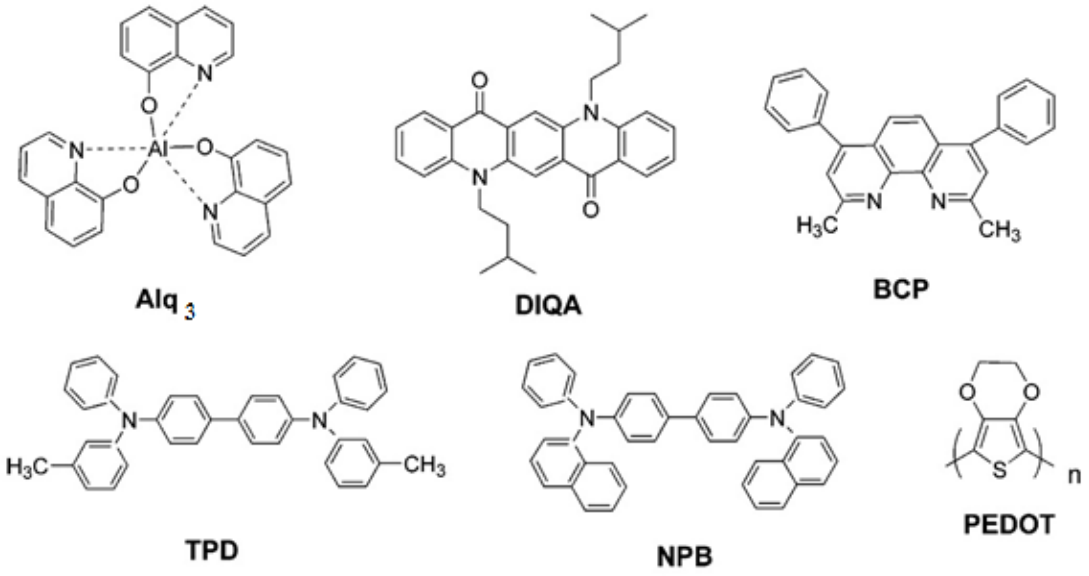

Scheme 1.2 Structures of Multilayer OLED Constituent Materials: TPD, NPB, and PEDOT (HTL), Alq3 (ETL), DIQA (Dopant), and BCP (ETL)

1.1.3 "Small Molecular" OLED Devices

As the name indicates, the active components are "small" molecules. These small molecules are deposited by vapor deposition. Most "small molecules" would crystallize when deposited from solutions and crystallization would damage the device performance. Also, solution coating may result in uncontrollable mixing of layers. Most of the hole-transport small molecules, for example TPD, contain one or several aromatic amine groups (a key pre-requisite for hole transport) and a variety of pendant substituents. These molecules have a low oxidation potential and must form stable cation-radicals. Electron transport molecules are typically complexes of a metal such as aluminum (*i.e* Alq3), boron, etc. with aromatic groups, bisbiphenyl anthracene[12]. These molecules have a relatively high electron affinity and must form stable anion-radicals. Also, there is a need to fabricate the devices with extremely uniform thicknesses of each layer. Nonuniformities may lead to localized surges of electric current, localized overheating, and gradual destruction of the device.

1.2 Introduction to Fluorescence

All molecules absorb light. However, only a relatively low number of molecular species (usually rigid conjugated polyaromatic hydrocarbons or heterocycles) emit light as a result of absorption of light from some other sources. If the emission is immediate or from the electronically excited singlet state, the phenomenon is called fluorescence. Fluorescence is named after the mineral fluorite, composed of calcium fluoride, in which this phenomenon was observed. Fluorescent effects have been observed for thousands of years. In 1852 the true science of fluorescence was brought to light by Sir George Stokes[13]. He applied the scientific method to fluorescence and developed the "Stokes Law of Fluorescence", which dictates that the wavelength of fluorescence emission must be greater than that of the exciting radiation. Fluorescence is the emission of light from a molecule in which an electronically excited state has been populated. The emission of the light is usually in the ultraviolet to visible portion of the spectrum, sometimes in the near-infrared. The phenomenon can be illustrated by a simple electronic state diagram called Jablonski diagram:

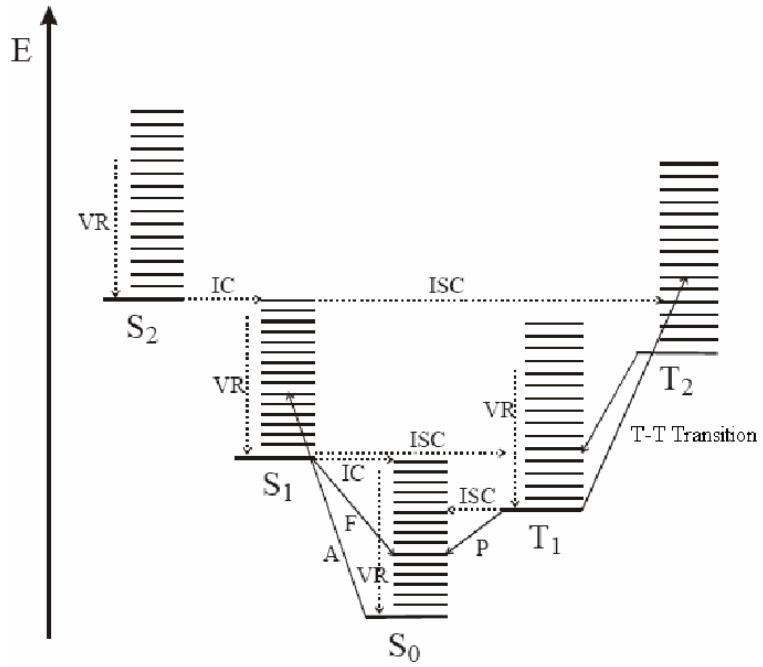

Figure 1.3: Jablonski-Diagram of different monomolecular deactivation. (dotted line transition: radiation less process, solid line transition: radiating process; A = Absorption, F = Fluorescence, P = Phosphorescence, IC = Intercrossing, ISC = Inter system crossing, VR = Vibrational Relaxation.

The electronic and vibrational energy levels of the fluorophore are represented by horizontal lines and grouped in bands. The lowest band is associated with the ground electronic state, S_0. The lowest energy level of the excited singlet state is represented by S_1, whereas T_1 is the

lowest level of the excited triplet state. Upon excitation, fluorophores in ground state absorb a photon and jump to higher vibrational energy levels of the electonically excited singlet state, shown as absorption of light, A. The photon of excitation is supplied by an external source, such as an *incandescent* lamp or a laser. The transition from S_0 to higher excited levels of S_1 is responsible for the visible and ultraviolet absorption spectra observed for fluorophores. The absorption of photon is highly specific and it takes place in about 10-15 seconds.

Excitation is followed by a return to the lower vibrational levels of the electronically excited state. This relaxation occurs in about a picosecond. The excited state itself exists for a finite time. Typical values of excited-state lifetimes are in the range of nanoseconds. From the singlet state, the fluorophore returns to the electronic ground state with the emission of the photon, shown as fluorescence F, but to higher vibrational levels of this state. In fluorescence emission, the spin multiplicities of the ground and excited states are the same. One can measure either a steady state spectrum of emitted light or the actual decay kinetics of emission. Photoemission is unimolecular. It is a first order process in the concentration of the excited state. The energy of the photon that is emitted as the electron decays to the ground state depends on the energy difference between the excited and ground state at the time of emission. The rapid decay of excited vibrational states implies that the state from which the fluorophore decays is independent of the excitation wavelength. However, the state to which the fluorophore decays is not always the lowest vibrational state of the ground state, but it is an equilibrium distribution of vibrational levels. Therefore, the emission spectra of fluorescent molecules show fine structure. The probablility of decay from the excited state to each vibrational level of the ground state is what determines the shape of the fluorescence spectrum. Especially in rigid molecules like perylene, the fluorescence spectrum is more or less the mirror image of the absorption spectrum. The symmetry equilibrium is due to the vibrational frequency of the excited energy levels and the ground state that remain similar in fluorescence bands which actually determine the fine structure of the absorption bands. Further, the fluorescence and the absorption both exhibit comparable intensities.

An important term in fluorescence is quantum yield. The fluorescence quantum yield describes the efficiency of the fluorescence process. It is defined as the ratio of the number of photons emitted to the number of photons absorbed. The maximum fluorescence quantum yield is 1.0 (100%); every photon absorbed results in a photon emitted. Compounds with quantum yields of 0.10 are still considered quite fluorescent. In rigid molecules, there are only small differences in the geometry equilibrium between the ground state and the excited state. This results in very small Franck-Condon-Factors for radiation less transition and so the inter

conversion will be very slow. As a result, the total excitation energy will be emitted as fluorescence with high intensity so that the quantum yield will be increased. Thus the quantum yield is related with the intensity of the emission and partially related with the life time of the excited state too. The fluorescence lifetime refers to the average time the molecule stays in its excited state before emitting a photon.

1.3 Introduction to non linear optics (NLO)

NLO-linear optics represents optical phenomena, caused by the interaction of an oscillating electromagnetic field (light) with specific molecules or bulk materials, with emission of a new electromagnetic field (new light), which differ particularly not only in frequency, but also in phase or other optical properties from the incident ones. In general, a NLO phenomenon results from a strong interaction between light and material and so the first observations of NLO phenomena are subsequent to the laser development. In the last decades, the research has been widely developed, due the possibility to generate potentially interesting new NLO materials for optical and electro-optical device.[14] Generally, the NLO processes can be classified in two principal categories:

a) Phenomena with frequency conversion: in these processes the interaction of the electromagnetic radiation with the NLO material produces a variation of the frequency of a part of output radiation respect to incident radiation. The frequency of this new radiation is a multiple of the incident radiation frequency.
b) Phenomena with the modulation of the refraction index due to the effect of a strong and external electric field: the interaction of a laser radiation with a NLO material, in the presence of electric field which produces a variation of the refraction index of the material, can modulate the velocity of the laser propagation, but not its frequency.

When the applied field is an *electric* field, we can talk about electro-optic effects (optoelectronics); if it is optic or electromagnetic, and so associated to a strong bright radiation, we can talk about optic-optic effects (photonics). In general the radiation is a very strong laser, which can modify the electric and optical properties of a material. In conclusion, the opto-electronic phenomena are referred to a system, in which the material is crossed by a laser radiation while it is also perturbed by a strong external electric field. In the photonic phenomena, instead, the electric field applied is substituted by an electromagnetic field of a strong laser radiation. The photonic phenomena represent the new technology in which the photons, but not the electrons, are used to transfer, to obtain and to analyze data and information with a very high velocity of light respect to the velocity of the electric phenomena. Moreover, the photonic devices are advantageous, because they can also exploit the high frequency, the wide wavelength range and so the available energies of the electromagnetic radiation.

1.3.1 Basic concepts of non-linear optic phenomena

When a bulk material experiences an oscillating external field, there is a perturbation of its electrons and therefore of its polarity, expressed by Eq. (1)[15]:

$$\vec{P} = \vec{P}_0 + \vec{P}_{ind} = \vec{P}_0 + \chi^{(1)}\vec{E} \qquad \text{Eq. (1)}$$

where $\vec{P}_0$ is the intrinsic polarity, $\vec{P}_{ind}$ is the induced polarization and $\chi^{(1)}$ the electrical susceptibility or linear polarizability tensor. If the applied electric field strength $\vec{E}$ is very high, as it happens in the case of laser pulses, the perturbation is not anymore linear with respect to the electric field and the induced polarization is better expressed by a power series according to Eq. (2):

$$\vec{P} = \vec{P_0} + \chi^{(1)}\vec{E} + \chi^{(2)}\vec{E^2} + \ldots\ldots\ldots\ldots + \chi^{(n)}\vec{E^n} \qquad \text{Eq. (2)}$$

where $\chi^{(2)}$, $\chi^{(3)}$ and $\chi^{(n)}$, which are tensors, are, respectively, the second-, third- and *n*-order electrical susceptibilities, which correspond to non-linear responses of the bulk material. When $\vec{E}$ is relatively low, the perturbation of the electrons can be explained as a simple linear harmonic displacement, but, when $\vec{E}$ is very strong, the perturbation or the polarization of the electronic density is not linear and therefore anharmonic. From the graphic point of view, the perturbation, induced by the electric field $\vec{E}$, can be represented with different diagrams. In fact, if the electric field strength is relatively low, the induced polarization, $\vec{P}_{ind}$, is proportional to the field applied $\vec{E}$ and it can be expressed only as a function of the susceptibility $\chi^{(1)}$(figure 1.3), ignoring the terms which depend on E^2 or E^3:

$$\vec{P}_{ind} = \chi^{(1)}\vec{E} \qquad \text{Eq. (3)}$$

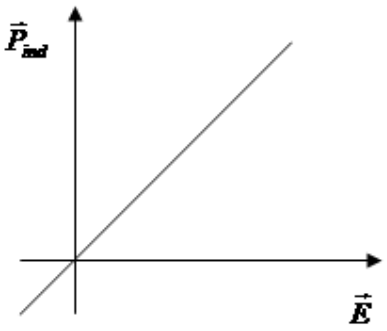

Figure 1.3 Weak electric field applied.

In this case the response is linear and the material has a linear optic behavior. When the electric field applied, $\vec{E}$, is very strong the induced polarization in the material has not a linear response and it can be represented by the diagrams reported in figures 1.4a e 1.4b:

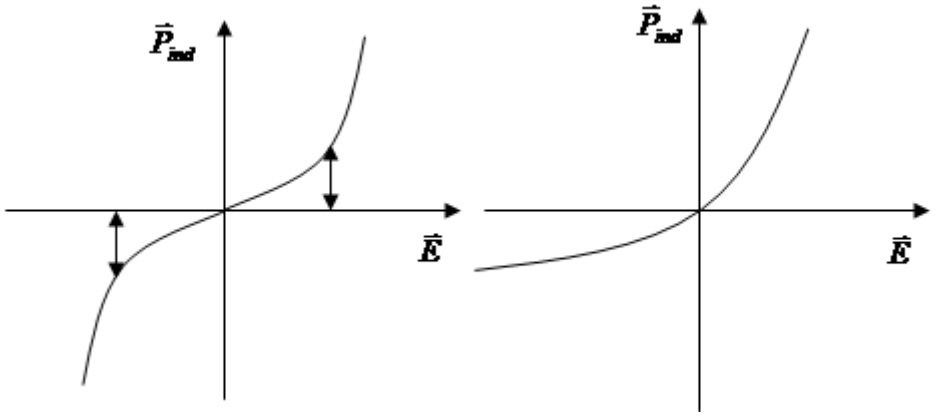

Figure 1.4a and 1.4b. Strong electric field applied in centrosymmetric (**1b**) and noncentrosymmetric (**1c**).

This non-linear optical response is associated with strong electric field $\vec{E}$, such as laser radiation, in fact:

$$\vec{E}_{laser} \geq 10^3 \, V/cm \tag{1.4}$$

This value is enough to perturbed the electronic system of a material or a molecule, which is subject to a value of microscopic and atomic electric field of the order of 108 - 109 V/cm. In this way the laser perturbs, but it cannot ionize or damage the material. When n increases, the $\chi^{(n)}$ values decreases in considerable way, since the efficiency η of a non-linear process is given by:

$$\eta \approx 1/\lambda_{laser} \left(\vec{E}_{laser} / \vec{E}_{atomic} \right)^{n-1} \tag{1.5}$$

Since $\vec{E}_{atomic} > \vec{E}_{laser}$, for the greatest part of the materials the effects of the more third order are not observable, because they have a low efficiency and so, generally, they are ignored. When a material is polarized, from the electric point of view three terms of susceptibility can be considered:

$\chi^{(1)}$ or linear

$\chi^{(2)}$ or quadratic or first order NLO effect

$\chi^{(3)}$ or cubic or second order NLO effect

In the fig. 1.4a the induced polarization of a centrosymmetric material is reported: in fact the polarization in $+\vec{E}$ direction (that is $[\vec{P}_{ind}(+\vec{E})]$) is identical, but with contrary sign respect to the polarization in $-\vec{E}$ direction (that is $[\vec{P}_{ind}(-\vec{E})]$). The same effect is obtained when the field is inverted. Therefore, in a centrosymmetric material the terms of susceptibility of odd order ($\chi^{(2)}$, $\chi^{(4)}$, ...) must be equal to zero so that $\vec{P}_{ind}(+\vec{E}) = \vec{P}_{ind}(-\vec{E})$. In particular a value of $\chi^{(2)}$, different from zero, is attributed to non-centrosymmetric materials. When atoms or molecules are considered the Eq. (2) can be substituted by Eq. (4):

$$\vec{P} = \mu_0 + \alpha\vec{E} + \beta\vec{E}^2 + \gamma\vec{E}^3 + \ldots\ldots\ldots\ldots \qquad \text{Eq.(4)}$$

with:

μ_0: molecular ground state static electric dipole moment

α: first order polarizability

β: second order polarizability or first order (quadratic) hyperpolarizability

γ: third order polarizability or second order (cubic) hyperpolarizability

Because of the anisotropy, these quantities are tensors with nine terms of increasing order (correspondent respectively to 9, 27, 81 elements). To connect $\chi^{(1)}$ to α, $\chi^{(2)}$ to β etc., it is assumed that the atoms or molecules in a material are independently polarized by $\vec{E}$, without interatomic or intermolecular coupling (joining). As a consequence of this approximation it can be reported that:

$$\chi^{(1)} = \Sigma\,\alpha$$

$$\chi^{(2)} = \Sigma\,\beta$$

$$\chi^{(3)} = \Sigma\,\gamma$$

The NLO response observed for a single molecule depends on, when working with the same applied field, non-linear coefficients, generated by the properties of its electronic structure. At molecular level, such as in the case of the materials, the NLO coefficients of odd order (for example β) are zero for centrosymmetric structures, because in absolute value $\vec{P}_{ind}(+\vec{E}) = \vec{P}_{ind}(-\vec{E})$. In these cases the first non- linear term different from zero is γ. Instead, the non-centrosymmetric molecules have all nonlinear terms and the first is β.

Moreover, it is important to underline that usually the non-linear coefficients have very low values. Therefore, to obtain significantly NLO effects, it is necessary that β and γ (or $\chi^{(2)}$ and $\chi^{(3)}$) are not too much low. This involves, for example, that the order of magnitude for $\chi^{(2)}$ is at least $5 \cdot 10^{-8}$ esu and for $\chi^{(3)}$ at least $3 \cdot 10^{-15}$ esu (esu is the electrostatic unity of the non-linear

susceptibility. 1 esu = 1 cm/statvolt; 1 volt = 1/299, 8 statvolt). For β e γ the limit order of magnitude are respectively 10^{-30}esu and 10^{-34} esu .

1.3.2 The most important quadratic or cubic NLO effects with molecular origin

The optical phenomena induced by β and γ can be used to obtain different optic effects either in some properties such as the frequency or in the intensity (usually the second order effects are higher in intensity respect to the third order effects).
Generally the second order NLO effects (or quadratic) are due to a mixing of three waves: two incident waves with frequency ω (or ω_1 and ω_2) interact with the molecule (characterized by a known value of quadratic hyperpolarizability β) to generate a new wave, SHG, Second Harmonic Generation, if the frequency is 2ω, or SFG (Sum Frequency Generation), if the frequency is $\omega_1 + \omega_2$ (the minus sign is a convention):

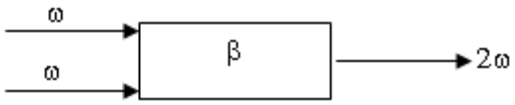

β(−2ω; ω, ω)

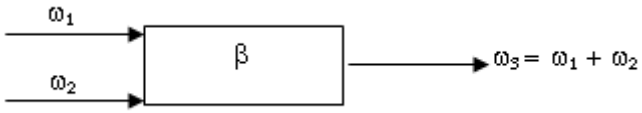

β(−ω3; ω1, ω2)

Moreover there is another effect, that is an elision without emission of radiation (Optical Rectification):

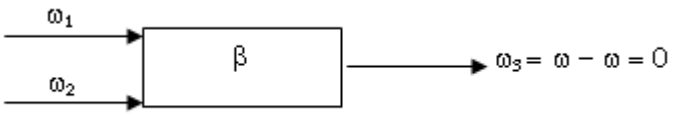

β(0; ω, ω)

This last phenomenon corresponds to a simple fixed polarization of the material. If the properties of the polarization, induced from the interaction of the molecule with the electromagnetic field (that is a variable electric field with frequency ω), are analyzed with the Fourier method, a periodic trend, constituted by three components, can be evidenced:

• a component with frequency ω (linear polarization);

• component with frequency 2ω (second order polarization, produces SHG);

• a component with frequency 0 (fixed polarization that produces Optical Rectification)

In the case of third order NLO effets (or cubic) there is a mixing of four waves: three incident waves with frequency ω (or ω_1, ω_2 and ω_3) interact with the molecule (characterized by a certain value of cubic hyperpolarizability γ) to emit a new wave, THG (Third Harmonic Generation), if the frequency is 3ω and FWSM (Four Wave Sum Mixing) if the frequency is $\omega_1+\omega_2+\omega_3$ or more complex emissions of the type SFG (Sum Frequency Generation):

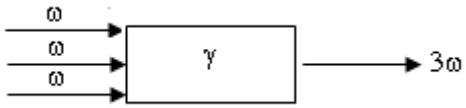

THG $\gamma(-3\omega; \omega, \omega, \omega)$

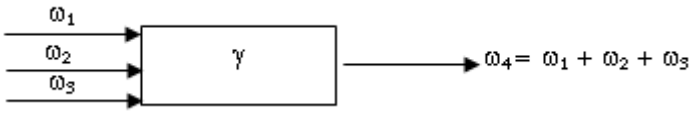

FWSM $\gamma(-\omega_4; \omega_1,\omega_2, \omega_3)$

It is evident that the interaction at molecular level occurs between the incident laser radiation (or more incident laser radiation) and a solution of the molecule in a solvent without important NLO properties. To have measurable NLO phenomenon it is important that the concentration of the molecule is sufficiently high. Obviously, the interaction occurs also when the molecule is at gaseous state, but when its partial pressure is sufficiently high to give measurable NLO response.

1.3.3 Requirements of materials for significant second order NLO properties.

1.3.3.1 Requirement for high second order electrical susceptibilities $\chi^{(2)}$

A non-centrosimmetric crystalline structure is the main requirement to have a NLO-active material. However, centrosymmetric polarizable molecules can crystallize with a noncentrosymmetric packaging and so crystals (and also the material deriving from these molecules) can show second order NLO properties. These properties may be significant when in the crystalline architecture of low symmetry there are charge transfers between molecule and molecule (this corresponds to a push-pull process, that is an intermolecular charge transfer).

The acentricity requirement constitutes a major impediment when we attempt to engineer materials with large $\chi^{(2)}$ because about 75% of organic molecules crystallizes in centrosymmetric space groups. Same strategies to overcome this issue have been developed in the last years:

- introduce chiral groups in the molecule;
- use hydrogen bond to drive crystallization;
- introduce steric hindrance groups;
- use ionic chromophores.

1.3.3.2 Requirements of organic molecules for significant second order (β) NLO properties

From a molecular point of view, in the last years the research has shown some essential criterions in order that the molecule has a quadratic hyperpolarizability (β) value different from zero.[16,17,16] In particular the molecule:

1) must be polarizable (for example with a wide π electronic conjugation);
2) must have an asymmetric charge distribution (that is a push-pull system with charge transfer);
3) must have one or more excited states energetically similar to the energy of the fundamental state with a significant charge transfer;
4) must have a great difference between the ground and excited state dipole moment.

The effect of these characteristics may be better understand considering the approximate expression for the calculation of β proposed by Oudar[17]. In his model Oudar considers that the direction of the excitation is the same of the charge transfer between two energetic levels of a

push-pull molecule. So the hyperpolarizabiliyt is called β_{CT} and it may be calculate as reported below:

$$\beta_{CT} = \frac{3e^2}{2} \cdot \frac{h\varpi_{eg} f \Delta\mu_{eg}}{[(h\varpi_{eg})^2 - (2h\varpi)^2][(h\varpi_{eg})^2 - (h\varpi)^2]}$$

where:

$h\varpi_{eg}$ is the energy of the charge transfer transition

$h\varpi$ is the energy of the laser radiation used in the experiment

f is the oscillator's strength of the CT equal to the integral of the absorption coefficient of the CT as reported below

$$\int_{\varpi_2}^{\varpi_1} \varepsilon_{CT}\, d\varpi$$

$\Delta\mu = \mu e - \mu g$ is the difference of dipole moment between the excited and ground state.

Some inorganic compounds such as $LiNbO_3$ and KH_2PO_4 give crystals with interesting second order NLO properties. In spite of this, in the last twenty years many studies have been dedicated to the second order NLO properties of organic structures. These researches are motivated from many factors, for example:

• organic materials cost is lower than inorganic materials;

• organic materials show high NLO properties and more quick responses;

• there is a great flexibility for organic structures and so tailor made molecular structure may be created.

The basic idea is to obtain a more π−delocalized system (known as spacer), many times more polarizable thanks to the presence of heteroatoms (S, Se …), able to separate electrondonor groups (D) from electron-withdrawing groups (A). This system is known as push-pull system.

A typical push-pull system is reported below:

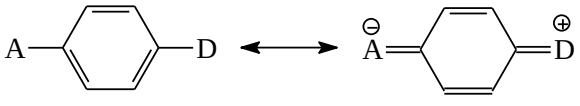

(A = electronwithdrawing group, D = electrondonor group)

where in the excited state there is a strong charge transfer between donor and acceptor through the π organic polarizable system. Experimentally in the organic system it has been found that the β value increases when the lenght of the π conjugation system also increases and it depends on the nature of the electronic nature of the spacer. In particular, the conjugated double bond is better than triple bond and phenyl group about the capacity to transfer charge from electrondonor group to electronwithdrawing group. The intensity of the NLO effect also depends on the conjugation efficacy, controlled by the lenght and the type of the spacer, that is between donor D and acceptor A.

1.4 References

[1] Brodrick J. R., OIDA OLED Workshop, April 5, 2002; Source: U.S. Lighting Market Characterization, Volume I – Lighting Inventory and Energy Consumption Estimate, Draft for Review, Arthur D. Little, Arlington, VA., March 5, **2002**.

[2] Kendall M. and Scholand M., "Energy Savings Potential of Solid State Lighting in General lighting Applications" A.D.Little, Inc., Prepared for U.S. Department of Energy.

[3] Jabbour G., University of Arizona, OIDA OLED Workshop, April 5, **2002**.

[4] Pope M., Kallmann H. P., *Chem. Phys*. 1963, *38*, 2042; Sano M., Pope M., Kallman H., *J. Chem. Phys.* **1965**, *43*, 2920.

[5] Vincentt P. S., Barlow W. A., Hann R. A., and Roberts G. G., *Thin Solid Films*, **1982**, *94*,171.

[6] Adachi C., Tokito S., Tsutsui T., and Saito S., *J. Appl. Phys.*, **1988**, *27*, L269; Adachi C., Tokito S., Tsutsui T., and Saito S., *J. Appl. Phys*. **1988**, *27*, L713.

[7] Burroughes J. H.,. Bradley D. D. C, Brown A. R., Marks R. N., Mackay K., Friend R. H., Burns P. L., and Holmes A. B., *Nature* **1990**, *347*, 539.

[8] Hotta S. and Waragai K., *Adv. Mater.* **1993**, *5*, 896.

[9] Garnier F., Hajloui R., Yassar A., and Srivastava P., *Science* **1994**, *265*, 1684; Hebner T. R., Wu C. C., Marcy D., Lu M. H., and Sturm J. C., *Appl. Phys. Lett*. **1998**, *72*, 519; Bharathan J. and Yang Y., *Appl. Phys. Lett.* **1998**, *72*, 2660.

[10] Baldo M. A., O'Brein D. F., You Y., Shoustikov A., Sibley S., Thompson M. E., Forest S. R., *Nature* **1998**, *395*, 151; Adachi C., Baldo M. A., Thompson M. E., and Forrest S. R., *J. Appl. Phys.* **2001**, *90*, 5048.

[11] Sugiyama K., Ishii H., Ouchi Y., and Seki K., *J. Appl. Phys*. **2000**, *87*, 297.

[12] Murata H., Kafafi Z. H., Uchida M., *Appl. Phys. Lett.* **2002**, *80*, 189.

[13] Prof. Dr. Valeur B., *Molecular Fluorescence,* **2001** Wiley-VCH Verlag GmbH.

[14] Blanchard-Desce M., Murder S.R., Barzoukas M., in *Comprehensive Supramolecolar Chemistry,* D.N. Reinhoud Ed., Pergamon, **1996**.

[15] a) Long N.J., *Angew. Chem. Int. Ed. Eng.*, **1995**, *34*, 21. b) Andrè J.M., Delhalle J., *Chem. Rev.*, **1991**, *91*, 843. c) Nalwa H.S., *Appl. Organomet. Chem.*, **1991**, *5*, 349

[16] Kanis D.R., Ratner M.A., Marks T.J., *Chem. Rev.*, **1994**, *94*, 195

[17] Oudar J.L., *J. Chem. Phys.*, **1977**, *67*, 446

2 Preparation, study and optimization of thin film

2.1 Introduction

By and large the field of organic optoelectronics is fueled by a demand for mass-production of inexpensive solid-state lighting and photovoltaic devices. Such devices utilize thin organic films deposited either by sublimation or by spin-coating from solution. Both processes are conducted far from thermodynamic equilibrium hence yielding metastable amorphous thin films. In such films the non-covalent interactions are comparable in energy to thermal fluctuations and thus can lead to morphological and structural changes driven by the minimization of Gibbs energy. The inherently low glass transition temperature, Tg, of many organic solids may be further depressed in thin organic films[1], which makes those susceptible to morphological and structural changes. These include spontaneous dewetting and an amorphous-to-crystalline phase transformation that may occur even at an ambient temperature. The spontaneous changes in the thin film structure or morphology are difficult to control, yet those can adversely affect performance of an organic optoelectronic device.

Although considered generally as a nuisance, a spontaneous dewetting in organic thin films can be used to create patterned surfaces for advanced technological applications[2]. Similarly, an amorphous-to-crystalline phase transformation can be detrimental to an organic light emitting diode (OLED)[3], yet it may improve performance of an organic photovoltaic (OPV) device[4]. The reason for the latter is a much higher mobility of charge carriers in crystalline matter when compared to an amorphous material of the same kind. The low carrier mobility in amorphous organic materials is compensated in OLEDs by the presence of large electric fields, but not in OPVs where such fields are absent. A considerable attention has been given to the morphology and the size of the crystalline domains in OPVs and to the formation of their percolative pathways required for extraction of photo-generated charge carriers[5]. It has been demonstrated that various dendritic structures, inherent to both organic and inorganic matter, can be particularly beneficial in that respect[6,7] .

One of the most intriguing examples of a spontaneous pattern formation in nature, resulting in a variety of beautiful shapes, is the growth of a dendrite. Although formally not classified as self-assembled entity[8], the formation of a dendrite is intrinsically a non-equilibrium phenomenon[9]. Of interest to us is a particular type of dendrites whose growth is controlled by diffusion processes, leading to structures that exhibit self-similarity on an extended length scale; i.e. the fractal dendrites[10]. According to the diffusion-limited aggregation (DLA) model

due to Witten and Sander[11], an irreversible attachment to a seed aggregate of the particles performing surface random walk leads to an open-structure branched two-dimensional dendrites with fractal dimensionality of $D \approx 1.70$. The DLA-like patterns have been found in nature[12] but have also been realized experimentally in some physical systems involving complex phenomena such as electrochemical deposition[13], dielectric breakdown[14] and solidification from supersaturated solutions[15]. Such patterns have been recently found in epitaxial thin films of pentacene[16] where dendrite morphology can be controlled by the deposition rate, surface coverage, and the type of substrate[17,18]. Here we report on DLA-like patterns that form during spontaneous crystallization of aged amorphous *N*,*N* 8-Bis(3-tolyl)-*N*,*N*'-bis(phenyl)benzidine (TPD) (Hole transport layer) films when deposited on a surface-modified Indium-Tin Oxide (ITO) and show that the size of such dendrites depends on the film thickness.

2.2 Results and Discussion

One of the most used Hole Transport Layer (HTL) material in OLED is *N*,*N* 8-Bis(3-tolyl)-*N*,*N*'-bis(phenyl)benzidine (TPD). In this PhD thesis we studied the growth, on different surfaces, of thin films of TPD deposited through combinatorial physical vapor deposition method (CPVD). This method takes advantage of the angle-dependent evaporation rate from a point source to produce thin film libraries. The evaporation of TPD was conducted in a high-vacuum chamber (2x10−7 Torr) using temperature-stabilized spherical tantalum boats with a 2 mm pinhole. The TPD films were evaporated on a rectangular (2 cm x 7 cm) substrate whose end was placed at a short distance (3,5 cm) above the evaporator. As a result, the thickness of deposited films varied considerably along the substrate length. It has been previously demonstrated that the evaporation rate from a Knudsen source has a cosine-like angular dependence[19] therefore, spatially resolved optical density of the deposited films has the following functionality:

$$A = A_0 \cos^n [\arctan(\mathbf{r}/d)] \qquad \text{Eq. 1}$$

Where A_0 is the absorbance of deposited film at $\mathbf{r}=0$ (which is the point on the substrate directly above the evaporator), $\mathbf{r}$ is the substrate spatial coordinate and d is the distance between the evaporator and the substrate. The latter, in turn, determines the value of n, which can be obtained by the least squares fit of the absorbance values as a function of $\mathbf{r}$. The nominal thickness of the film was calculated from the absorbance measurements using TPD absorption coefficient α =1.6x104 cm^{-1} at 352 nm.[20] (Figure 2.1) Previous studies indicated that TPD molecules tend to form structured films when deposited on hydrophilic substrates such as fused silica. In particular a digital photograph of a TPD thin film deposited on silica showed the presence of two visually distinct sections separated by a sharp front. The section of the film above the evaporator was transparent while the other one was opaque. Consistent with this, an extended long wavelength tail was found in the absorption spectra of the opaque section of the film, which is characteristic of a light scattering process (see the inset of Figure 2.1). The light scattering was caused by microscopic TPD aggregates whose AFM images obtained at different substrate coordinates are shown in Figure 2.2.

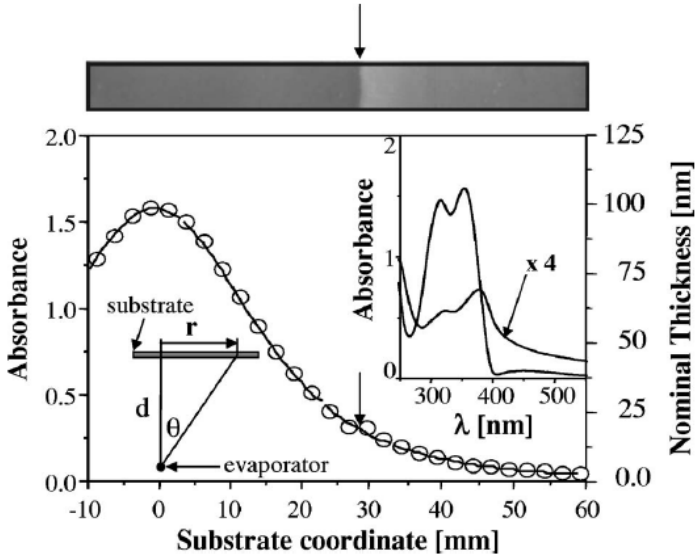

Figure 2.1: Digital photograph of a TPD thin film (top) deposited for 3 min from a point source at 461 K yielding a 100-nm-thick film at **r**=0. Visible by naked eye was a border line at **r**=29 mm separating uniform from structured portion of the film. The representative absorption spectra of the two film segments are shown in the inset. Below, the spatially resolved absorbance measurements are plotted as a function of the substrate coordinate. The solid line is the least squares fit to Eq. 1(R=0.9995) from which n=5.0±0.2 was extracted.

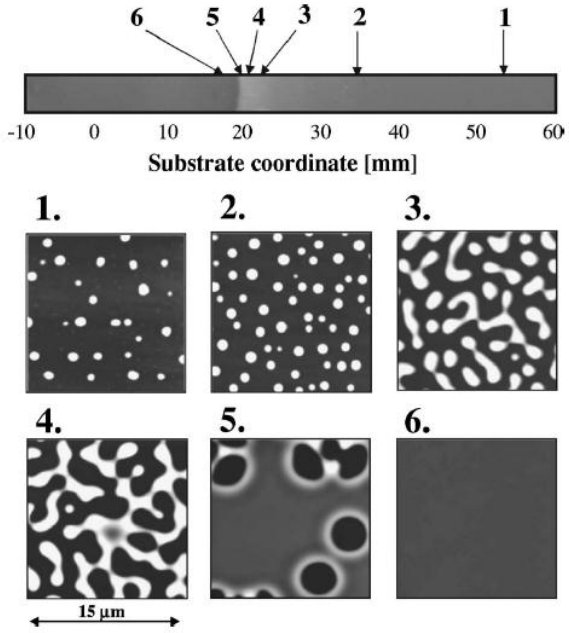

Figure 2.2: Digital photograph of a TPD thin film (top), deposited for 45 min from a point source at 427 K, yielding a 100-nm-thick film at **r**=0 and the border line at **r**=19 mm. Shown below are AFM images of various morphology phases that have been identified, linked by a number to the spatial position on the substrate. The following distinct morphology phases were found: spherical droplets (1 and 2), isolated striplets (3), percolated striplets (4), inverse droplets/holes (5) uniform film (6).

Starting at the substrate end with smallest deposition rate, the TPD morphology gradually evolves from sparsely populated spherical droplets (1) through a domain phase composed of packed droplets (2), which evolves into separated striplets (3). Further increase of the

deposition rate (i.e., the coverage) leads to a percolated striplet phase (4), which is followed by a tiny section of a flat film with randomly distributed pores (5). Further increase in the deposition rate gives rise to uniform flat film at thicknesses $d \geq 29$ nm. This results indicate that an already low glass-transition temperature of TPD bulk ($Tg = 62\ ^0C$) is further lowered in thin TPD films. The reason for it is a weak van der Waals interaction between the hydrophilic substrate and hydrophobic TPD molecules, which destabilizes thin TPD films in respect to dewetting.

During this thesis we performed an investigation of influence of surface polarity on TPD thin films. In particular as substrates we chose ITO (Indium-tin oxide) the standard anode in OLED devices, that bears OH functionalities on its surface and a functionalized ITO (hereafter called FITO) with a surface covered by a monolayer of chemically bonded TPD molecules.

The TPD films deposited on ITO substrate at room temperature were found to be flat and uniform for film thicknesses $d \geq 27$ nm. Below this critical value, the structured TPD films begin to form by dewetting within several hours after the deposition. As shown in Figure 2.3, various morphology features, very similar to those observed on fused silica, were identified ranging from isolated TPD droplets (formed at the thinner end of the TPD film) to inverted droplets occurring in the vicinity of the border line separating uniform from the structured film. The structured TPD films remained amorphous for several days after the deposition but eventually crystallized without a significant change in their morphology, confirming results of an earlier morphology study of TPD thin films[20].

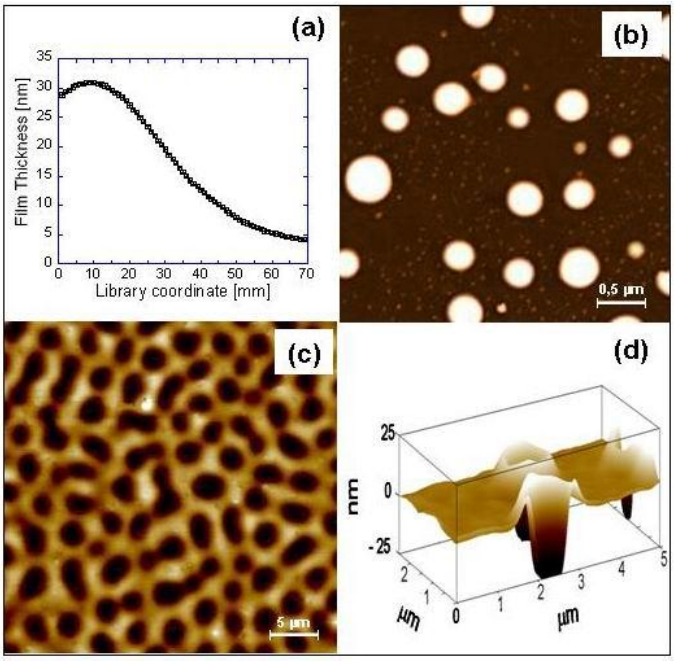

Figure 2.3 (a) Thickness profile of TPD films used in this study. AFM images of: (b) TPD droplets, (c) the percolated TPD network, and (d) circular holes (i.e. the inverted droplets) in the TPD film, found near the border line separating uniform from the structured film.

The FITO surface was prepared by reacting ITO surface OH groups with a TPD derivative bearing two $SiCl_3$ units (TPD-Si_2) synthetized as reported in the literature[21] according to the following scheme:

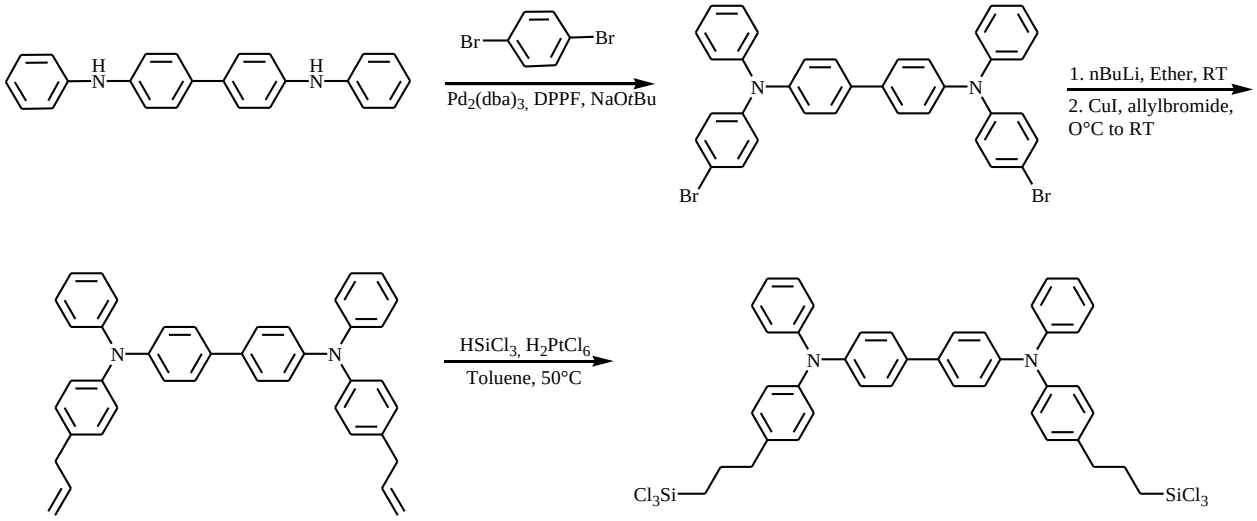

Scheme 2.1: Synthesis of TPD-Si_2

Utilizing a self-limiting, solution based chemisorption process, TPD-Si_2 is self-assembled onto hydrophilic ITO substrate surfaces with nanoprecise control in thickness. As illustrated

in Scheme 2.2, clean ITO-coated glass possess hydroxyl functionalities, which are reactive toward chlorosilanes, thereby affording covalent binding of the silanes to the surface. [22,23,24,25]

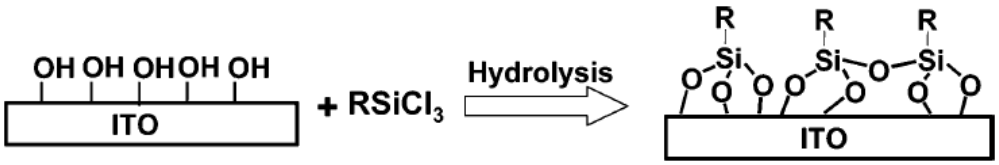

Scheme 2.2: Scheme for ITO Surface Modified by Covalently Bound HTL Materials

Further exposure to air and moisture (by rinsing in wet acetone) hydrolyzes any unreacted trichlorosilyl groups. Thermal curing facilitates the formation of cross-linked siloxane networks, resulting in a thin layer consisting of hole transporting motifs covalently anchored to the ITO surface.

Unlike the TPD morphologies on ITO, the amorphous TPD films deposited on FITO were found to be unstructured in the entire range of film thicknesses (5 nm < d < 30 nm).

Figure 2.4

A parallel experiment of PVD deposition on FITO and ITO substrates confirmed the formation of flat films on FITO, while structured films are obtained on ITO in same experimental conditions. (Figure 2.4) As anticipated the stronger van der Waals interaction between deposited TPD molecules and a covalently bound SAM stabilizes TPD films in respect to dewetting, which is an important result from the prospective of a device scientist. However, the presence of a hydrophobic SAM on ITO does not prevent spontaneous crystallization of TPD films. After several days in air TPD films on FITO develop a large number of randomly distributed seed crystallites over the entire range of film thicknesses, which evolve into dendrites of the kind shown in Figure 2.5.

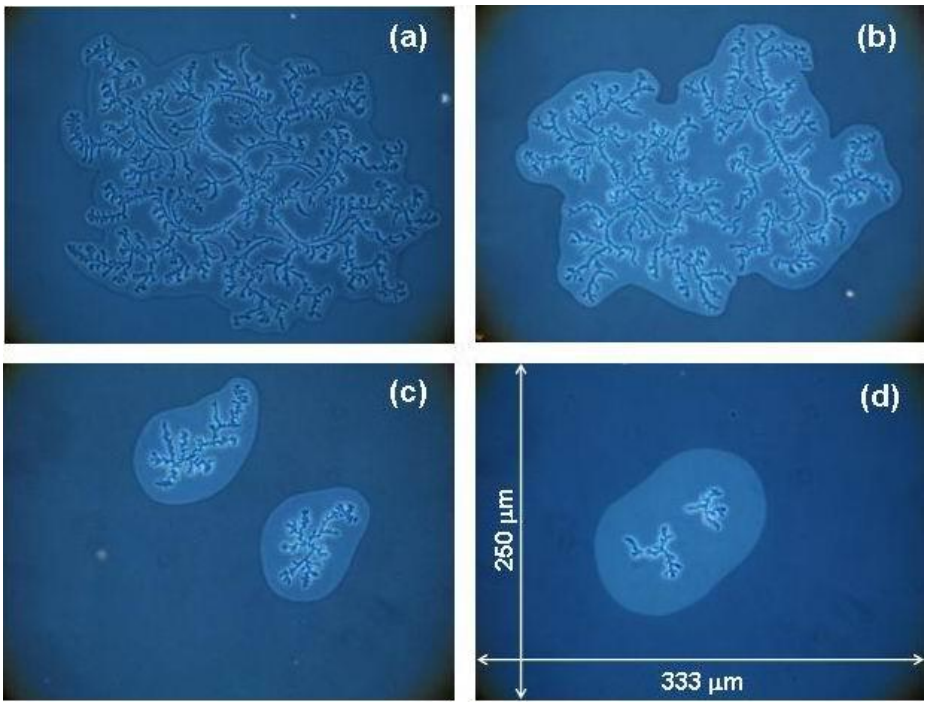

Figure 2.5. Representative images of TPD dendrites growing on FITO surface by amorphous-to-crystalline phase transformation mediated by the DLA mechanism. The images were taken in different thickness areas, 96 hours after the film deposition: 31 nm (a), 25 nm (b), 20 nm (c) and 8 nm (d).

The TPD dendrites exhibit up to four leading branches emerging from the central seed aggregate, decorated with a number of short side-branches. Clearly visible under an optical microscope was a sharp front of amorphous TPD film surrounding the dendrites at a distance of several micrometers. Statistical survey of a large number of dendrite images at different film thicknesses revealed that dendrite lateral size increases with the film thickness while the separation between dendrite leading branches and the edge of the amorphous film has the opposite trend (see Figure 2.3a). An AFM top-view image in the inset of Figure 2.6a reveals well-developed facetted edges of a tip of the dendrite branch suggesting its crystalline nature. A high resolution AFM cross section scan in Figure 2.6b shows the edge of a 17 nm tick amorphous film making a contact angle with the FITO surface on the order of $\theta_c \approx 4^0$, separated by some 7 µm from a tip of the dendrite branch.

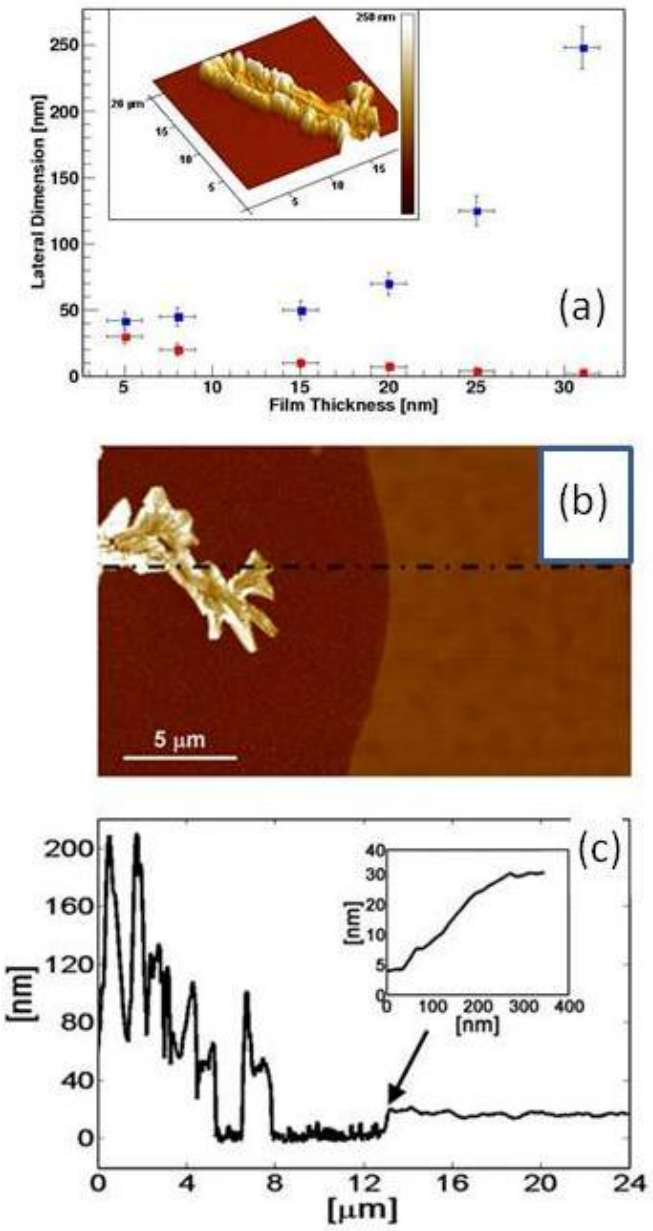

Figure 2.6. (a) The average dendrite size (blue squares) and the separation between the tips of dendrite branches (red squares) from the amorphous film edge as a function of the TPD film thickness. A spread in the dendrite average size arises from the fact that not all the dendrites were conceived at the same time. An AFM top-view image of a dendrite tip is shown in the inset. (b) A high resolution AFM image showing morphology of a dendrite branch separated ~7 μm from the edge of a 17 nm tick amorphous TPD film. (c) Corresponding cross-section of the dendrite branch with the inset showing a profile of the amorphous TPD film making surface contact angle of $\theta_c \approx 4^0$ with the FITO surface.

In Figure 2.6c, the AFM cross section scan reveals a ragged surface of the dendrite branch whose average height exceeds that of the surrounding amorphous film. Continuing inspection of a TPD library with growing dendrites reveals that, after several days, the entire amorphous

film transforms into TPD dendrites where the trend in dendrite size with the initial film thickness has been preserved.

From the above observations the following qualitative analysis emerges. Following random formation of TPD seed crystallites, the surrounding amorphous film is quickly depleted because dendrite average height exceeds that of the surrounding film. The separation between the amorphous TPD film and the growing dendrite necessitates surface diffusion of TPD molecules over the FITO substrate. The resulting directional mass transport (from the amorphous film to dendrite branches) implies a presence of the surface concentration gradient. Although we do not have direct evidence of the crystalline nature of TPD dendrites, the higher thermodynamic stability of dendrites in respect to the amorphous film and the presence of faceted edges of the dendrite branches should be sufficient arguments. Hence, we have a rare example of amorphous-to-crystalline phase transformation in an organic thin films mediated by the surface diffusion. For the film thicknesses of up to ~25 nm, the rate of dendrite growth in the vertical direction exceeds the surface diffusion rate and thus leads to steadily increasing separation between the crystal and the amorphous film. For the film thicknesses larger than 25 nm, the lateral growth of dendrite branches continues indefinitely and the dendrite size becomes limited by simultaneous growth of neighboring dendrites. Therefore for the certain range of the film thicknesses the growth rate of TPD dendrites increases with the film thickness, which is the cause of the observed trends in the dendrite size and their mutual separation.

The dynamics of the dendrite growth was captured by a camera attached to an optical microscope. Some 200 images of a dendrite growing in a 30 nm thick TPD film were taken in equal time intervals over 90 hours and are compressed in a 30 seconds long presentation revealing details of the dendrite growth kinetics (By comparison the formation of disordered and structured TPD films on bare ITO surface can be viewed at the following link: http://users.unimi.it/cimaina/stuff/movie2.avi). The growth of TPD dendrites on the FITO surface is extremely slow. For the film thickness of 30 nm the velocity of the leading branches is on the order of $v = 1x10^{-4}$ μm/s, therefore it takes about two days for a dendrite of 70 m in diameter to double its size. The tips of the leading branches are never in direct contact with surrounding amorphous film; hence the dendrite growth can only proceed by the surface diffusion of TPD species. The leading branches gear their tips towards the highest concentration gradient, which changes frequently due to local fluctuation in the diffusion field caused by surface imperfections and the competition with neighboring branches. Particularly interesting is the "collision" of two dendrites growing in the same area, which can be seen

towards the end of the movie presentation. All the colliding branches remained separated by a couple of microns as the amorphous TPD film was consumed before the contact between the two dendrites could have been made.

A remarkable feature of the TPD dendrite growth is the presence of retreating amorphous film whose front edge is clearly visible under the optical microscope. This makes it possible to account quantitatively for the mass transport of TPD molecules and make an estimate of the surface diffusion coefficient[26], D_s, by using Fick's first law, $J = -D_s \partial\phi/\partial x$. Here J is the diffusion flux and $-\partial\phi/\partial x$ is the surface concentration gradient. The one-dimensional approximation is plausible since the mass transport occurs mainly between the tips of dendrite branches and nearby edge of the amorphous film. While diffusion flux can be accurately computed from the area of amorphous film consumed in time, the concentration gradient needs a rough estimate. The contact angle of $\theta_c \approx 4^0$ implies that a 30 nm thick amorphous film evolves in a TPD monolayer some 430 nm from its edge. We assume here that the surface density of TPD molecules in the vicinity of dendrite tips is at least an order of magnitude smaller than that of the TPD monolayer and thus can be neglected. The average distance between the amorphous film edge and the leading dendrite tips was estimated to be on the order of 5 μm. This leads to $\partial\phi/\partial x \leq |-4.7 \times 10^8|$ molm^{-4} and the surface diffusion constant $D_s \geq 1 \times 10^{-14}$ m^{2}s^{-1} for TPD on FITO at 294 K (see Table 1)

Table 1. Time evolution of TPD surface area consumed by a growing dendrite in Fig 2.5b and the corresponding surface diffusion constant D_s.

ΔS_A [μm^2][a]	P [μm][b]	$\Delta J \times 10^6$ [*mol*m^{-2}s^{-1}][c]	$D_s \times 10^{14}$[m^{2}s^{-1}]
323	292	3.2	0.7
447	306	4.3	0.9
506	332	4.5	1.0
612	342	5.2	1.1
671	378	5.2	1.1
1022	399	7.5	1.6
1058	439	7.0	1.5

[a] Surface area of the TPD film consumed by dendrite in seven consecutive Δt = 7.5 h time intervals (see Fig.2.5b).

[b] The perimeter of TPD hole-contours.

[c] The flux of TPD molecules defined as a number of TPD *mols*, $(\rho/M)\Delta S_A d$, crossing the unit surface area, Pd_m, in a unit time, Δt: $\Delta J = (\rho/M)\Delta S_A d/(Pd_m \Delta t)$. ρ=1.22 g/cm^3 and M = 520 g/mol are TPD density and the molar mass, d=30 nm is the TPD film thickness and d_m = 0.89 nm is the thickness of TPD monolayer. The latter was estimated from $d_m = [(\rho/M)A]^{-1/3}$ where A is Avogadro number.

The small fluctuations of the diffusion constant during the dendrite growth are probably caused by surface imperfections giving rise to temporal changes of the concentration gradient. The fact that the average height of TPD dendrites is negligible in comparison to their lateral dimension and that their growth is limited by surface diffusion satisfies formally the basic postulates of the two-dimensional DLA model[8]. Also, like in a DLA computer simulations, there is a "lunching circle" and the "killing circle" surrounding a TPD dendrite (in our case the front edge of the amorphous TPD film plays the role of the both circles), which increases in perimeter as the growth of dendrite branches progresses (see Figure 2.7).

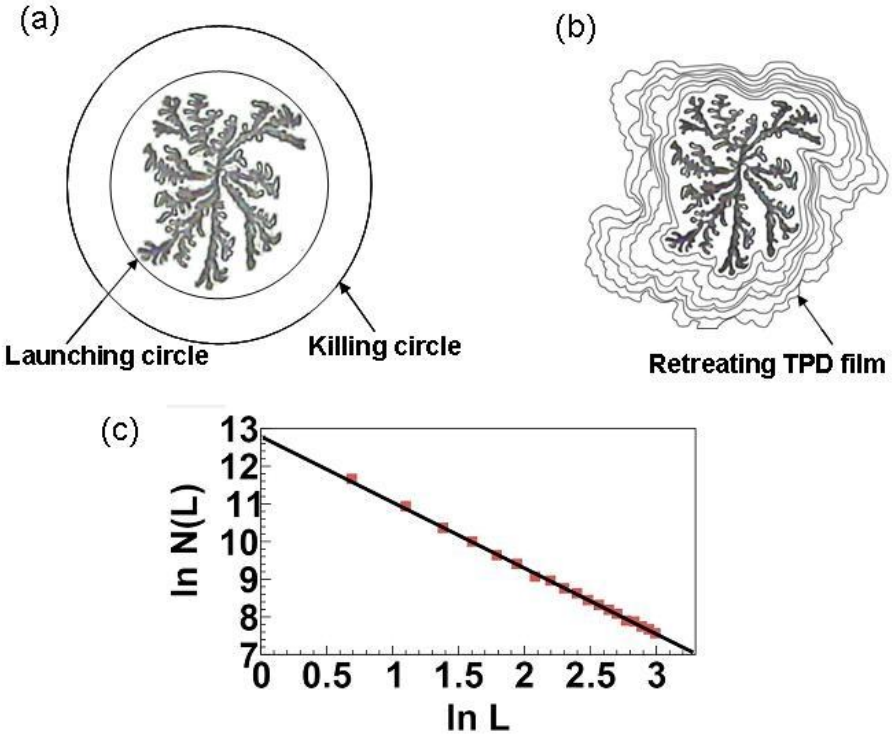

Figure 2.7. (a) Schematic of the DLA model computer simulation involving random walkers emerging from one at the time form the lunching circle. They either stick to the growing dendrite or are eliminated if they cross the killing circle. (b) Images of amorphous TPD film on FITO obtained in 7.5 hours intervals. The TPD molecules diffuse from the edge of the TPD film towards the dendrite. Only the initial size of the growing dendrite was shown for clarity. (c) The box-covering diagram.

Yet, there are some important differences too. In the DLA model the random walkers are released one at the time, they move over an ideally smooth surface and their attachment to the growing dendrite is irreversible. In the case of TPD dendrites there are multiple walkers present at the time and their mass transport is guided by the concentration field gradient. Finally, the FITO surface roughness is considerably larger than the size of TPD molecule and their sticking coefficient is probably smaller than unity.

In spite the fact that some important premises of the DLA model are not applicable to the growth of TPD dendrites, we find those to have both fractal dimension and density-density correlation power law consistent with the DLA model. The fractal properties of the TPD dendrites appear in the region $\lambda < L < \Lambda$, where λ is the resolution of data (around one pixel) and Λ is the length scale at which the finite size effects appear in the statistical analysis. In order to measure the fractal dimension we applied the box-covering algorithm by starting from the scale $\lambda \approx 1$ pixel up to 20λ. Shown in Figure 2.7c is a log-plot of the number of boxes versus the size of the box. The measure of the fractal dimension is given by the slope of the linear fit: $D_{exp} = 1.73 \pm 0.02$, in a good agreement with the expectation of the DLA model (1.70 ± 0.02)[11]. Even though the growth of TPD dendrites shares the same underlying physics the DLA model was built on, a nearly quantitative agreement with the DLA predictions in respect to the fractal dimensionality is puzzling.

2.3 Conclusions

Presented is an influence of the surface functionalization on time evolution of TPD thin film morphology on ITO. It was found that air-exposed amorphous TPD films on ITO are subject to dewetting phenomena for the film thickness d< 27 nm, which occur within an hour after the deposition. Such changes in morphology can be prevented by anchoring a covalently bound SAM of a TPD moiety onto ITO surface. Nevertheless, in a matter of days the thin TPD films undergo a spontaneous amorphous-to-crystalline phase transformation regardless of the type of underlying substrate. In the case of ITO such transition does not significantly change the morphology of structured TPD films. In the case of functionalized ITO, however, the amorphous TPD film transforms into previously unobserved quasi 2-dimensional TPD dendrites whose lateral size depends of the film thickness. The reason for dendrite formation is an extremely small diffusion constant for TPD species on the functionalized ITO surface, estimated to be on the order of $D_s \geq 1 \times 10^{-14}$ m^2s^{-1}. The slow surface diffusion of TPD molecules determinates the rate of crystal growth and thus gives rise to fractal dendrites in compliance with the well-known diffusion-limited aggregation (DLA) model of Witten and Sander[11]. The observed fractal dimensionality of TPD dendrites was found to be D_{exp} = 1.73±0.02 in a good agreement with the predictions of DLA model. There is no reason that formation of dendritic structures during spontaneous crystallization of amorphous thin organic films is a unique property of TPD species. Such phenomena should occur in thin films of other molecular solids in the vicinity of their-glass transition temperatures, provided a proper substrate functionalization that leads to slow surface diffusion.

2.4 Experimental section

2.4.1 General methods

All reagents and solvents were purchased from Sigma Aldrich and were used as received or purified using standard procedures. NMR spectra were recorded at room temperature on a Bruker Avance DRX 400 MHz. The chemical shifts δ are expressed in ppm relative to the used deuteriated solvents and tetramethylsilane as internal standard. The multiplicity of the ^{1}H spectra is expressed as follows:

s = singlet; d = doublet; dd = doublet of doublet; t = triplet; m = multiplet.

When possible mass spectra (VG Autospec M256) and elemental analysis (Perkin-Elmer CHN 2400) have also been performed.

2.4.2 Synthesis of 4,4'-Bis[(*p*-bromophenyl)phenylamino)]biphenyl (1).

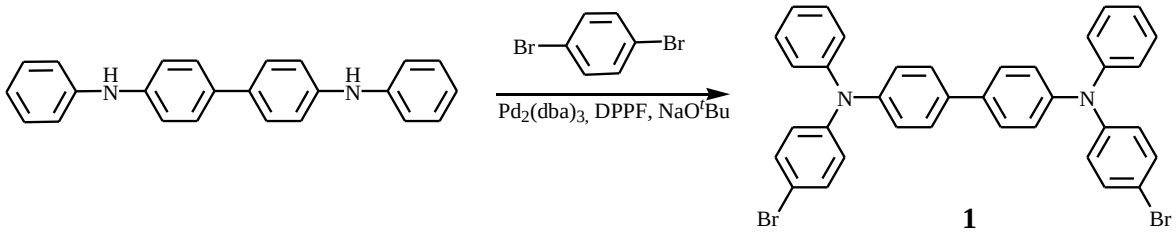

1

To a toluene solution (50 mL) of tris(dibenzyldeneacetone)dipalladium (0.55 g, 0.60 mmol) and bis(diphenylphosphino)ferrocene (0.50 g, 0.90 mmol) was added 1,4-dibromobenzene (18.9 g, 0.0800 mol) at 25 °C. Following stirring under an N_2 atmosphere for 10 min, sodium *tert*-butoxide (4.8 g, 0.050 mol) and *N*,*N*'-diphenylbenzidine (6.8 g, 0.020 mol) were added. The reaction mixture was then stirred at 90 °C for 12 h, followed by cooling to 25 °C. The reaction mixture was then poured into water, and the organic and aqueous layers were separated. The aqueous layer was extracted with toluene (3x100 mL), and the resulting extracts were combined with the original organic layer. The solvent was removed in vacuo giving a crude product which was purified by chromatography on a silica gel column (6:1 hexane:methylene chloride eluent) to yield pure **1** as a colorless solid (6.9 g) in 50% yield.

^{1}H NMR (400 MHz, $CDCl_3$): 6.99 (d, J=8.8 Hz, 4H), 7.02-7.16 (m, 10H), 7.28 (t, J=7.6 Hz, 4H), 7.34 (d, J=8.8 Hz, 4H), 7.45 (d, J=8.4 Hz, 4H).

^{1}H NMR (400 MHz, $CDCl_3$):

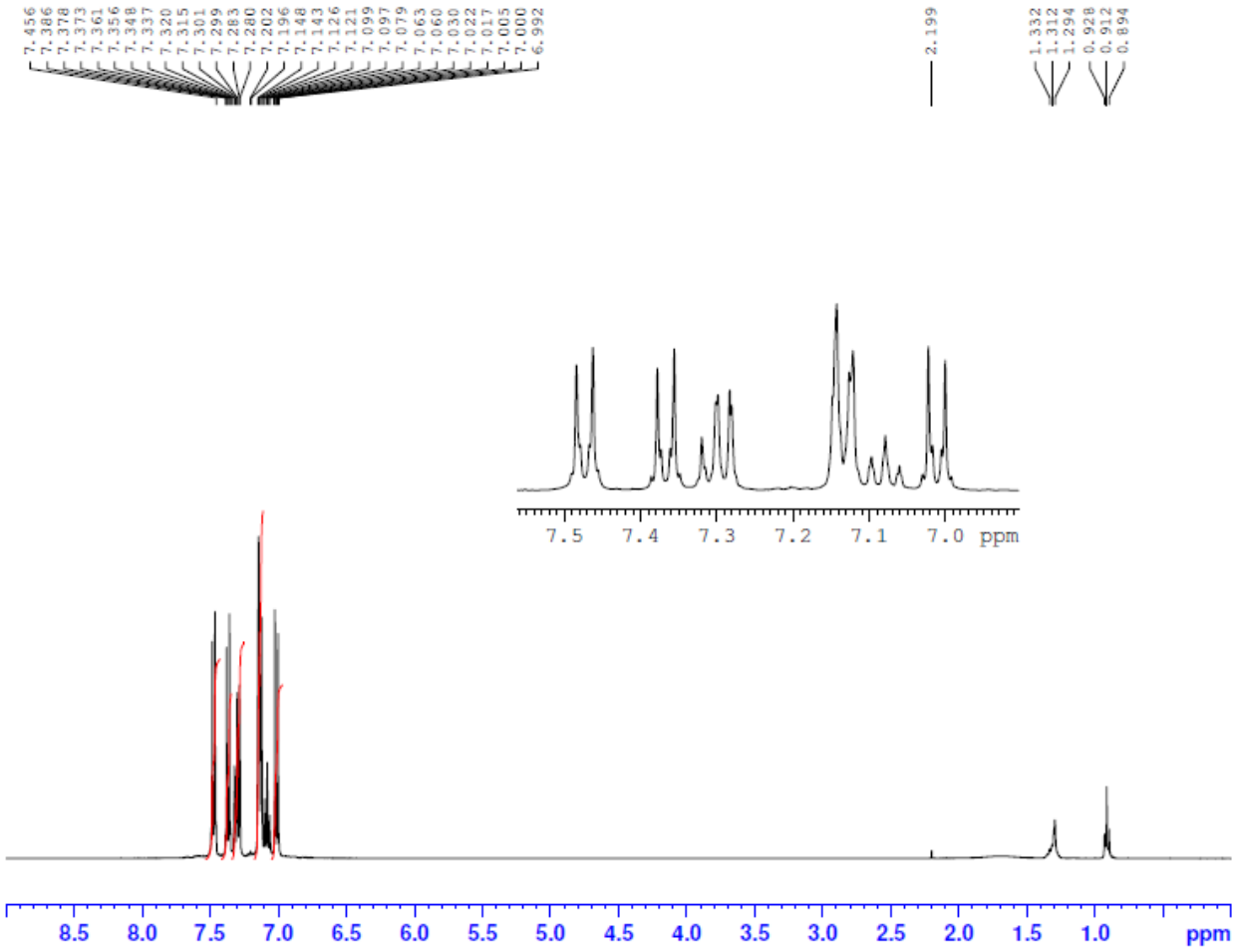

2.4.3 Synthesis of 4,4'-Bis[(*p*-allylphenyl)phenylamino]biphenyl (2).

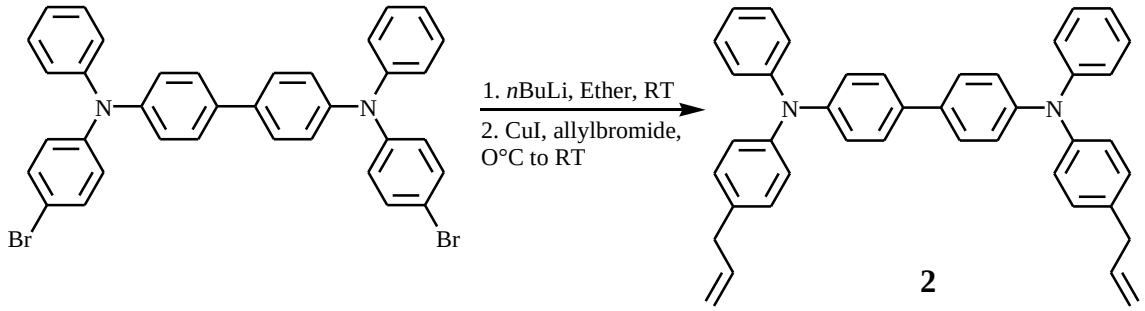

Using standard Schlenk techniques, 1.6 mL (3.5 mmol) of *n*-butyllithium (2.5 M in hexanes) was added dropwise under inert atmosphere to an ether solution (10 mL) of **1** (1.02 g, 1.58 mmol) while maintaining the temperature at 25 °C. The mixture was stirred for 2 h, then CuI (0.76 g, 4.0 mmol) was added. Upon cooling the reaction mixture to 0 °C, allyl bromide (0.60 g, 5.0 mmol) was added in one portion, and the mixture was stirred for 14 h (during which was allowed to warm at room temperature), followed by quenching with saturated aqueous NH_4Cl solution (100 mL) and extraction with ether (3x100 mL). The combined ether extracts were washed with water (2x100 mL) and brine (2x100 mL), and dried over anhydrous Na_2SO_4. Filtration and removal of solvent in vacuum afforded a yellow oil, which was further purified by chromatography on a silica gel column (4:1 hexane : methylene chloride) to yield 0.63 g of pure **2** as a colorless solid. Yield, 70%.

^{1}H NMR (400 MHz, $CDCl_3$): 3.40 (d, J=10 Hz, 4H), 5.10-5.20 (m, 4H), 6.03 (m, 2H), 7.01-7.10 (m, 2H), 7.10- 7.20 (m, 16H), 7.28 (t, J=7.6 Hz, 4H), 7.46 (d, J=8.8 Hz, 4H).

Elemental Analysis for $C_{42}H_{36}N_2$: Calculated %C, 88.68; %H, 6.39; %N, 5.23. Found: %C, 87.50; %H, 6.35; %N, 4.93.

^{1}H NMR (400 MHz, $CDCl_3$):

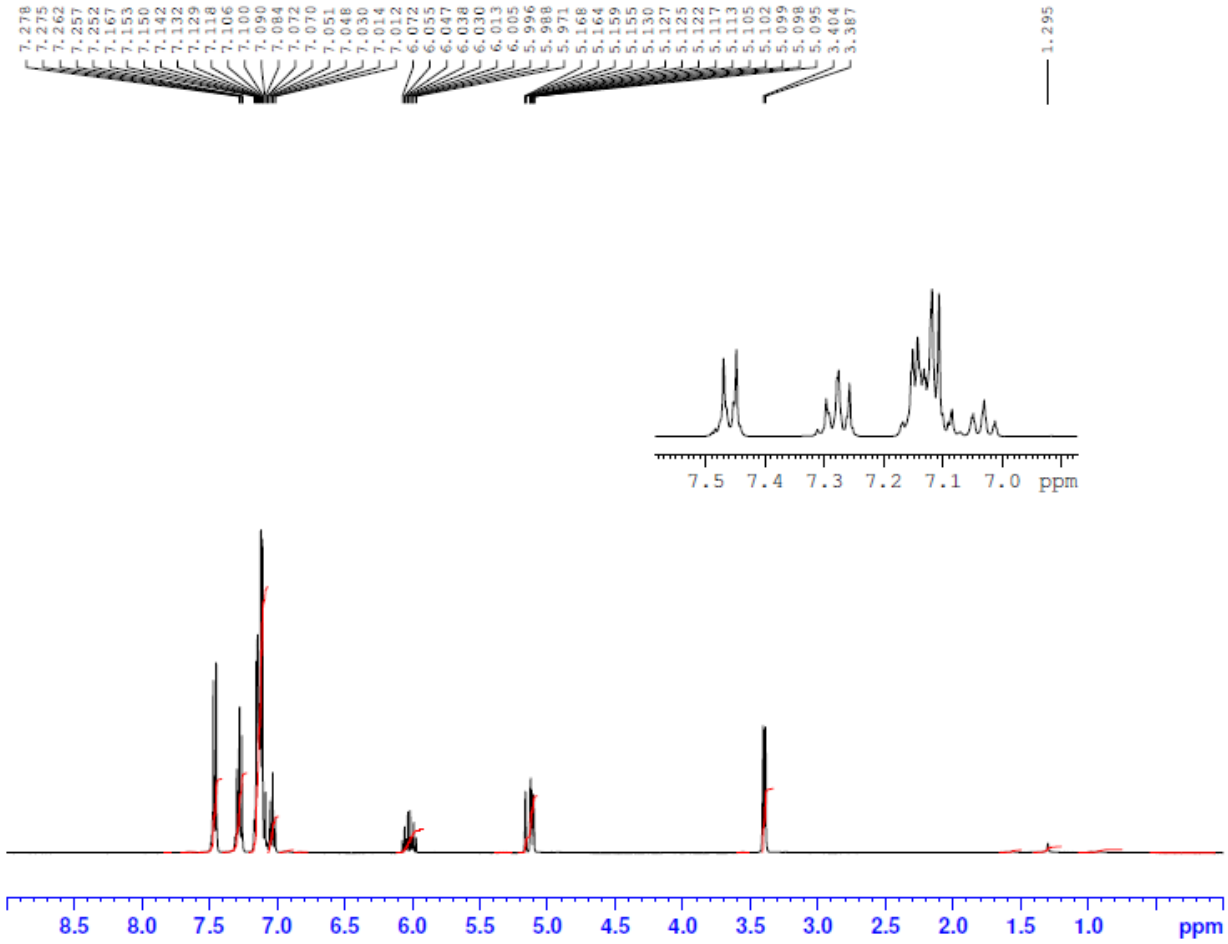

2.4.4 Synthesis of 4,4'-Bis[(*p*-trichlorosilylpropylphenyl)phenylamino]-biphenyl (TPD-Si_2, 3).

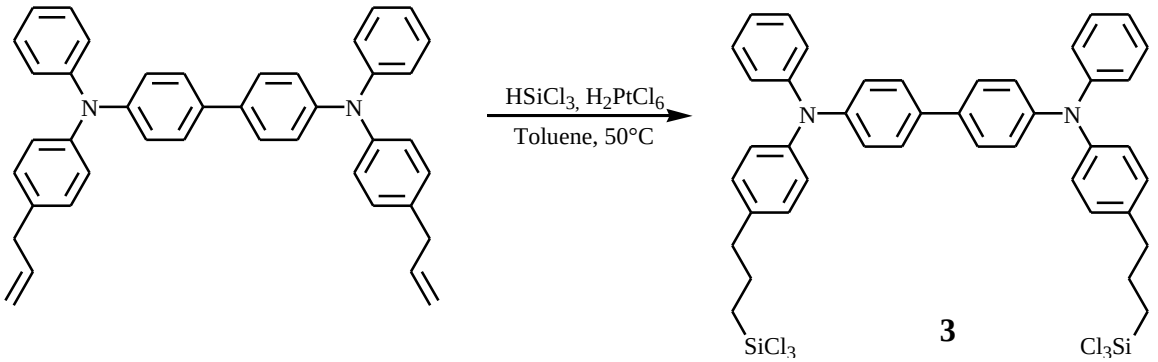

3

Under inert atmosphere at 25 °C, a grain of H_2PtCl_6, followed by $HSiCl_3$ (0.73 g, 5.5 mmol), was added to a CH_2Cl_2 solution (30 mL) of **2** (0.32 g, 0.55 mol), and the reaction mixture was stirred at 30 °C for 4 h. Removal of the solvent in vacuum yielded a dark-yellow oil, which was triturated with a mixture of 50 mL of pentane and 10 mL of toluene to yield a solid that was removed by filtration. The filtrate was concentrated in vacuum to yield **3** as a viscous, pale-yellow oil. Yield, 98%.

Elemental Analysis $C_{42}H_{38}Cl_6N_2Si_2$: Calculated %C, 60.08; %H, 4.56; %N 3.34. Found: %C, 60.52; %H, 4.87; %N, 3.29.

2.4.5 Synthesis of the self-assembled monolayer.

The ITO slides (Delta Technologies) were cleaned by washing with Hellmanex solution (5% vol), milliQ water (3 times), acetone and isopropanol followed by oxygen plasma etching. The surface functionalization was performed under nitrogen atmosphere in a schlenk line by immersion for 1 hour at 80°C in a dry toluene 0.02 M solution of 4,4'-bis[(*p*-trichlorosilylpropylphenyl)phenylamino]biphenyl (TPD-Si_2). The functionalized ITO slides were rinsed twice with toluene and wet acetone then dried at 120°C in an oven for 1h prior the deposition of TPD films. The full coverage of ITO surface by TPD-Si_2 self-assembled monolayer (SAM) was confirmed by cyclic voltammetry and XPS studies indicating completion of the silane hydrolysis and condensation process. The presence of a covalently bound SAM on functionalized ITO (hereafter abbreviated as FITO) was also verified by atomic force microscopy (AFM) and contact angle measurements. While the ITO surface roughness (2.8 nm) did not change significantly after the functionalization, the contact angle of water droplets increased from 20° on ITO to 90° on FITO thus indicating successful transformation of a hydrophilic to a hydrophobic surface.

2.4.6 Preparation of thin TPD thin films.

Thin films of TPD were deposited by a combinatorial vapor deposition method (CPVD). The method takes advantage of the angular dependence of evaporation rate form a Knüdsen source to produce thin organic films with a cosine-like thickness gradient along a rectangular (75x25 mm) ITO substrate (see Fig. 1a). This allows for an easy survey of the morphology at the different thicknesses by means of AFM or optical microscopy. The TPD films of about 30 nm at the peak of the thickness profile required 10 minutes deposition time at 190 ^{0}C source temperature. Prior the deposition traces of surface adsorbed moisture were removed by heating the substrate, which was held at room temperature during the deposition.

2.4.6 Instrumental

AFM. The investigation of morphology of the samples was carried out in air using a Bioscope II AFM (Veeco, USA). The AFM was operated in a tapping mode at scan rates of 20-2000 $\mu m^2 s^{-1}$. Standard single-crystal silicon cantilevers with resonance frequencies between 0.2 and 1.2 Hz and nominal radius of the tip curvature of 5-10 nm were used. AFM images are typically flattened line by line subtracting a polynomial function in order to get rid of the tilt of the sample substrate and of the scanner bow.

Optical Microscopy. The optical images in Fig. 1 were acquired with an Axiovert 40 CFL (Zeiss, Germany), inverted microscope using 40X objective and a digital camera (Canon Powershot G6 - 7.1 Megapixel). Except for Fig 1a, the contrast between the amorphous film and the FITO substrate was enhanced for clarity.

Media. The dendrite growth was recorded with a color CCD camera Sanyo VCC-3700P (500 x 582 pixels) mounted on a IX71 inverted microscope provided by Olympus, using a 20X magnification in phase contrast mode. Some 213 images were taken in 25 minute intervals and were compressed into a 30 seconds long presentation.

2.5 References

[1] Forrest, J. A., Dalnoki-Veress, K., Dutcher, J. R. *Phys. Rev. E.* **1997**, *56*, 5705.

[2] Higgins, A. M., Jones, R. A. L. *Nature* **2000**, *404*, 476.

[3] Aziz, H., Popovic, Z., Xie, S., Hor, A-M., Hu, N-X., Tripp, C. *Appl. Phys. Lett.* **1998**, *72*, 756.

[4] Campoy-Quiles, M., Ferenczi, T., Agostinelli, T., Etchegoin, P. G., Kim, Y. , Anthopoulos, T. D., Stavrinou, P.
N., Bradley, D. D. C., Nelson, J. *Nat. Mater.* **2008**, *7*, 158.

[5] Hoppe, H., Sariciftci, S. N. *J. Mater. Chem.* **2006**, *16*, 45.

[6] R. G. Seidensticker, *J. Cryst. Growth* **1977**, *39*, 17.

[7] Baxter, J. B., Aydil, E. S. *App. Phys. Lett.* **2005**, *86*, 053114.

[8] Whitesides, G. M., Grzybowski, B. *Science* **2002**, *295*, 2418.

[9] Langer, J. S. *Rev. Mod. Phys.* **1980**, *52*, 1.

[10] Meakin, P. *Fractals, scaling and growth far from equilibrium* (Cambridge University Press 1998).

[11] Witten, T. A., Sander, L. M. *Phys. Rev. Lett.* **1987,** *47*, 1400.

[12] Chopard, B., Herrmann, H. J., Vicsek T. *Nature* **1991**, *353*, 409.

[13] Argoul, F., Arneodo, A., Grasseau, G. *Phys. Rev. Lett.* **1988**, *61*, 2558.

[14] Niemeyer, L., Pietronero, L., Wiesmann, H. J. *Phys. Rev. Lett.* **1984**, *52*, 1033.

[15] Ohta, S., Honjo, H. *Phys. Rev. Lett.* **1988**, 60, 611.

[16] Meyer, F. J., Heringdorf, M. Z., Reuter M. C., Tromp R. M. *Nature* **2001**, *412*, 517.

[17] Ruiz, R., Nickel, B., Koch, N., Feldman, L. C., Haglund, R. F., Kahn, A., Scoles G. *Phys. Rev. B* **2003**, *67*, 125406.

[18] Pratontep, S., Brinkmann, M., Nuësch, F. , Zuppiroli, L. *Phys. Rev. B* **2004,** *69*, 165201.

[19] M. Ohring, *Materials Science of Thin Films* (Academic, New York, 2002).

[20] W. Holzer, A. Penzkofer, and H.-H. Hörhold, Synth. Met. **2002**, *113*, 281.

[21] Huang Q.,. Evmenenko G. A., Dutta P., Lee P.,. Armstrong R. N., Marks T. J, *al. J. Am. Chem. Soc.* **2005**, 127, 10227.

[22] Ulman, A. *Chem. Re*V. **1996**, *96*, 1533-1554.

[23] Jeon, N. L.; Nuzzo, R. G.; Xia, Y.; Mrksich, M.; Whitesides, G. M. *Langmuir* **1995**, *11*, 3024-3026.

[24] Ulman, A. *Thin Solid Films* **1996**, *273*, 48-53.

[25] Woodward, J. T.; Ulman, A.; Schwartz, D. K. *Langmuir* **1996**, *12*, 3626-3629.

[26] Seebauer, E. G., Allen, C. E. *Progress in Surface Science* **1995**, *49*, 265.

3 Synthesis of new fluorene derivatives as UV-Vis emitters for OLED application

3.1 Introduction

Since the first report on an organic light-emitting diode (OLED) with 1% of external electroluminescence quantum efficiency (ELQE) in 1987 by Tang and VanSlyke[1], a significant progress has been made in the arena of organic optoelectronics yielding many commercial products available today. The OLEDs can be made either from organic polymers or from small organic and/or organo-metallic molecules. Both have their advantages and disadvantages whose discussion goes beyond the scope of this work. The main advantage of OLEDs when compared to their inorganic counterparts (LEDs made of III-V semiconductors for instance) is the simplicity of their fabrication, variety of compounds and emission colors and the ability to adapt to various substrates including flexible plastic.

Major efforts these days are focused on improving blue emitting OLEDs in terms of their stability, longevity, quantum efficiency and the emission wavelength. Some materials for blue light emission have been developed[2] with a wide energy gap and high luminescent efficiency, and fluorenes are one of the most promising candidates in that respect[3]. However, photoluminescence (PL) and electroluminescence (EL) of some fluorene compounds as well as of many polyfluorenes exhibit an additional broadband red-shifted emission in. Its origin has been a subject of controversy and was ascribed to fluorene aggregates and/or excimers[4]. To prevent aggregation and inter-chain interactions polyfluorenes are often modified by the addition of bulky functional groups[5], dendrites[6], cross-linkable moieties[7] and by using a spiro-functionalized polymer backbone[8].

Particular emphasis has been given towards the use of fluorene compounds in fabrication of white light emitting OLEDs (WOLEDs)[9]. Idea there is to have a host with a large HOMO-LUMO gap whose emission falls at the edge of the visible and the UV region (~ 360 nm). Fluorene compounds meet such requirements as their HOMO-LUMO gaps can approach 4 eV[10] and their luminescence exhibits a very small Stokes shift, thanks to fluorene rigid structure. In WOLEDS the high energy excitons formed on the fluorene host transfer their energy by Förster and/or a Dexter mechanism to the blue-, green-, and red-emitting organic phosphors (i.e. dopants), giving rise to white light at the end. The ELQE of OLEDs is normally limited to 25%, because 75% of excitons are formed in the lowest triplet state from which the radiative transition to the singlet ground state is forbidden. This limitation can be

overcome by using organometallic phosphors with a heavy metal atoms (such as Ir or Pt for instance). In these compounds the spin-orbit interaction is much stronger when compared to the pure organic molecules so that the forbidden triplet-singlet transition becomes partially allowed. As a consequence, in such OLEDs and WOLEDs light is collected from both states (the singlet and the triplet) so that ELQEs of 100% have been claimed.

It has been recently shown that in the WOLEDs utilizing the host-guest energy transfer, the triplet state of the host should lay (on the absolute energy scale) above the triplet states of the dopants, otherwise a reverse energy transfer (i.e. the back triplet-triplet energy transfer from the dopant to the host) can occur[11]. Therefore, for the particular application, it is not only important to have a blue emitter with a large band gap and small Stokes shift but also the absolute energies of its states need to be known. About the only method which can determine absolute energies of the HOMO levels of a solid is the photon-electron spectroscopy, which we employed in this study to investigate our blue-emitting fluorene compound.

This chapter of my PhD thesis is devoted to the synthesis of the new molecule 1,3,5-tris(3,6,9-trimethoxy-9H-fluoren-9-yl)benzene, consisting of a benzene substituted in position 1, 3, 5 with three fluorene groups, functionalized in positions 3 and 6 by two methoxy groups with the aim to obtain a UV-Vis light-emitter (Figure 3.1).

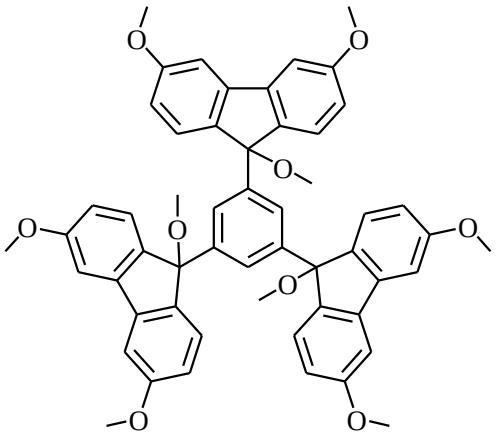

Figure 3.1: Target molecule

The main difficulty in producing this molecule is to synthesize a family of fluorenones functionalized in positions 3 and 6 (strongly de-activated by the carbonyl group in position 9). The reason for including the methoxy groups is dual:

1) to improve the fluorescence efficiency because as a rule of thumb, whenever one adds an electron donor, such as alkoxy to an aromatic unit, the fluorescence efficiency goes up;

2) to increase the conjugation length, resulting in a slight red-shift of the fluorescence, to hopefully give deeper blue color. Moreover the synthesis of a molecule with threefold symmetry should prevent it from crystallizing.

3.2 Results and discussion

As a first approach we explored the possibility to perform a Friedel-Crafts acylation between benzoylchloride and 3,3'-dimethoxybiphenyl. By using $AlCl_3$ as Lewis acid in toluene the monosubstituted derivative could be obtained with a very low yield (14%):

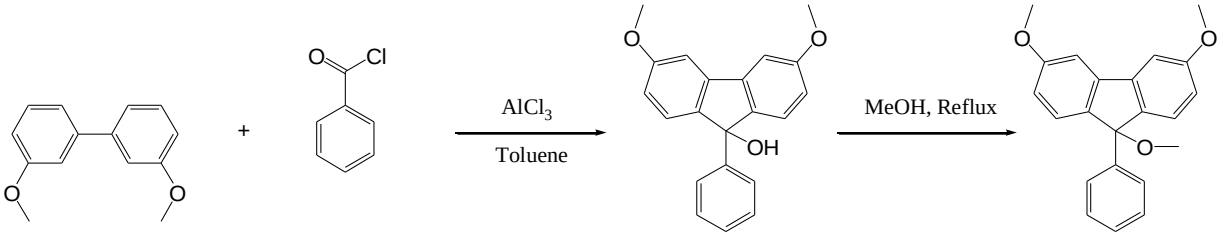

We tried to extend the previous methodic in order to obtain a tri-substituted derivative. All the attempts of Friedel-Crafts acylation, by using different solvents (Toluene, DCM, Ether) and Lewis acids ($SnCl_4$, $AlCl_3$, TiCl4, BF_3) were unsuccessful:

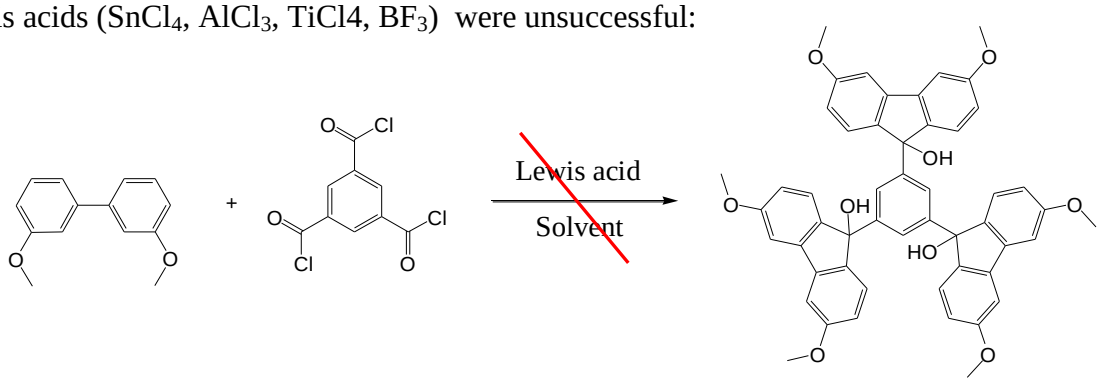

As a second approach we decided to synthesize the target molecule using the following two-step synthesis: the first step consists in the synthesis of functionalized fluorenone while the second one is the lithiation reaction between fluorenone and 1,3,5 tribromobenzene.

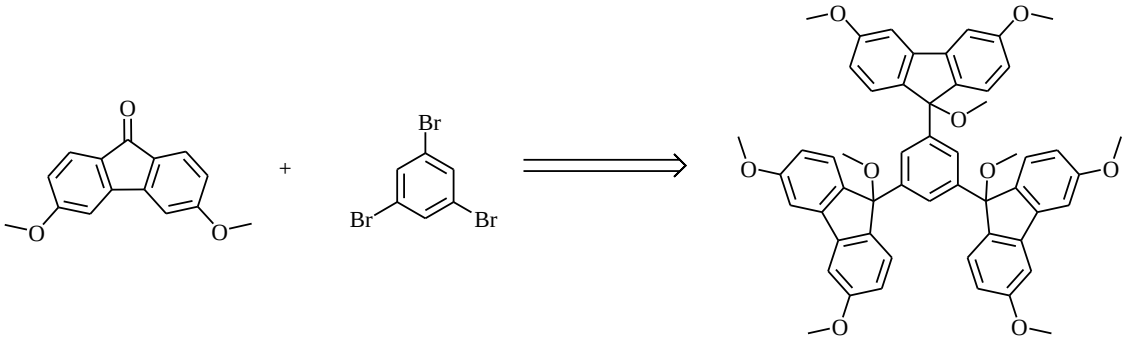

The first step of the synthesis is performed following the reaction scheme outlined in Scheme 3.1.

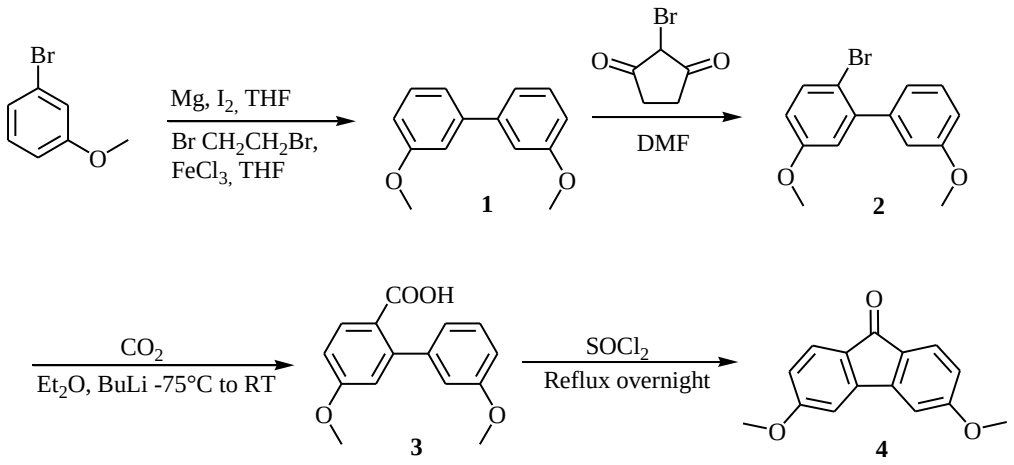

Scheme 3.1: Synthesis of fluorenone

Compound **1** prepared according to the iron-catalyzed homo-coupling reaction of 3-bromoanisole and magnesium in the presence of dibromoethane and iron trichloride to achieve the compound with the final yield to 74% yield. 3,3'-dimethoxybiphenyl was brominated with N-bromosuccinimide (NBS) in N,N-dimethylformamide (DMF) in quantitative yield, subsequent lithiation (BuLi), addition of CO_2 (as dryice) at -50°C, and acidification then provided a 96 % yield of acid **3**. This latter acid was cyclised by intramolecular Friedel-Crafts acylation in refluxing thionyl chloride to provide 3,6-dimethoxyfluorenone **4** in 76 % yield.

Concerning the second step, the synthesis of the target molecule is shown in Scheme 3.2.

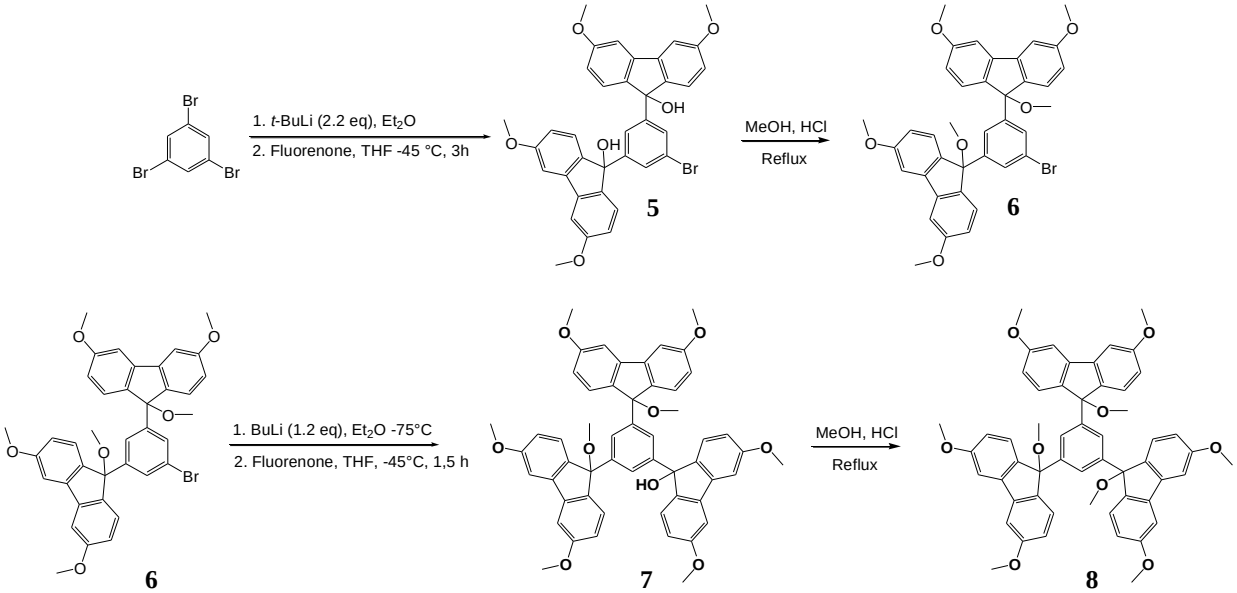

Scheme 3.2

To a solution of 1,3,5-tribromobenzene in an ethereal solvent, *tert*-butyllithium was added at -75 °C, after which the reaction mixture was quickly warmed to -50 °C, because the desired organolithium compounds are not stable at room temperature. This mixture was added by a solution of 3,6.dimethoxy-9-fluorenone in THF at 0°C (lower temperatures could not be achieved because the THF solution solidify) and stirred for 3 h at -45°C. The reaction temperature must be controlled very carefully in this latter steps because it turned out to be crucial for obtaining disubstituted compound **5** in 32% of yield. The resulting diol was then methylated with MeOH in presence of HCl resulting in **6**. 9-(3,5-bis(3,6,9-trimethoxy-9H-fluoren-9-yl)phenyl)-3,6-dimethoxy-9H-fluoren-9-ol (**7**) was synthesized by lithium-halogen exchange on **6** and subsequent addition to 9-fluorenone**.** Compound **8** was finally obtained by methylation of the OH group with MeOH and HCl at reflux to give a white solid with a 54 % of yield. It was fully characterized by ^{1}H and ^{13}C NMR, mass spectroscopy (LDI-TOF-MASS) and elemental analysis. The results are in agreement with the proposed structure. This 2-steps lithiation proved to be the best way for obtaining **8** in high yield. A direct tri-lithiation with *tert*-BuLi on 1,3,5-tribromobenzene was very difficult to control and usually afforded complex mixtures of products.

3.3 Optical properties

Absorption and emission spectra of **8** are shown in Figure. 3.2 and are similar to the poly(9,9' bis(2-ethylhexyl)-3,6-fuorene) of Cao[12]. The absorption edge at 350 nm sets the HOMO-LUMO gap of **8** at 3.6 eV while the PL spectra are peaking at ~365 nm.

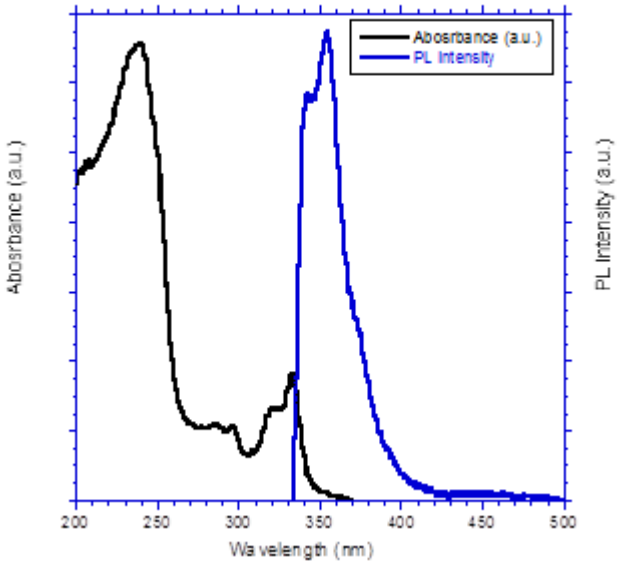

Figure 3.2: Absorption and PL spectra of **8**.

The very small Stokes shift is characteristic of fluorenes in general because of their nearly planar rigid structure that does not change much its geometry upon photon absorption. This helps keeping the emission at the border between near UV and the visible region. Our eyes are not sensitive in this spectral region so that apparent absence of the luminescence upon excitation with 250 nm radiation from a halogen lamp can be misleading. In fact, the strong emission of **8** is only obtained from spin coated thin films where **8** molecules are dispersed in a PMMA matrix.

The luminescence of neat **8** films prepared by PVD is extremely weak due to some quenching mechanism that we can only speculate about. We made an attempt of measuring the photoluminescence quantum efficiency (PLQE) of **8** thin films using a relative method rather than using an integrating sphere, which was not available to us at that time. The **8** thin films were excited with 325 nm radiation from a HeCd laser together with a thin film of TPD keeping the exactly same experimental conditions including reproducible geometry (i.e. the optical set up). Under such conditions one can neglect a small difference in the refractive indexes of the two materials which may alter the amount of light collected by the collimating lens that sends PL emission to the spectrometer with a silicon CCD detector.

TABLE 1	ε_{325}	A_{325}	d (nm)	1-T	PL I	PLI/(1-T)	PLQE
MF film	20850 [1]	0.20	96	0.37	2.2	6	~ 1%
MF/PMMA	20850	0.16	77 [2]	0.31	45	145	> 18%
TPD	65000 [3]	0.44	68	0.64	185	289	35% [3]

Table 3.1: Experimental data for PLQE estimate of 8 thin films.

[1] Extinction coefficient of **8** was estimated from the the absorbance of the neat XXXX films whose thickness was determined by a profilometer.
[2] An effective thickness of **8** film dispersed in the PMMA matrix; i.e. the thickness of a neat **8** film that corresponds to the **8** absorbance in PMMA matrix.
[3] H. Mattoussi *et al* 84, 2642 (1999).
[4] T is the transmittance of the thin films, PLI is the area under the PL curve and (1-T) quantity is linearly proportional to the number of photons absorbed by the thin film.

When normalized to the absorption of the incoming light (the 1-T quantity in Table 3.1), the PLQE of **8** can be estimated comparing its PL intensity with that of a TPD thin film (see Figure 3.3) whose PLQE is known.[3]

This approach gives PLQE of **8** on the order of 18% , which needs to be corrected for the spectral response of the silicon CCD (see Fig 3.3a).

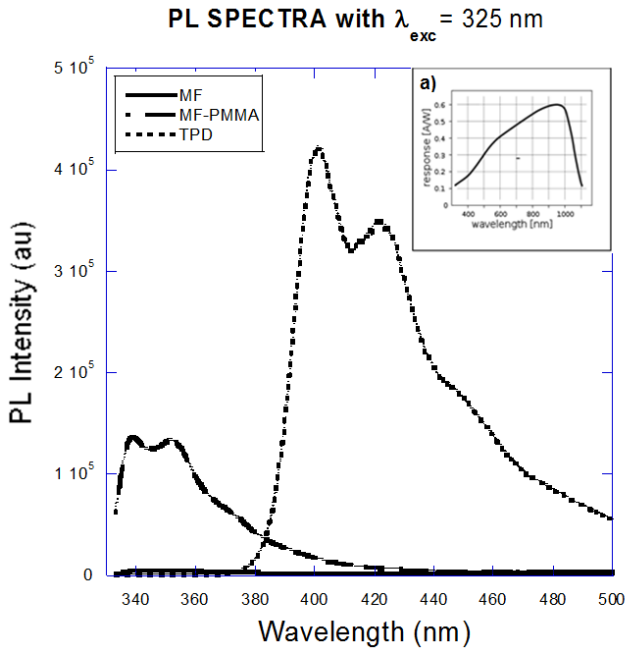

Figure 3.3: PL spectra of **8** and TPD thin films excited by a 325 nm radiation. a) Spectral response of a silicon photodiode.

We can see that the silicon detector is about twice more sensitive in the spectral area of TPD emission centred at 420 nm than at 360 nm. The latter corresponding to the peak of **8** emission. This gives PLQE of **8** on the order of 40%.

The remaining question concerns absolute energies of the **8** levels. For this we sent our films to Stpehen Berkenbile from the University of Graz who kindly measured the photoelectron emission of neat **8** films deposited n ITO. The method is based on the famous Einstein's photoelectric effect where the binding energy of the electron in the HOMO (the energy required to ionize the molecule) is determined form the difference between the energy of the photon (E=hν) and the kinetic energy of the electrons ejected from **8**. The report of Dr. Berkenbile is summarized below.

The ultraviolet photoemission spectra were recorded in a normal emission geometry using a SCIENTA SES200 hemispherical analyzer (acceptance angle 16°). Unpolarized HeI radiation (21.2 eV) was used with an incident angle of 45°. The system pressure during evaporation was about $5x10^{-9}$ torr. Nominal coverages for the uptake series can be derived by dividing the db number by the materials density. Assuming the latter on the order of 1.6 gr/cm^3 a monolayer coverage corresponds to roughly 24 db.

A growth series following the development of the valence band as a function of TTFB coverage is shown in Fig. 3.4, as observed by ultraviolet photoemission spectroscopy (UPS).

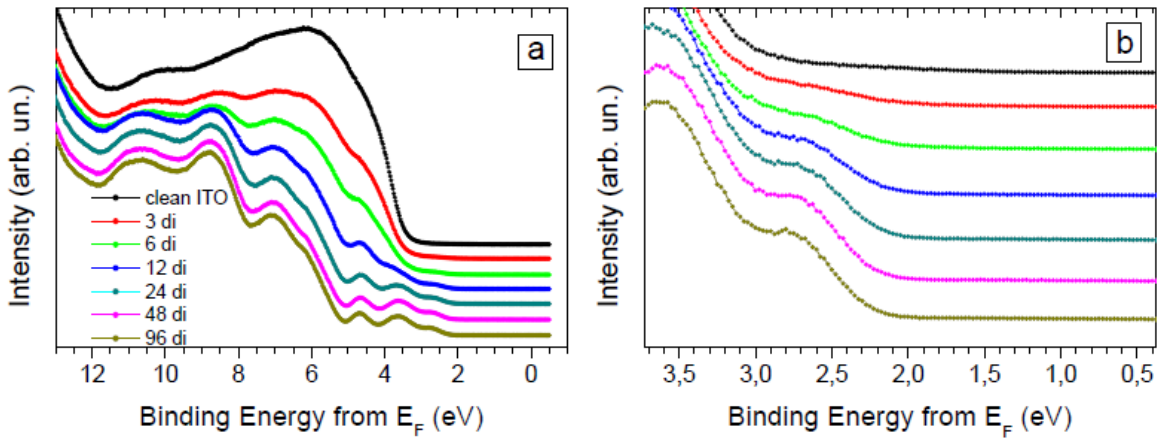

Figure 3.4: Valence band uptake of **8** measured with UPS. In (a) the entire valence band is shown. In (b) a close-up of the HOMO region is displayed with lines indicating the front edge of the HOMO emission.

The spectra are referenced to the Fermi level (E_F) of the ITO substrate and have been arbitrarily shifted vertically so that the uppermost spectrum is from clean ITO with increasing molecular coverages below. The strong ITO substrate features seen in the full UPS spectra of Fig. 3.4a are fully suppressed by the molecular signal at a coverage of 48 di, indicating that the substrate is completely covered at this point. No change in the molecular valence band is then seen up to a coverage of 96 di. At higher coverages (not shown) a significant rigid shift

to higher binding energies is observed. Such shifts are suggestive of a charging of the films during photoemission, perhaps due to islanding of the molecules on the initial layers.

In Fig. 3.4(b), the region containing the HOMO of the **8** is shown in detail. The peak of the HOMO emission can be observed at all coverages between the binding energies of 2.6 and 2.8 eV. The band alignment of the HOMO with respect to the Fermi level is found by extrapolating the slope of the front edge of the emission peak to zero intensity, as indicated by the intersection of the two lines for each spectrum. The initial **8** coverage, less than a complete first layer, has a band alignment of 2.01 eV. The band alignment then exponentially decreases with increasing coverage to a value of 2.23 eV in the completed thin film of 96 di. This small difference in the band alignment between the initially deposited molecules and the thin film can occur either due to charge transfer between at the organic/inorganic interface or due to a higher extramolecular screening of the photohole for molecules near the interface. Further experiments could clarify this point.

From the above report we can see that the first photoelectrons were detected at ~ 2.2 eV in respect to the Fermi level of ITO, which was found lay at ~ 4. EV below the vacuum level. Note that we take the onset of the valance band photoemission rather than the its maximum, because this is a more appropriate value for combining with the band gap data obtain by optical methods. The Fermi level of ITO in this study appears to be a bit low as it is normally found to be around 4.5 eV. Nevertheless, it is known from the literature that the ITO Fermi level is highly dependent on the surface preparation procedure and can vary for more than 0.5 eV[13]. Based on the UPS photoemission results we can set the absolute values of the **8** HOMO level at 6. 2. eV below the vacuum. The LUMO energy level at 2. 6 eV was found by subtracting the band gap energy of **8** obtained by optical studies (Eg = 3.6 eV) form the HOMO energy (see Figure 3.5).

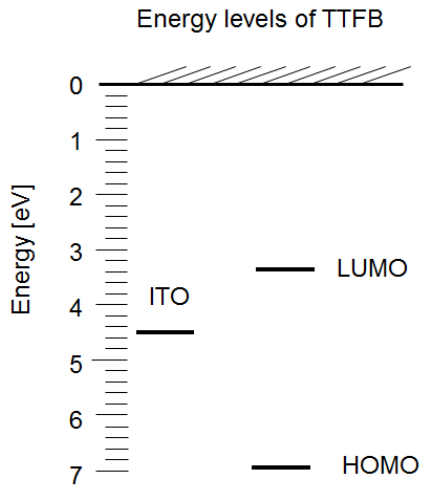

Figure 3.5: Absolute values of the HOMO and LUMO levels of **8** in respect to vacuum

3.4 Conclusion

A novel trifluorene compound, functionalized in position 3 and 6 with 2 methoxy groups, that can be used as efficient UV emitter in UV OLEDs and as effective host materials for electrophosphorescent devices have been successfully synthesized and characterized. The reason for introducing the methoxy group was dual: to improve the fluorescence efficiency by adding an electron donor and to increase the conjugation length, resulting in a slight red-shift of the fluorescence. The new trifluorene chromophore **8** presents good emissive properties in solution (PLQE = 47% in CH_2Cl_2 solution) while a quenching in the pure film emission is observed. On the contrary, PLQE of compound **8** dispersed in PMMA matrix is 18 times higher than that of a neat **8** film, indicating a severe concentration quenching effect. Nevertheless the PL spectrum of **8** at the edge of the UV/VIS region suggests a possible down-conversion application in white organic light-emitting diodes (WOLEDs).

3.5 Experimental section

3.5.1 General methods

All reagents and solvents were purchased from Sigma Aldrich and were used as received or purified using standard procedures. NMR spectra were recorded at room temperature on a Bruker Avance DRX 400 MHz. The chemical shifts δ are expressed in ppm relative to tetramethylsilane as internal standard. The multiplicity of the ^{1}H spectra is expressed as follows:

s = singlet; d = doublet; dd = doublet of doublet; t = triplet; m = multiplet.

When possible mass spectra (VG Autospec M256) and elemental analysis (Perkin-Elmer CHN 2400) have also been performed.

3.5.2 Synthesis of 3,3'-dimethoxybiphenyl (1)

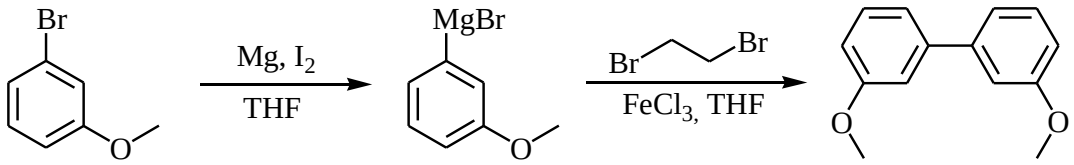

A dried three-necked flask equipped with a magnetic stirrer, thermometer and condenser was charged under nitrogen with THF (50 ml) a solution of $FeCl_3$ (0.03 eq) in THF and 1,2-dibromoethane (4.16 ml, 0.6 eq). A solution of aryl Grignard reagent (3-Bromo-anisole 10.16 ml in 50 ml of THF and 2.95 g of Mg) was added at once via a syringe to the resulting yellow-green solution. The colour immediately changed to dark brown and the temperature increased. The resulting mixture was stirred at room temperature for 4h then hydrolyzed with a 1M HCl solution. After extraction with methylene chloride, the combined organic layers were dried over magnesium sulphate and concentrated by rotary evaporation. The residue was purified by column chromatography (methylene chloride/hexane) to afford 6.4 g (74 %) of a colorless oil.

^{1}H-NMR (400MHz, $CDCl_3$): 3.92 (s, 6H), 6.98 (ddd, 2H), 7.22 (t, 2H), 7.26 (dt, 2H), 7,42 (t, 2H)

^{1}H-NMR (400MHz, $CDCl_3$):

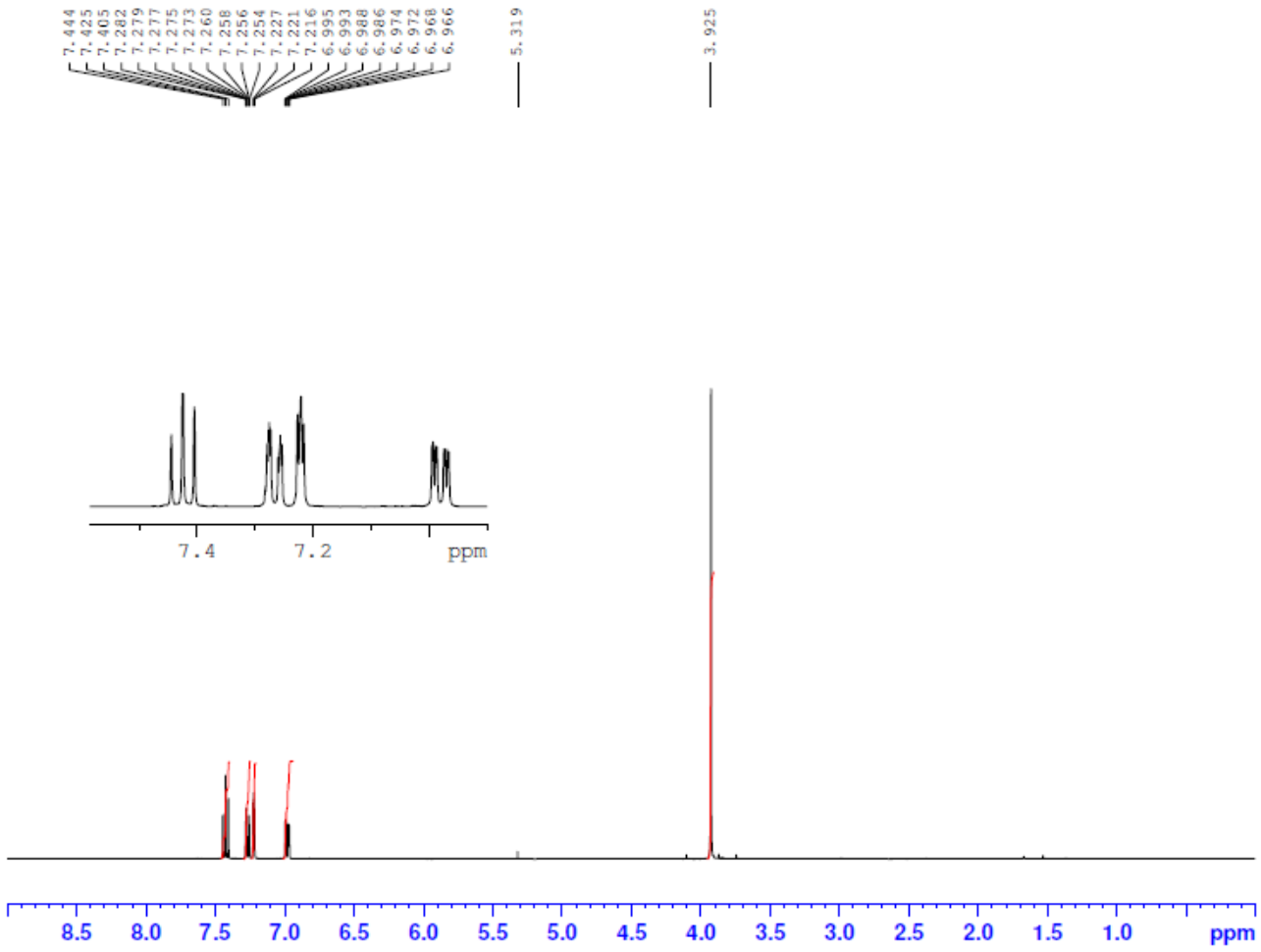

3.5.3 Synthesis of 2-Bromo-3,5-dimethoxybiphenyl (2)

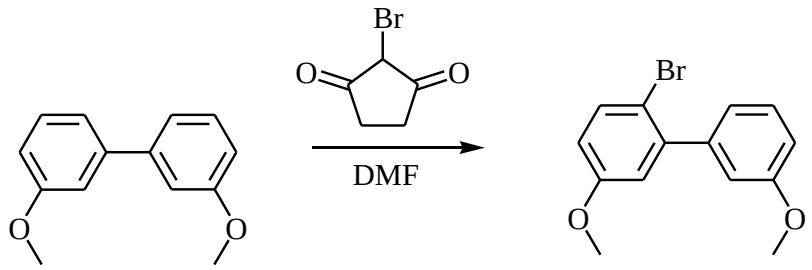

1 (5.0 g, 23.34 mmol) was dissolved in dimethylformamide. N-Bromosuccinimide (4.15 g, 23.34 mmol) was dissolved in dimethylformamide (63 mL) and added slowly to a solution of 3,3-dimethoxybiphenyl. The mixture was stirred at room temperature for about 16 h. Afterwards the reaction mixture was transferred to a separatory funnel and added to Et_2O and de-ionized water. The Et_2O solution extracted and washed with water and saturated NaCl. The combined organic phase was concentrated under reduced pressure and purified by flash column chromatography to give 6.7 g (98%) of compound **2** as colorless oil.

^{1}H NMR (400 MHz, $CDCl_3$): 3.83 (s, 3H), 3.87 (s, 3H), 6.81 (dd, 1H, J_1 = 8.8 Hz and J_2 = 3.1 Hz), 6.92 (d,1H, J = 3.1 Hz), 7.03–6.95 (m, 3H), 7.37 (t, 1H, J = 7.7 Hz), 7.56 (d, 1H, J = 8.8 Hz);

HRMS (EI+) calculated for $C_{14}H_{13}BrO_2$ *m*/*e* 292.009, found 292.009

^{1}H NMR (400 MHz, $CDCl_3$):

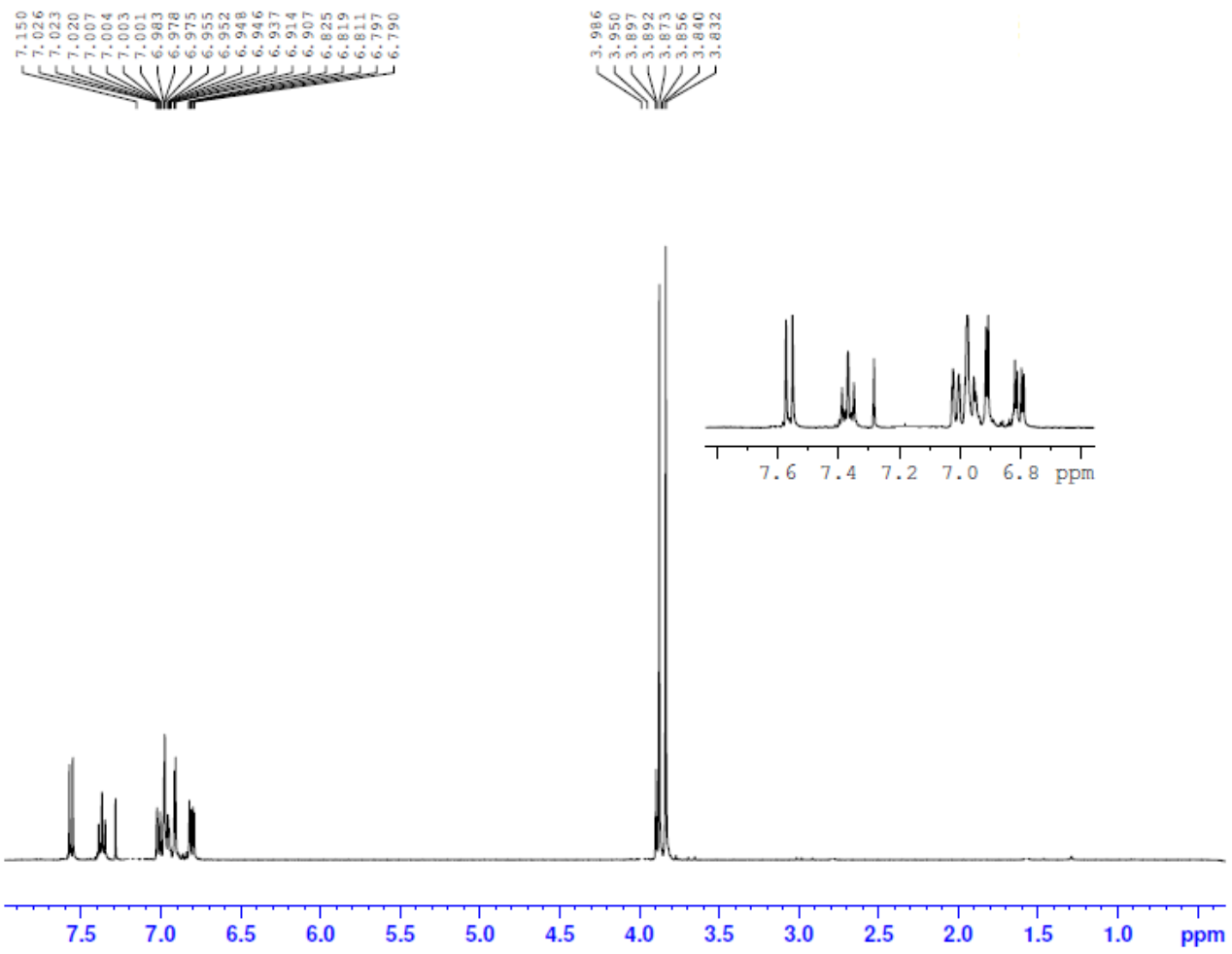

3.5.4 Synthesis of 3,5-Dimethoxy-[1,1-biphenyl]-2-carboxylic Acid (3)

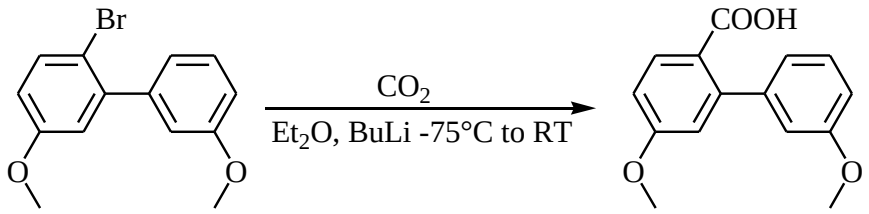

A solution of **2** (13.3 g, 45.4 mmol) in diethyl ether (400 mL) was stirred at -45 °C under dry N_2 and treated dropwise with a solution of *n*-butyllithium (25 mL, 2.5 M in hexane, 62 mmol). After 15 min, Dry ice was added through the mixture, and the temperature was allowed to rise to 25 °C. The resulting mixture was acidified with aqueous 1 M HCl and extracted with diethyl ether. The organic phase was washed with water and brine, dried over $MgSO_4$, and filtered. Volatiles were removed by evaporation under reduced pressure, and the residue was crystallized from acetone/pentane to afford 3,5-dimethoxy-[1,1-biphenyl]-2-carboxylic acid (11.3 g, 43.8 mmol, 96%) as a light yellow solid.

^{1}H NMR (400 MHz, $CDCl_3$): 7.99 (d, 1H, J = 8.7 Hz), 7.30 (t, 1H, J = 8.0 Hz), 6.94-6.87 (m, 4H), 6.84 (d, 1H, J = 2.6 Hz), 3.87 (s, 3H), 3.83 (s, 3H);

^{1}H NMR (400 MHz, $CDCl_3$):

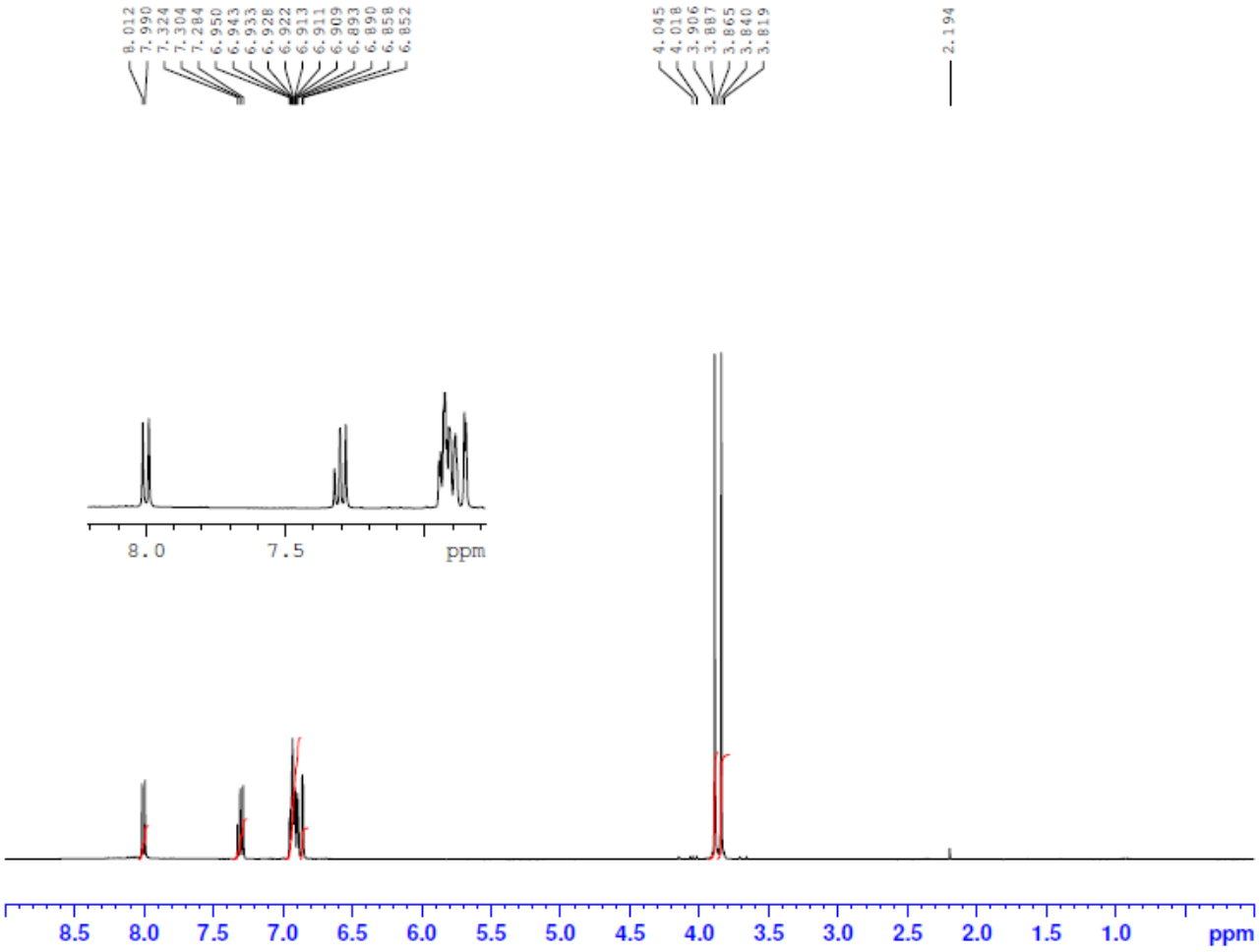

3.5.5 Synthesis of 3,6-Dimethoxy-9-fluorenone (4)

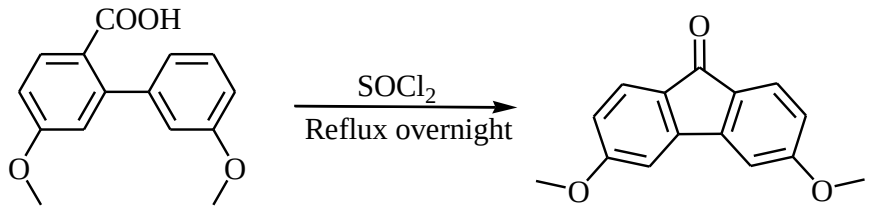

A solution of acid **3** (4,16 g, 16,1 mmol) in thionyl chloride was stirred at reflux for 20 h. The solution was cooled to room temperature and concentrated in vacuo to afford a yellow residue. The mixture was extracted with dichloromethane and the extracts dried over magnesium sulphate, filtered, concentrated by rotary evaporation. The crude product was purified by column chromatography (ethyl acetate/hexane) to afford 2,2 g (76 %) of a yellow solid.

^{1}H-NMR (400MHz, $CDCl_3$): 3.91 (s, 6H), 6.750 (d of d J_1 = 8, J_2 = 2 Hz, 2H), 6.98 (s, J = 2 Hz, 2H), 7.58 (d, J = 8 Hz, 2H).

^{13}C-NMR (100MHz, $CDCl_3$): 55.74, 107.04, 113.02, 125.41, 128.31, 145.89, 165.00, 191.36.

^{1}H-NMR (400MHz, $CDCl_3$):

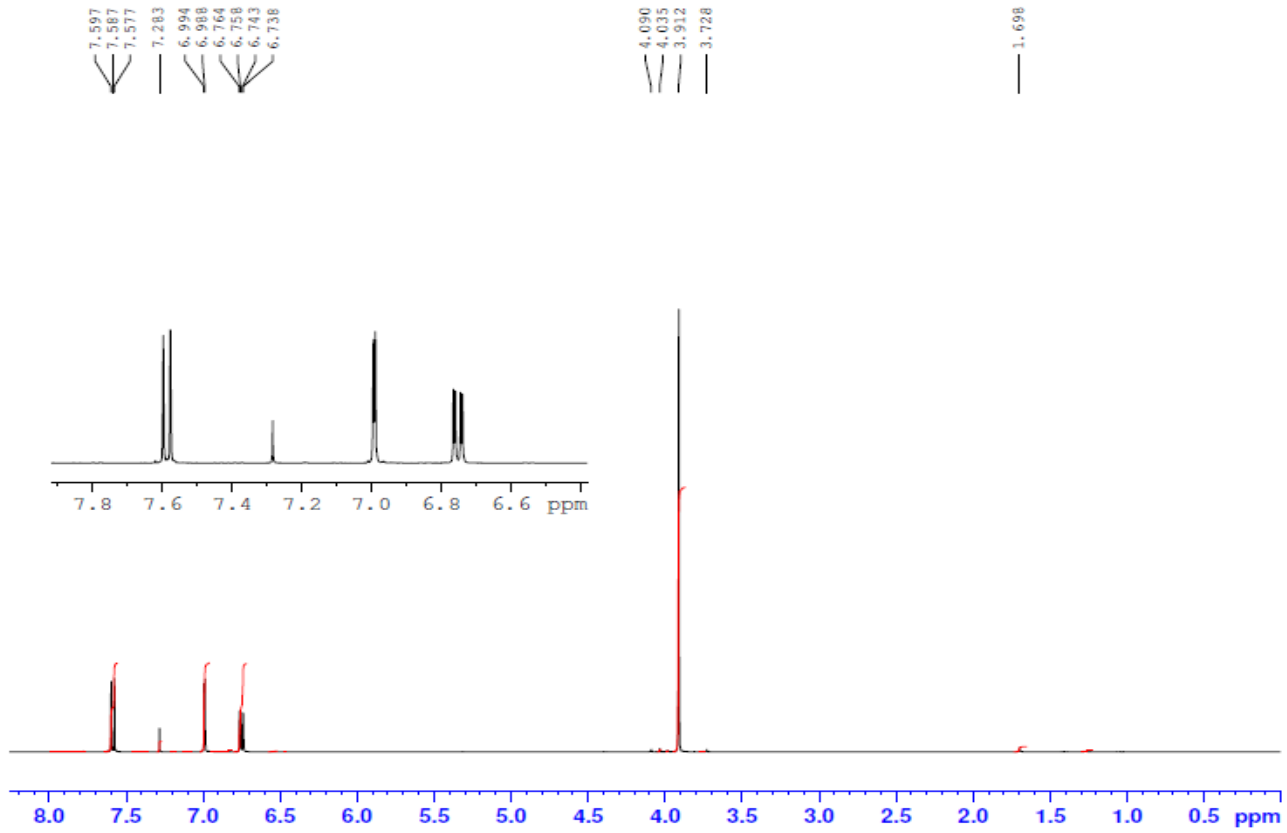

^{13}C-NMR (100MHz, $CDCl_3$):

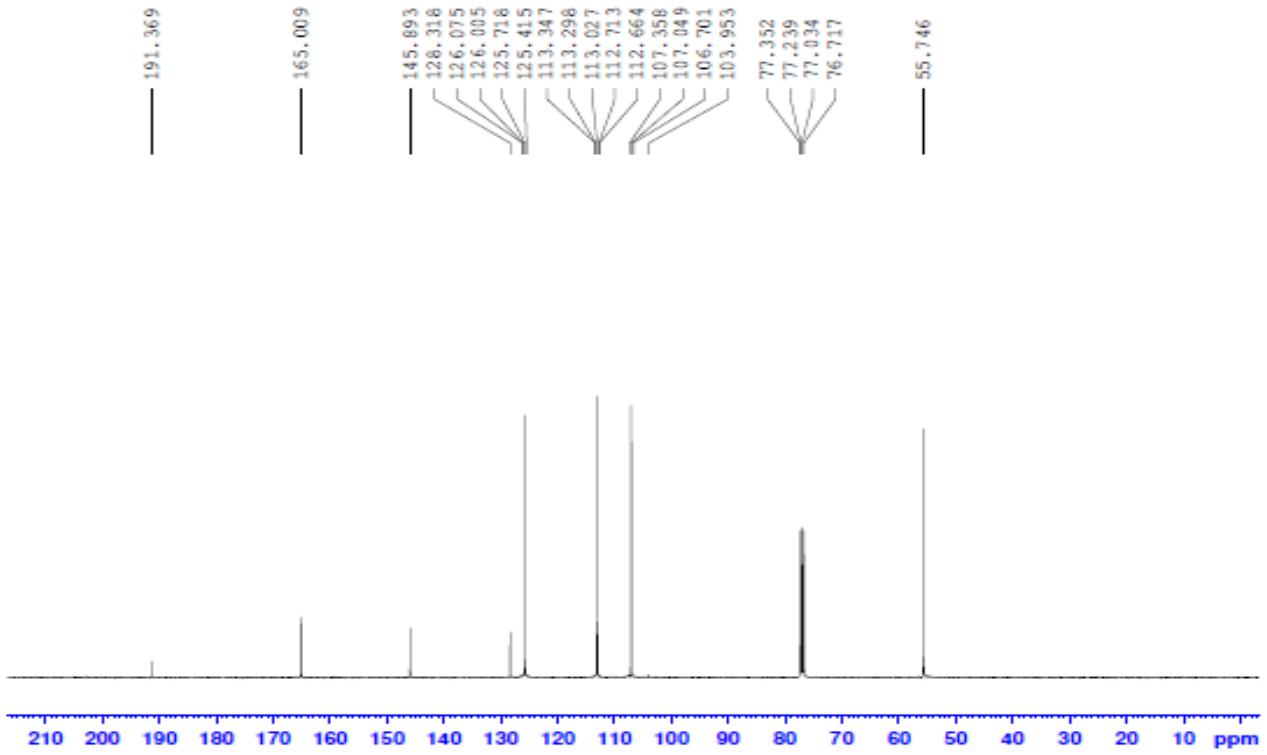

3.5.6 Synthesis of 9-(3-bromo-5-(3,9-dimethoxy-9H-fluoren-9-yl)phenyl)-3,6,9-trimethoxy-9H-fluorene (6)

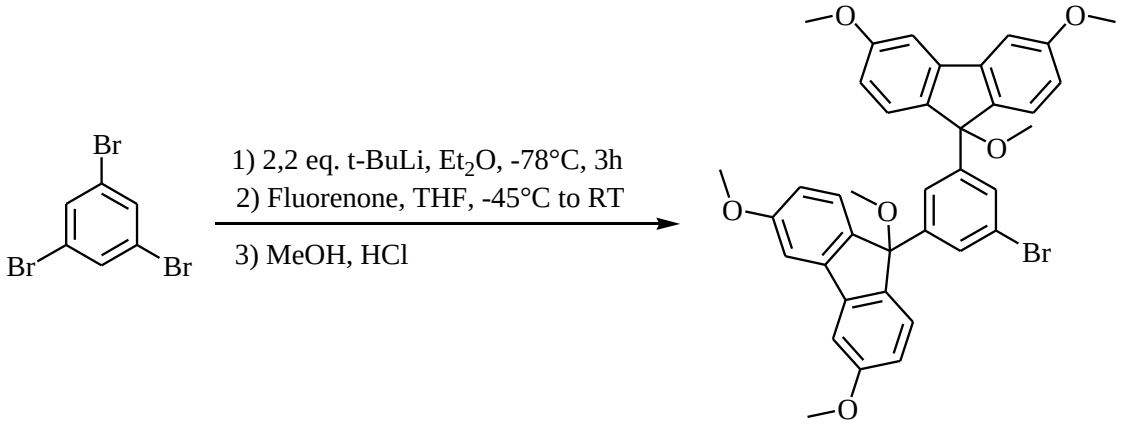

A solution of tribromobenzene (0.4 g, 1,2 mmol) in Et_2O (30 ml) was cooled to -75 °C and was added 1,5 M *t*-BuLi (2 ml, 3 mmol) dropwise via syringe and let stir for 30 min. To this was added a second solution of **4** (0,46 g, 2,5 mmol in 30 ml of THF at 0°C) via canula and stirred for 3 h at -45-40°C. The reaction was quenched with a saturated solution of NH_4Cl and extracted with CH_2Cl_2.The extracts dried over magnesium sulphate, filtered, concentrated by rotary evaporation to give a solid. A suspension of solid in MeOH and 0,5 ml of HCl conc. was stirred a reflux for a 3h. A white solid was collected by filtration, washed with methanol to give 256 mg of **6** (32%).

^{1}H-NMR (400MHz, $CDCl_3$): 2.90 (s, 6H), 3.90 (s, 12H), 6.79-6.84 (dd, 4H), 7.08 (d, 4H), 7.14 (d, 2H), 7.16 (d, 4H), 7.64 (t, 1H).

^{13}C-NMR (100MHz, $CDCl_3$): 15.52, 55.54, 58.39, 105.32, 113.93, 121.88, 122.44, 125.96, 127.35, 135.81, 141.87, 146.13, 160.68.

^{1}H-NMR (400MHz, $CDCl_3$):

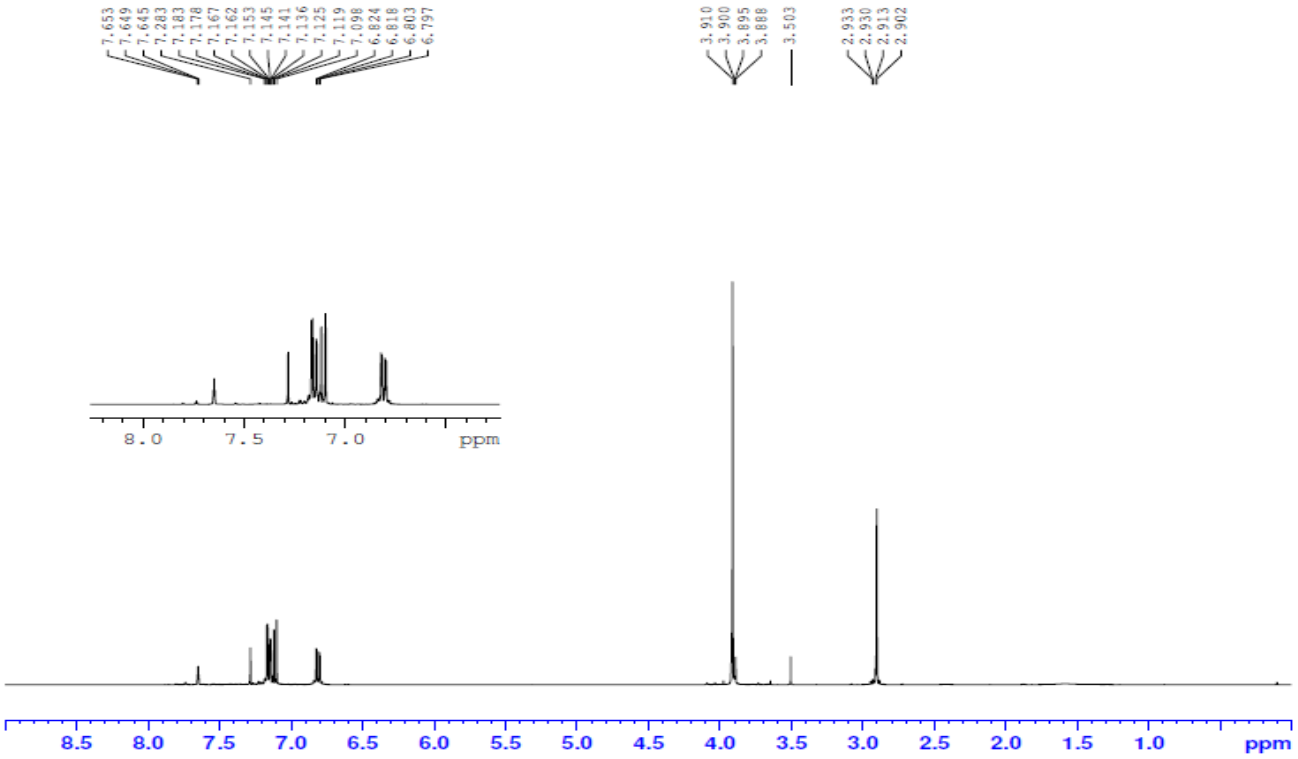

^{13}C-NMR (100MHz, $CDCl_3$):

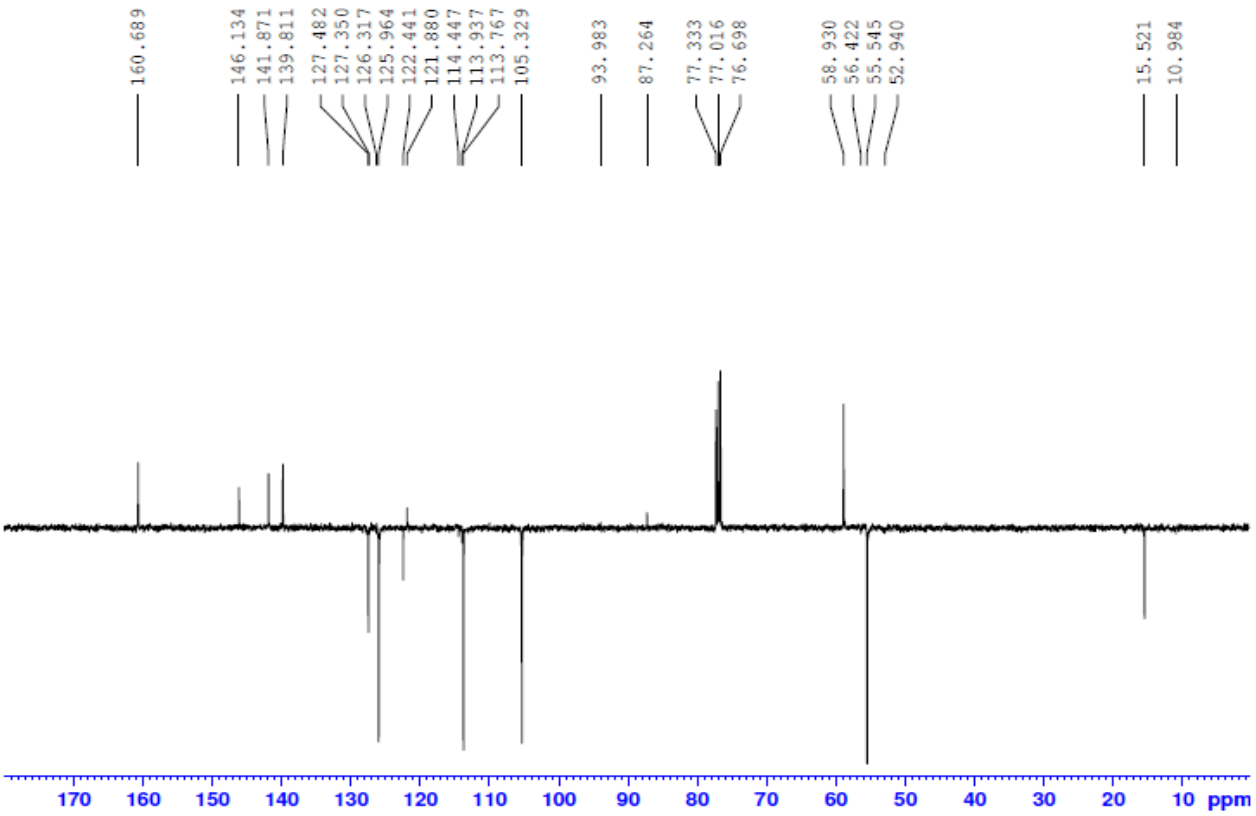

3.5.7 Synthesis of 1,3,5-tris(3,6,9-trimethoxy-9H-fluoren-9-yl)benzene (8)

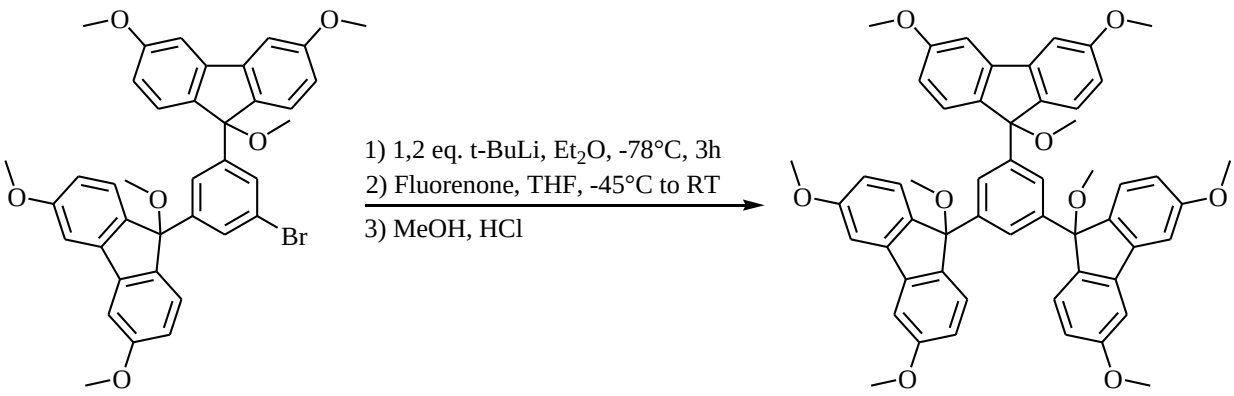

A solution of **6** (0.284g, 0,4 mmol) in Et_2O (20 ml) was cooled to -75 °C and was added with *n*-BuLi 1.5 M (0,3 ml, 0.45 mmol) dropwise via syringe and let stir for 15 . To this was added a second solution of 3,6.dimethoxy-9-fluorenone (0,077 g, 0,4 mmol in 10 ml of THF at 0°C) via canula and stirred for 3 h at -45 to -30°C. The reaction was quenched with saturated solution of NH_4Cl and extracted with CH_2Cl_2.The extracts dried over magnesium sulphate, filtered, concentrated by rotary evaporation to give a solid. A suspension of solid in MeOH and 0,5 ml of HCl conc. was stirred at reflux for 3h. A white solid was collected by filtration, washed with methanol to give 192 mg of **8** (54%).

^{1}H-NMR (400MHz, $CDCl_3$): 2.87 (s, 9H), 3.89 (s, 18H), 6.73 (dd, J_1 = 8.34 Hz, J_2 = 2.38 Hz , 6H), 7.04 (d, J =8.51 Hz, 6H), 7.08 (d, J = 2.55 Hz, 6H), 7.21 (s, 3H).

^{13}C NMR (100 MHz, $CDCl_3$): 51.16, 55.49, 88.33, 105.16, 113.51, 122.84, 125.54, 139.74, 142.05, 142.80, 160.51.

^{1}H-NMR (400MHz, $CDCl_3$):

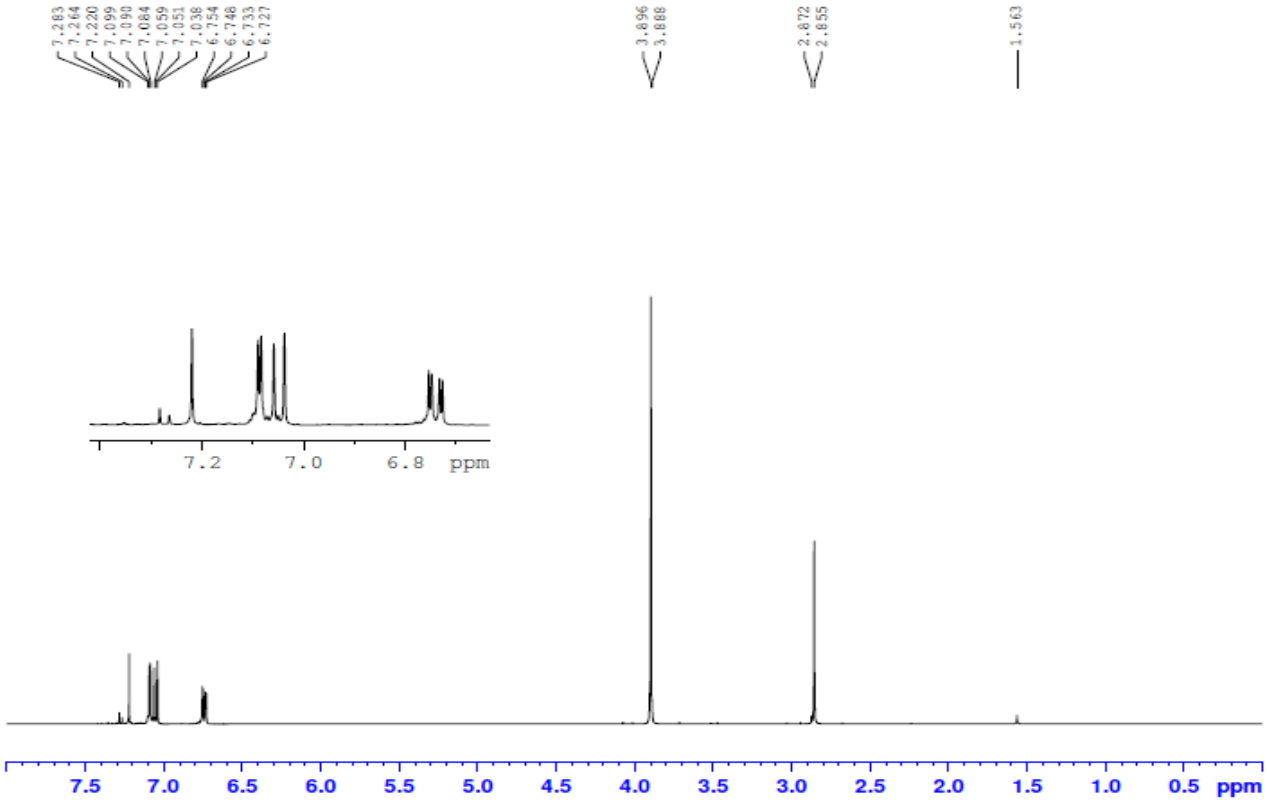

^{13}C NMR (100 MHz, $CDCl_3$):

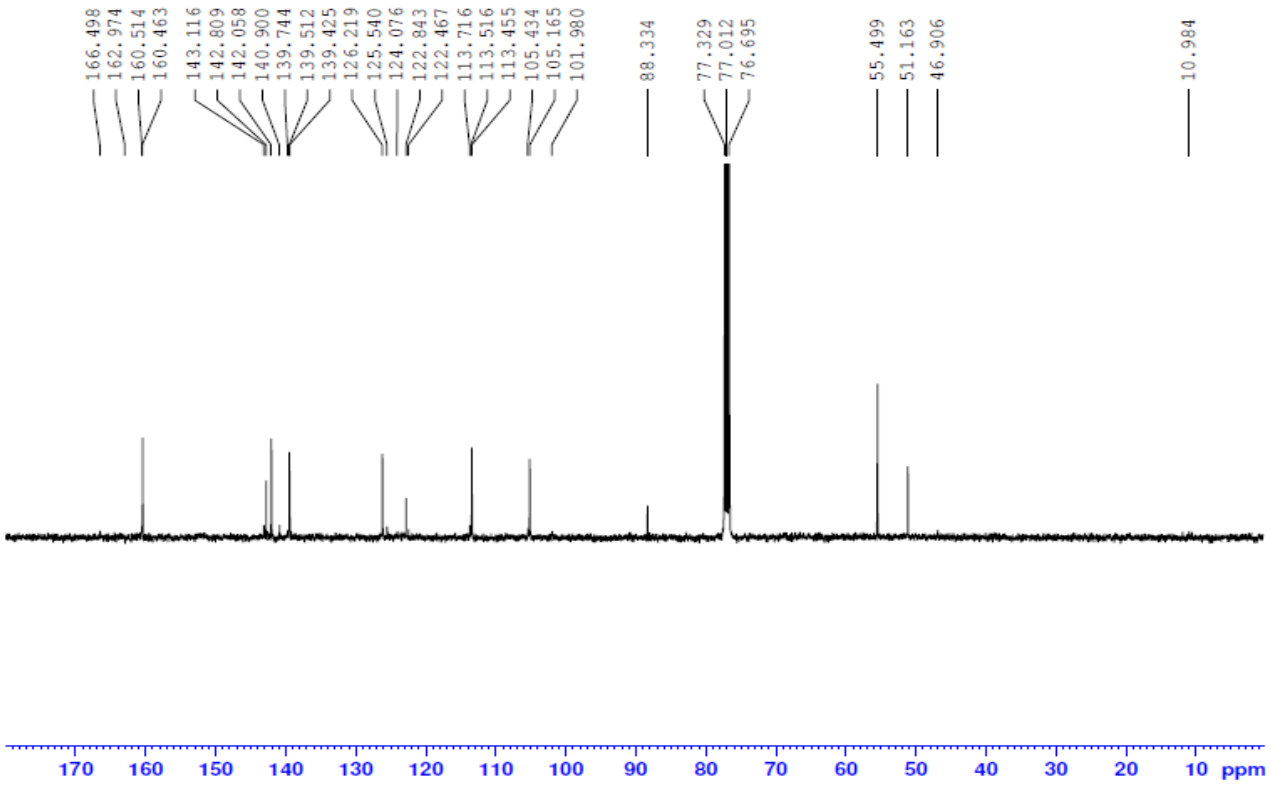

3.6 References

[1] Tang CW, Van Slyke SA. *Appl. Phys. Lett*. **1987**; 51: 913.

[2] Ahn K, Ryu GY, Youn S, Shin D. *Mat. Sci. Eng. C* 2004; 24: 163. a) Chen Z, Yu J, Ogino K, Miyata S. *J. Phys. D Appl. Phys*. **2002**; 35: 1099. b)Zhou Q, Qin A, He Q, Lei G, Wang L, Qiu Y, Ye C, Teng F, Bai F. *J. Lumin*. **2007**; 122: 674.

[3] Fang Q, Xu B, Jiang B, Fu H, Zhu W, Jiang X, Zhang Z. *Synthet. Met*. **2005**; 155: 206. b) Han M, Lee S, Jung J, Park K, Kwon S, Ko J, Lee PH, Kang Y. *Tetrahedron* **2006**; 62: 9769. c) Tang C, Liu F, Xia Y, Lin J, Xie L, Zhong G, Fan Q, Huang W. *Org. Electron*. **2006**; 7: 155.

[4] Chen X, Tseng HE, Liao JL, Chen SA. *J. Phys. Chem. B* **2005**; 109: 17496. a) Zeng G, Yu WL, Chua SJ, Huang W. *Macromolecules* **2002**; 35: 6907. b) Grell M, Bradley DDC, Ungar G, Hill J, Whitehead KS. *Macromolecules* **1999**; 32: 5810. c) Lemmer U, Heun S, Mahrt RF, Scherf U, Hopmeier M, Siegner U, Göbel EO, Müllen K, Bässler H. *Chem. Phys. Lett*. **1995**; 240: 373. d) Lee JI, Klärner G, Miller RD. *Chem. Mater*. **1999**; 11: 1083. e) Conwell E. *Trends. Polym. Sci*. **1997**; 5: 218. f) Cimrova V, Scherf U, Neher D. *Appl. Phys. Lett*. **1996**; 69: 608. g) Weinfurter KH, Fujikawa H, Tokito S, Taga Y. *Appl. Phys. Lett*. **2000**; 76: 2502. h) Bliznyuk VN, Carter SA, Scott JC, Klärner G, Miller RD. *Macromolecules* **1999**; 32: 361.

[5] Yu WL, Pei J, Huang W, Heeger AJ. *Adv. Mater*. **2000**; 12: 828.

[6] Pogantsch A, Wenzl FP, List EJW, Leising G, Grimsdale AC, Müllen K. *Adv. Mater*. **2002**; 14: 1061.

[7] Klärner G, Lee JI, Lee VY, Chan E, Chen JP, Nelson A, Markiewicz D, Siemens R, Scott JC, Miller RD. *Chem. Mater*. **1999**; 11: 1800.

[8] Wu FI, Dodda R, Reddy DS, Shu CF. *J. Mater. Chem*. **2002**; 12: 2893.

[9] K.S. Yook et al. Organic Electronics 10 (2009) 1378–1381.

[10] Mo Y., Tian R., Shi W. and Cao Y., *Chem. Commun.*, **2005**, 4925.

[11] Rizzo A., Solin N., Lindgren L. J., Andersson M. R., and Inganas O., *Nano Lett.* **2010**, *10*, 2225.

[12] Zhonglian Wu, Yan Xiong, Jianhua Zou, Lei Wang, Jincheng Liu, Qiliang Chen, Wei Yang, Junbiao Peng, and Yong Cao, *Adv. Mater*., **2008**, *20*, 2359.

[13] M. Andreasson *et al.*, *Organic Electronics*, **2005**, *6*, 175.

4 Synthesis and characterization of pyrene chromophores for NLO applications and optical devices.

4.1 Introduction

Materials possessing nonlinear optical (NLO) properties have been proven to be very useful for a variety of applications, spanning modulation of optical signals, microfabrication, sensing, and medical imaging. Inorganic NLO materials such as lithium niobate ($LiNbO_3$) or potassium dihydrogen phosphate (KH_2PO_4) are known to exhibit second harmonic generation (SHG) effect and have been used in lasers over the last 40 years.[1] During the 1990's also organic materials were identified as promising candidates for nonlinear optical applications.[2] Such compounds offer the advantages of larger optical nonlinearity and faster optical response and large efforts in fundamental research have been devoted in the last decades to improve their performances as 2nd order NLO materials.[3,4]

For applications in optical devices, materials have to possess not only significant molecular response, but also attributes like chemical, photochemical and thermal resistance, must be easy to produce and process and with long term optical properties.

One of structural motifs that has been recognized to be successful for obtaining molecules with high 2nd order NLO response, is the push-pull structure in which a donor and acceptor group are separated by a π-coniugated bridge. The result of such structure is a molecule in which polarization in one direction is easier than in the opposite direction.

In this chapter I report about the synthesis of novel 2nd order NLO chromophores based on pyrene moiety. Pyrene is a polycyclic aromatic hydrocarbon consisting of four fused benzene rings, resulting in a flat aromatic system, which chemical structure is shown in Figure 4.1

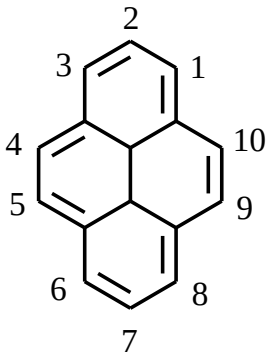

Figure 4.1

In the last four decades, a number of works have been carried out and published which included both the theoretical and experimental investigation of pyrene concerning on its electronic structure, UV-Vis absorption and fluorescence emission spectrum[5]. Recently pyrene has proved as potential component for advanced materials and different structural derivatives were reported as useful materials in field effect transistors, photovoltaic cell, light emitting diodes etc. Due to optoelectronic properties, pyrene is not only limited to the these applications but also used in the field of ionic[6] and molecular recognition.[7] While it is widely employed in applications that exploit its outstanding fluorescence properties (long lifetime and high quantum yield),[8] there are no reports on second order NLO properties of pyrene-based structures.

We decided to prepare a pyrene derivative containing a pyridine moiety, that could be eventually exploited for the preparation of push-pull chromophores and for complexation to different metals. To our knowledge there is only one report in the literature for such compound, which has been used as fluorescent probe as strong sensor of surface charge of lipid vesicles and micelles.[9]

4.2 Experimental procedure for the synthesis of pyrene derivatives

Compound **1** was obtained by Heck coupling of 1-bromo-pyrene and 4-vinylpyridine in the presence of dicyclohexylmethylamine (which acts as Base/HBr scavenger), catalyzed by $[Pd[P(tBu)_3]_2]$ in dry toluene for 24 h at 80 °C. Since oxygen can inhibit the action of the catalyst, it is necessary to remove it completely from the reaction mixture. The latter action was performed through 3 freeze-pump-thaw cycles.

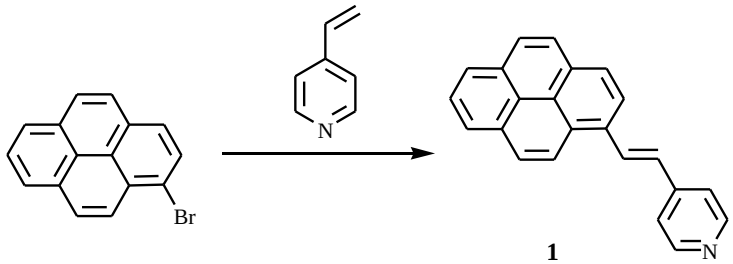

1

The reaction crude in this way was then purified through column chromatography on silica gel using dichloromethane-hexane 7/3 as eluent. Crystallization from dichloromethane-hexane afforded a straw-yellow solid in 65% yield. Compound **1** was characterized through ^{1}H-NMR, ^{13}C-NMR, mass spectroscopy and elementary analysis (see experimental section).

Interesting, the measurements of its second order NLO properties, by EFISH technique, revealed a μβ value strongly dependent on the concentration.

1	Conc (M)	μβ (*10^{-48} esu)
	10^{-3}	203
	10^{-4}	2200
	$5\ 10^{-5}$	2660

At high concentrations the decrease in the NLO response seems to point to the formation of central symmetrical aggregates. This phenomenon is also evident in the emission spectra of **1** in $CHCl_3$ solution at various concentrations (see Figure 4.2). In particular, the spectra macroscopically change when shifting from the 10^{-3} M to the 10^{-4} M solution, a shift that is also critical in the variation of the NLO response.

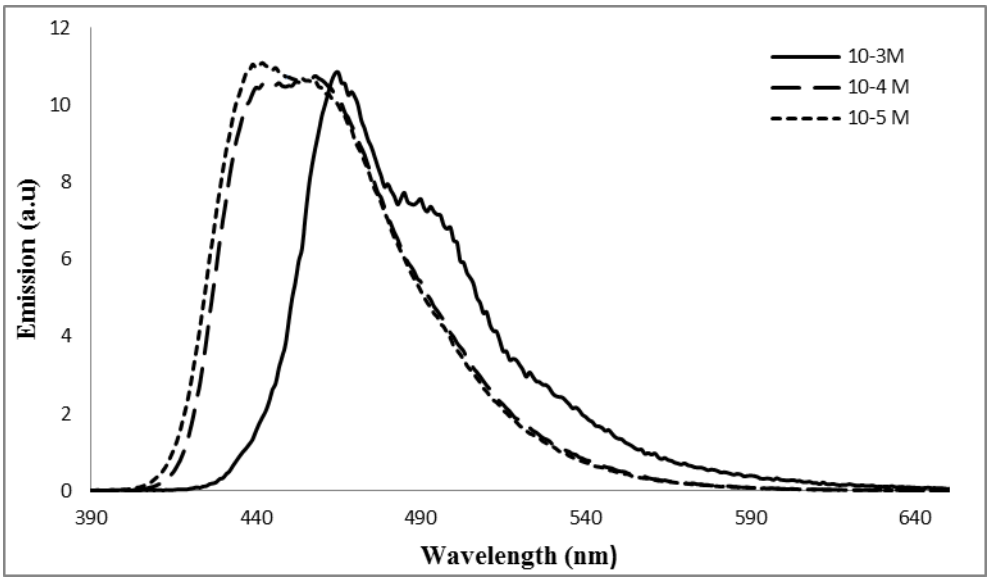

Figure 4.2: Variation in the emission spectra of the compound **1** at different concentrations

This variation, on the other hand, is not present in the electronic absorption spectra in fact, as the Figure 4.3 shows, the position and shape of the absorption band don't change with the concentration.

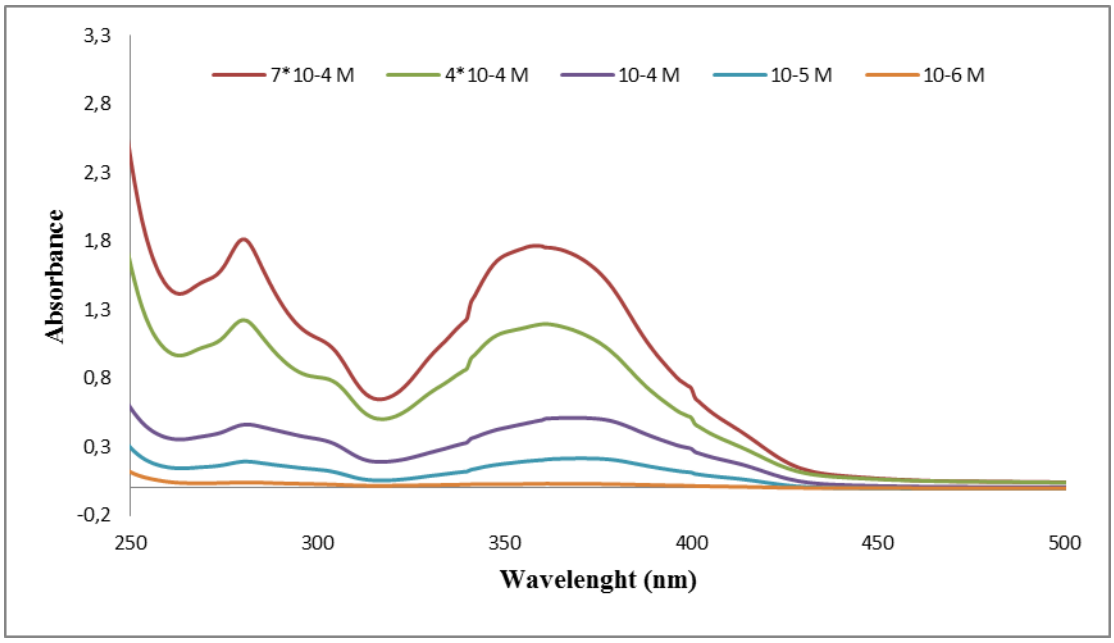

Figure 4.3: Absorption spectra of compound **1** at different concentrations

The fluorescence quantum yield of the compound in $CHCl_3$ solution, using Coumarine 503 in methanol as standard, is equal to 64%. In the solid state the compound displays a structured emission band centered at 500 nm (figure 4.4).

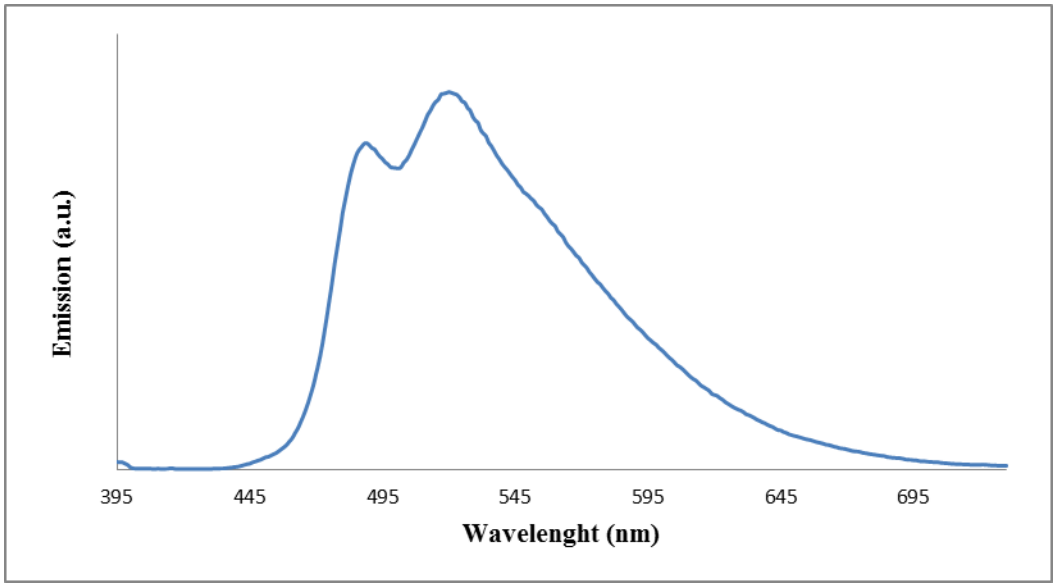

Figure 4.4: Emission spectrum of compound **1** at solid state

Recently, a high interest focused on emitting molecules whose properties are influenced by external stimuli as, for instance, the presence of vapours from volatile organic compounds (VOC) (vapochromism), acid or basic vapours (acid chromism), viscosity of the matrix in which they are dissolved (viscochromism), variations in the pressure (piezochromism,

mechanic chromism), etc. The idea is to exploit this variation of the emission properties in order to build luminescent sensors.

We studied the effect of the exposition to acids on the emission behaviour of this compound. When **1** at the solid state is exposed the HCl vapours, it is protonated to give the pyridinium chloride **2**, which is characterized by a red colour. The reaction is complete after 12 hours at room temperature.

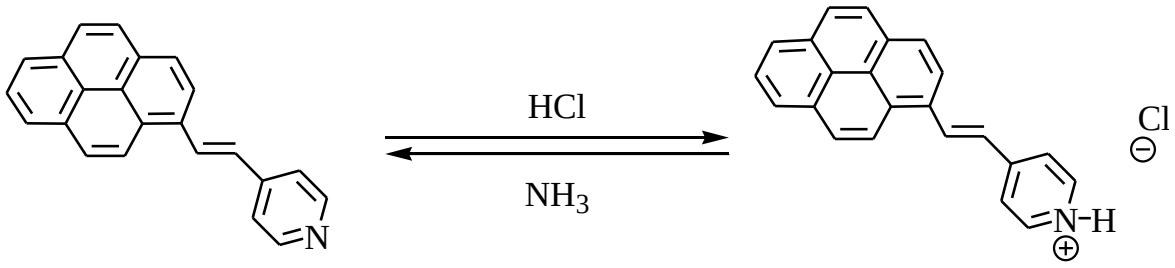

1 **2**

Also the emission spectra in the solid state change after protonation.(see figure 4.5).

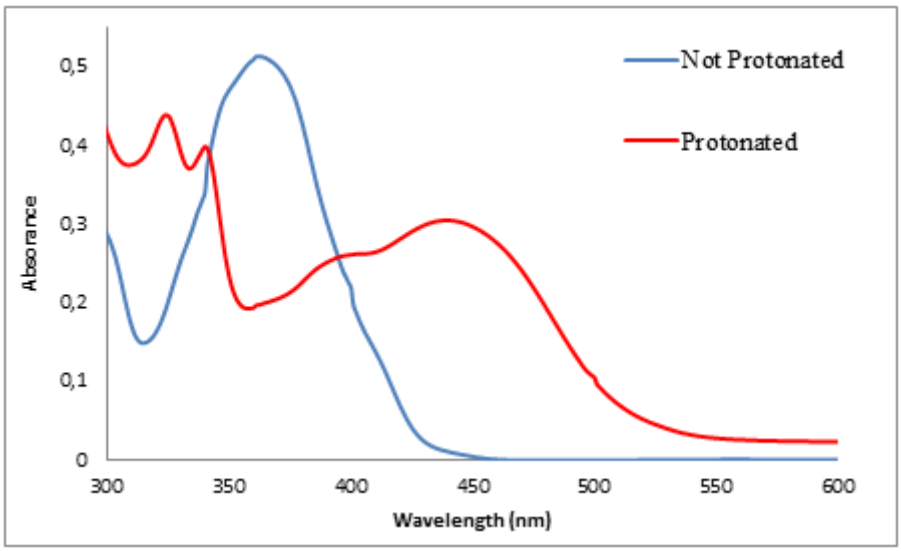

Figure 4.5: Emission spectra from powder for compounds **1** and **2**

The protonation reaction, that is totally reversible for exposition of **2** to ammonia vapours, can also be followed by UV-Vis spectroscopy in solution, as evidenced from the absorption and emission spectra reported in Figure 4.6 and Figure 4.7.

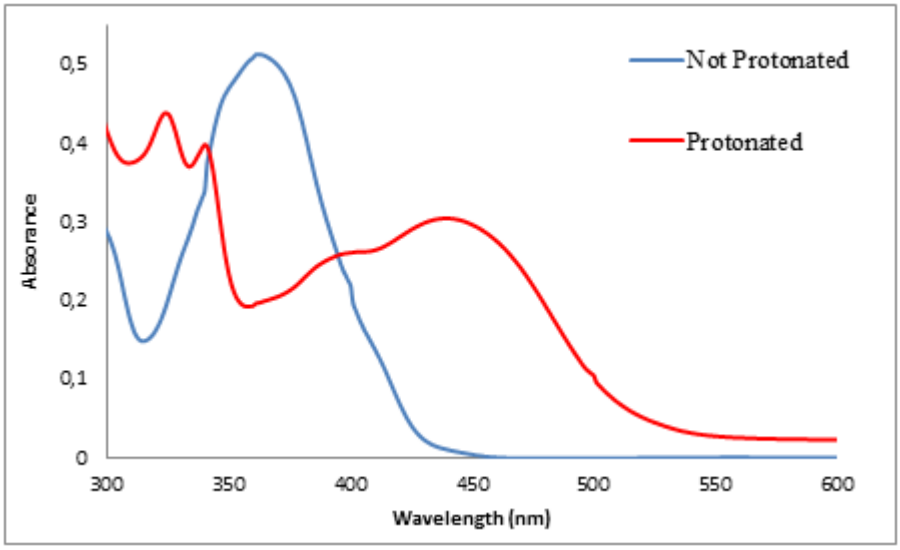

Figure 4.6: Absorption spectra of compounds **1** and **2** in $CHCl_3$ solution.

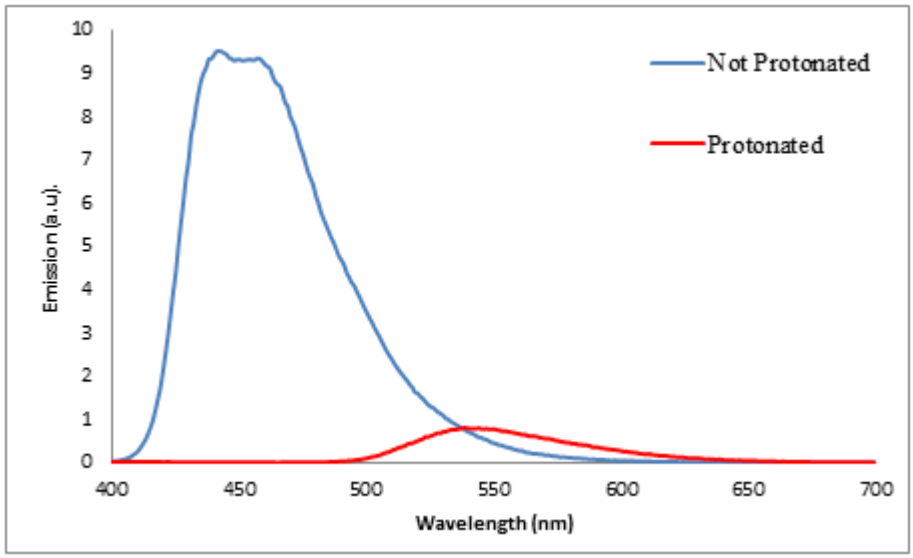

Figure 4.7: Emission spectra of compounds **1** and **2** in $CHCl_3$ solution.

As shown in the emission spectra, the protonated species not only displays a strongly red shifted band, but its intensity is also quite lowered with respect to **1**. The quantum yield of **2** in $CHCl_3$, using as standard quinine sulphate, was equal to 19%.

Interestingly, the emission spectra of *2* at different concentrations do not show substantial changes, revealing that no aggregates form by increasing concentration.

Such behavior is confirmed by the measurements of 2^{nd} order NLO response by EFISH, which shows a μβ value quite similar for different concentrations.

2	Conc (M)	μβ ($*10^{-48}$ esu)
	$7.2\ 10^{-4}$	414
	10^{-4}	525

This latter result is quite unexpected since, according to the push-pull model, **2** which bears the more withdrawing pyridinium group, should have a stronger dipole moment than **1** and therefore a stronger NLO response.

Electronic density calculation, in order to evaluate if the positive charge of **2** is delocalized on the aromatic ring, are currently under investigation.

4.3 Conclusion

Heck coupling between 1-bromo-pyrene and 4-vinylpyridine afforded **1** in high yield. A preliminary investigation of its optical and NLO properties at different concentration revealed a quenching in the emission and in the second order NLO response at high concentrations (10^{-3} M), probably due to the formation of centrosymmetric aggregates. Nevertheless the μβ value of **1** at 10^{-4} M ($2200*10^{-48}$ esu) is very high in view to its low push-pull character and when compared to similar molecular structures[10].

Moreover an easy and reversible interconversion between **1** and its protonated derivative **2**, has been performed by simple exposition to HCl or NH_3 vapours, either in solution or in the solid state. Such interconversion is accompanied by macroscopic variations in the optical properties of the system, suggesting a potential use of these materials as optical switch and pH sensors.

4.4 Experimental section

4.4.1 General methods

All reagents and solvents were purchased from Sigma Aldrich and used as received or purified by standard procedures. NMR spectra were recorded at room temperature on a Bruker Avance DRX 400 MHz. The chemical shifts δ are expressed in ppm relative to tetramethylsilane as internal standard. The multiplicity of the ^{1}H spectra is expressed as follows:

s = singlet; d = doublet; dd = doublet of doublet; t = triplet; m = multiplet.

When possible mass spectra (VG Autospec M256) and elemental analysis (Perkin-Elmer CHN 2400) have also been performed.

4.4.2 Synthesis of 4-(2-Pyren-1-yl-vinyl)-pyridine (1):

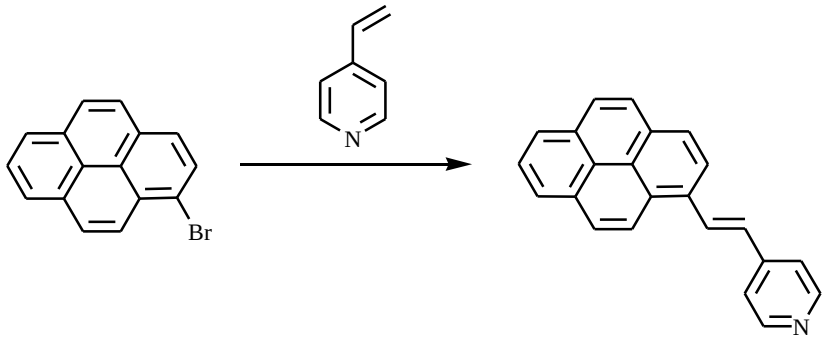

1-bromopyrene (1 g, 3.5 mmol), 4-vinylpiridine (0.68 ml, 3.5 mmol) and bis(tri-*t*-butylphosphine)-palladium(0) [Pd[P(*t*Bu)$_3$]$_2$] were weighted into a 100-ml Schlenk flask, under nitrogen atmosphere. Anhydrous toluene (60 ml) and degassed dicyclohexylmethylamine (Cy_2NCH_3) (0.904 ml, 4.4 mmol) were added, followed by 3 freeze-pump-traw cycles. The reaction was stirred for 24h at 80°C. Once completed, the reactive mixture was filtered on celite and the solution concentrated on vacuum. The solid was purified by column chromatography (CH_2Cl_2:Hexane, 7:3) followed by crystallization from pentane/methanol to give a yellow solid (700 mg, 65% yield).

^{1}H NMR (400 MHz, $CDCl_3$): δ (ppm) 7.24 (d, 1H, CH=CH), 7.52 (d, 2H, aromatic pyridine), 8.10 (m, 3H, aromatic pyrene), 8.19 (m, 4H, aromatic pyrene), 8.29 (d, 1H, aromatic pyrene), 8.33 (d, 1H, CH=CH), 8.45 (d, 1H, aromatic pyrene), 8.66 (d, 1H, aromatic pyridine).

^{13}C NMR (100 MHz, $CDCl_3$): δ (ppm) 121.41, 123.42, 124.22, 125.53, 125.83, 126.10, 126.56, 127.79, 128.31, 128.51, 129.25, 130.79, 150.50.

Elemental analysis $C_{23}H_{15}N$: found % C 90,40; % H 5,10; % N 4,75; calculated % C 90,40; % H 4.95; % N 4,59.

^{1}H NMR (400 MHz, $CDCl_3$):

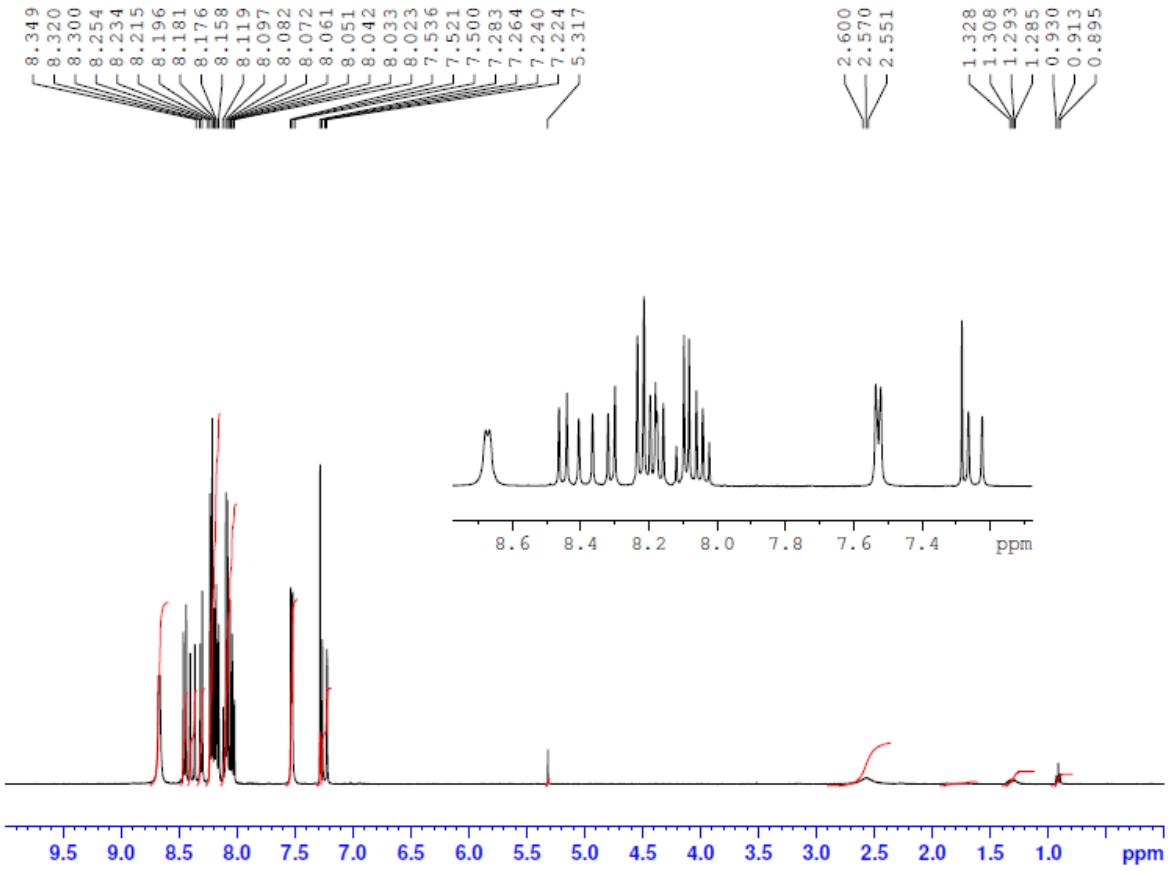

^{13}C NMR (100 MHz, $CDCl_3$):

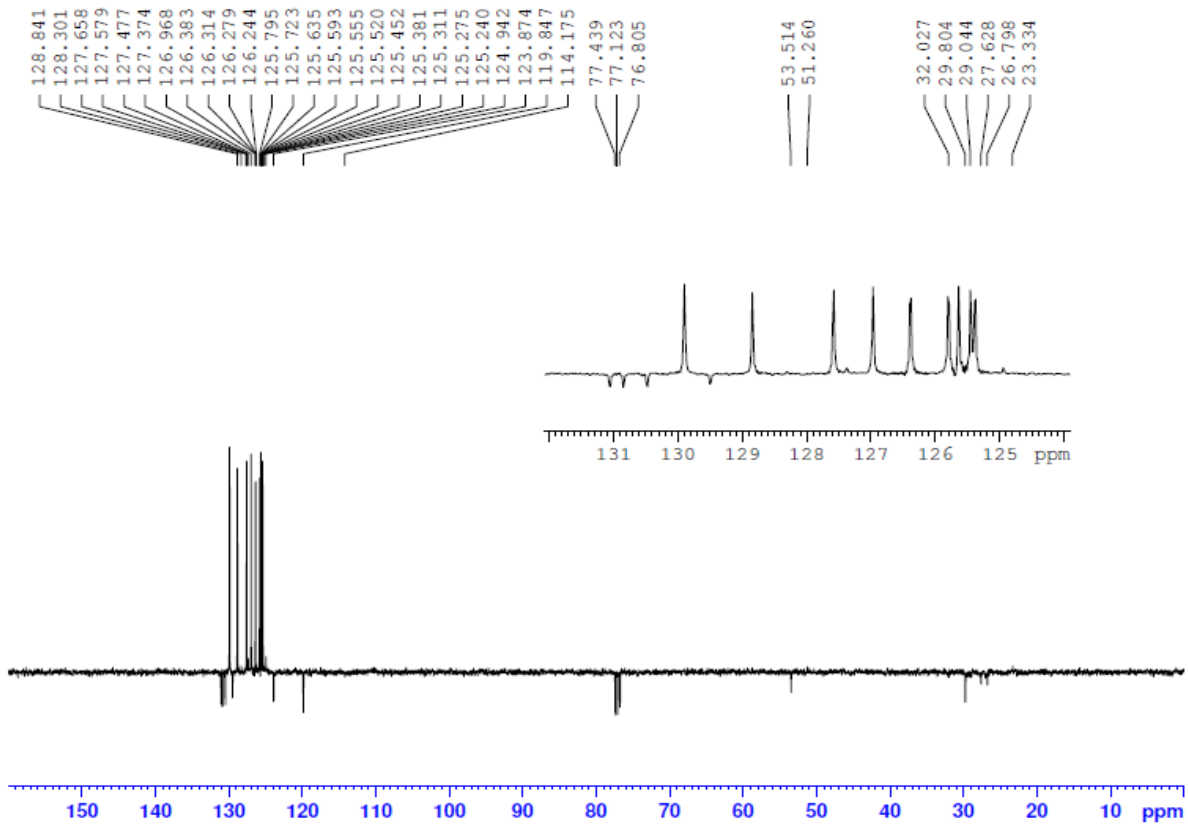

^{1}H-^{13}C HSQC (400 MHz, $CDCl_3$):

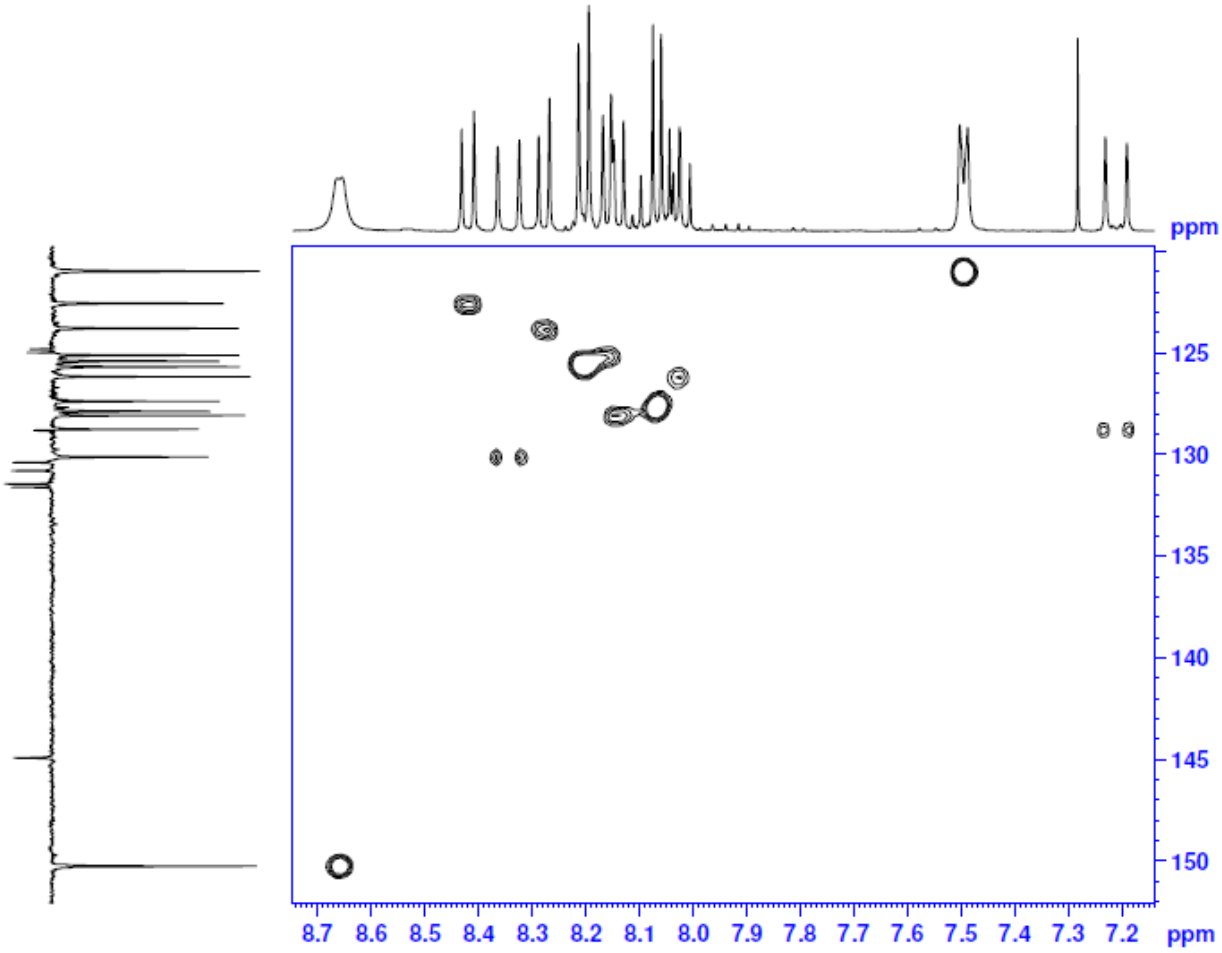

4.5 References

[1] a) Agullo-Lopez F., Cabrera J. M., Agullo-Rueda F., Electrooptics: Phenomena, Materials and Applications; Academic Press: New York, **1994**. b) L. R. Dalton, et.al., *Chem. Mater*., **1995**, *7*, 1060.

[2] Prasad P. N., Williams D. J., Introduction to Nonlinear Optical Effects in Molecules and Polymers, Wiley: New York, **1991**

[3] Balzani V., Campagna S. (Eds.), "Photochemistry and Photophysics of Coordination Compounds" Parts I & II, Topics in Current Chemistry, Volumes 280 *and* 281, Springer, Berlin, Heidelberg, Germany, **2007**.

[4] (a) Dalton L. R., Sullivan P. A., Bale D. H., *Chem. Rev*. **2010**, *110*, 25; (b) Sullivan P. A., Dalton L. R., *Acc. Chem. Res*. **2010**, *43*, 10.

[5] a) Azumi T., McGlynm S. P., *J. Chem. Phys*. **1964**, *41*, 3131. b) Clar E., Schmidt W., *Tetrahedron.* **1976**, *32*, 2563.

[6] a) Park S. M., Kim M.H., Choe J-I., Tai K., Chang S-K., *J .Org. Chem*. **2007**, 72, 3550. b) Xiang J., Zhu D., *Org. Lett*. **2008,** 10, 2271. c) Choi J. K., Kim S. H., Yoon J., Lee K-H., Bartsch R. A., Kim J. S., *J.Org.Chem*. **2006**, 71, 8011.

[7] Hariharan M., Karunakaran S. C., Ramaiah D., *Org. Lett.* **2007**, *9*, 417.

[8] Birks, J.B.; Dyson, D.J.; Munro, I.H. *Proc. Roy. Soc*. **1963**, *275*, 135.

[9] Singh Y., Gulyani A., Bhattacharya S., *FEBS Letters*, **2003**, *541*, 132.

[10] Calabrese V., Silvio Quici S., Rossi E., Cariati E., Dragonetti C., Roberto D., Tordin E., De Angelis F. and Fantacci S. *Chem. Commun.*, **2010**.

5 Synthesis of new inorganic/organic hybrids with enhanced linear optical properties

The continuously growing interest around materials endowed with emitting and non linear optical properties (NLO) is justified by their numerous electronic and photonic applications in the field of material science, such as, for instance, modulation of optical signals, microfabrication, sensing and medical imaging.[1-2]

For applications in optical devices, materials have to possess not only significant molecular response, but also attributes like chemical, photochemical and thermal resistance, must be easy to produce and process and with long term optical stability. In this field, a particular interest has devoted towards inorganic-organic hybrid systems, which offer the possibility to combine the properties of the organic component with those of the inorganic scaffold thanks to synergistic effect between the two systems with the aim to optimize the performance of the material.

In this thesis, we chose as organic component for the preparation of emitting hybrids the perylene chromophore. Perylene dyes are a class of materials with exceptional properties: high chemical and photochemical stability, molar absorptivity and fluorescence quantum yield. In this chapter we describe the synthesis of perylene bisimides asymmetrically substituted and displaying, at one side, a long secondary alkyl chain (to increase solubility) and, at the other, a ligand able to bind a Polyhedral Oligomeric Silsesquioxane (POSS). In fact, it has been recently reported that the introduction of such scaffolds in conducting polymers in electroluminescent devices[3] or bounding them in emitter OLED materials[4] increases in the thermal stability and in general the performances of the devices.

Moreover, the introduction of silsesquioxane fragments should reduce the aggregation-caused quenching (ACQ) phenomenon, which very often hampers the development of efficient solid state emitters. In fact organic chromophores with good emissive properties in solution become instead weak emitters when deposited in films or when in the crystalline state.

5.1 Organic Cromophore: Perylene

The chemistry of the perylene bisimides started with the work of Kardos in 1913. He described the reaction of naphthalene-1,8-dicarboximide in molten alkali to perylene bisimides. These products found their use as vat dyes and various derivatives are still produced today for red dyes and pigments[56]. Perylene bisimides combine a strong absorption in the visible region with fluorescence quantum yields near unity and a high stability towards photooxidation[7]. Furthermore, perylene bisimides feature a relatively low reduction potential, which enables their use as an *n*-type semiconductor and as an electron acceptor in photoinduced charge transfer reactions. Because of their appealing properties, perylene monoimide and perylene bisimide derivatives have been utilized in various electronic and optical applications such as field-effect transistors, fluorescent solar collectors, electrophotographic[8] devices, dye lasers[9], photovoltaic cells[10], and light-emitting diodes (LEDs)[11].

Since the pioneering work of Wasielewski *et al.* in 1992, the research on perylene imides took a new and exciting direction. Perylene bisimides were covalently connected to organic chromophores to create multifunctional photo- and electro-active systems. Photoexcitation of these compounds results in intramolecular energy or charge transfer with the perylene imide as the electron-accepting moiety. Potential application of these molecules in molecular and supramolecular electronics, photocatalysis and materials for LEDs and solar cells has resulted in a high activity in this field in recent years.

Compound	$\mathbf{E_{ox}}$	$\mathbf{E_{red}}$	$\boldsymbol{\lambda_{abs}}$	$\boldsymbol{\lambda_{PL}}$	$\boldsymbol{\phi_{PL}}$	$\boldsymbol{\tau}$
	(V)	(V)	(nm)	(nm)		(ns)
Perylene	1,04	-1,73	440	446	0,89	4,6
Perylene Mono-imide R_1=2,5-di-*tert*butylphenyl	1,05[a]	-1,24	505	528	0,99	4,8
Perilene Bis-imide R_1=2,5-di-*tert*butylphenyl	1,36[a]	-0,81[a]	528	530	0,97	3,6
Perilene Bis-imide R_1= 1-hexylheptyl	1,61	-0,59	524	534	0,99	4,0

Table 5.1: Optical and electrochemical property (in Toluene) of Perylene and Perylene bis-immide

5.1.1 Synthesis of perylene bisimides

The most common procedure used to synthesize the symmetrical perylene bis-imides **(2)** is the condensation reaction of the perylene dianhydride **(1)** with a primary ammine (Fig. 5.1)[12,13]. The choice of solvent for this reaction depends on the reactivity of the amine. For reactive amines, *e.g.* alkyl amines, water or DMF[14] can be used at 100 – 160°C. Solvents as quinoline or fused imidazole are necessary for less reactive amines such as aromatic amines with reaction temperatures of 160 – 180 °C. Zinc salts like zinc acetate are catalysts for the reaction; it has been suggested that they have an ability to solubilize the anhydride.

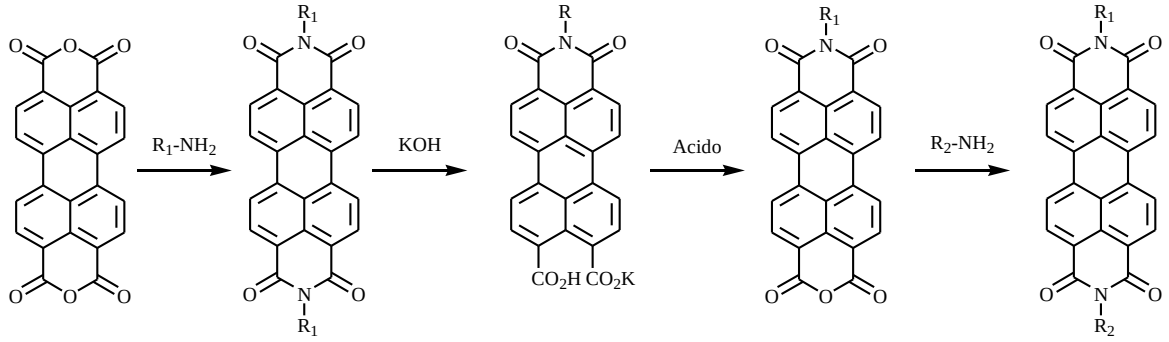

Figure 5.1: Synthesis of symmetrical and non-symmetrical perylene bisimides.

Formation of non-symmetrically substituted perylene bisimides **(5)** by performing the reaction with two different amines usually does not take place because of differences in reactivity of the two amines. Although it is possible to partially condensate the dianhydride **(1)** with a primary amine to form **4**, this method is not widely applied[15]. asymmetrically substituted perylene bisimides **(5)** are generally obtained in a multistep procedure (Figure 5.1)[16]. First, symmetrically substituted perylene bisimides **(2)** are partially saponificated into the potassium salt **(3)** by reaction with KOH in *tert*-butanol, and subsequent treatment with acid. The obtained monoimide monoanhydride **(4)** can be reacted with an amine to form the non-symmetrically substituted bisimide **(5)**.

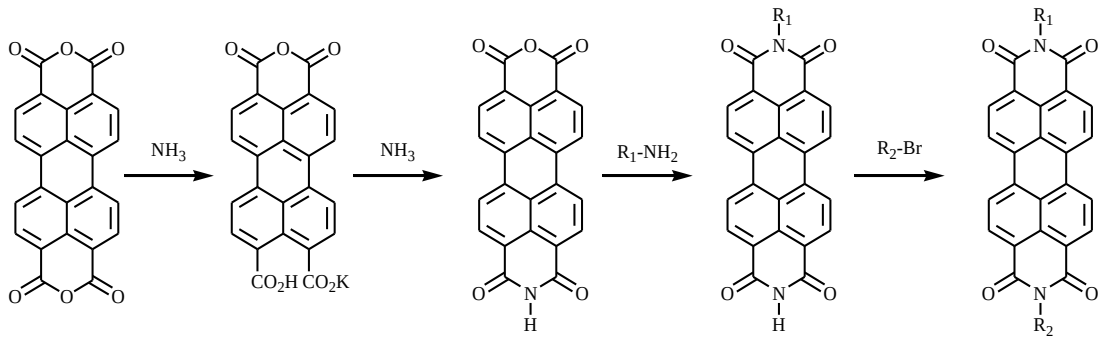

Figure 5.2: Alternative route to non-symmetrically substituted perylene bisimides.

An alternative route to non-symmetrically substituted perylene bisimides that does not require perylene bisimide as a starting material, is shown in Figure 5.2[16]. The monopotassium salt **(6)** of dianhydride **1** reacts in a condensation reaction with ammonia to imide **(7)**[17]. After reaction with a primary amine to **8**, a nucleophilic substitution reaction with an alkylbromide in presence of a base leads to bismide **5**, where R_2 = alkyl. (Figure 5.2).

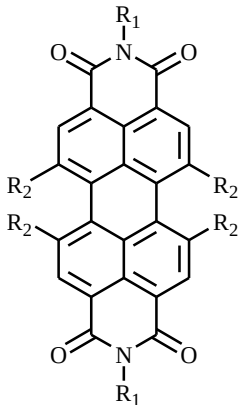

Figure 5.3: Commonest substitution positions for the perylene

The solubility of the perylene bisimide strongly depends on the substitution (Figure 5.3). It is found that high solubility in organic solvents is obtained when the two *N*-terminal groups R_1 are secondary alkyl residues having two long chains or *ortho*-substituted phenyl groups[18]. These substituents are forced out of the plane of the chromophore and thereby hamper the face-to-face π-π stacking of the perylene bisimides, which has a positive effect on the solubility of the molecules. Another possibility to increase the solubility of the perylene bisimide is by substitution at bay-positions R_2. In this case, we proceed with a halogenation, introducing Cl or Br groups, which are then replaced, for example, with phenoxy group by reaction with phenol in presence of a base. Because of their bulkiness, the substituents in the bay-region force the aromatic core to bend with an increase in solubility. Nevertheless, the

bromination or chlorination reactions in bay position generate isomer mixtures which are often difficult to purify and separate. For this reason, in this thesis we preferred to use the route described in Figure 5.1 and to perform the synthesis of asymmetric perylene bisimide.

5.2 Inorganic scaffolds: Silsesquioxanes

The term "silsesquioxane" refers to a very large family of silicon-oxygen compounds with the idealized empirical formula $(RSiO_{1.5})_n$, where R is hydrogen or any alkyl, alkylene, aryl, arylene, or derivatives of these groups.[19] Silsesquioxanes have been synthesized with structures that are either polymeric or oligomeric (i.e. existing as discrete polyhedral structures) and generally exhibit different properties, hence their research and applications are usually separated.[20]

The sub class of interest in this dissertation are the organo-spherosilicates characterized by interconnected siloxane rings known as Polyhedral Oligomeric Silsesquioxanes, (POSS) characterized by a self-organized cage-like structure. The cubic skeleton of the cage is constituted of Si atoms bearing an organic group occupying the vertex position and oxygen atoms bridging the corners.

POSS can be further divided into two subgroups: completely condensed and incompletely condensed. For completely condensed species [Figure 5.4 (a-c)], oxygen acts only as a bridge between silicon atoms and there are no –OH functionalities. Fully condensed silsesquioxanes (notably polyhedral oligomeric silsesquioxanes), because of their inherent thermal and oxidative stabilities, hardness, relative ease of preparation, wide array of possible frameworks, and variety of pendant groups, have attracted much attention in recent years to model catalytic surfaces,[21,22] generate new catalysts,[23] novel porous media,[24] NMR standards,[25] and act as novel encapsulants.[26]

Incompletely condensed silsesquioxanes contain silanol groups [Figure 5.4d] which make them ideal compounds for modeling the surfaces of silica[3,27] and as ligands for metal coordinate complexes.[28]

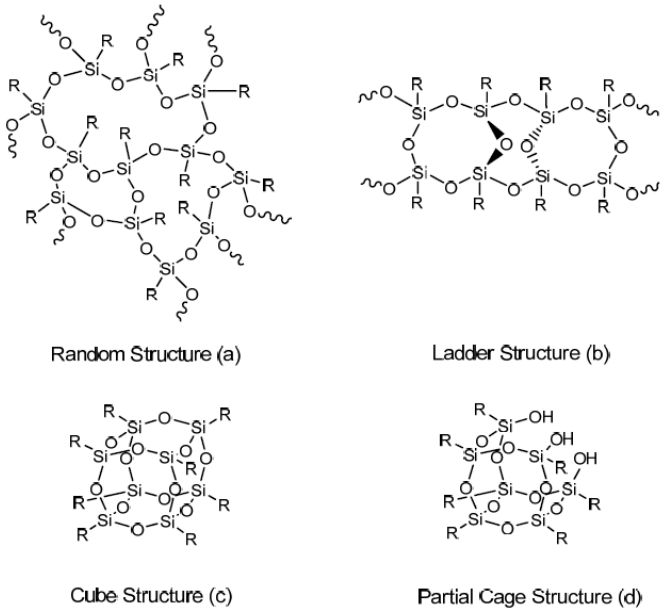

Figure 5.4. Some representative silsesquioxane structures

When the polyhedron is not fully condensed (i.e. when it differs from $R_8Si_8O_{12}$) the dangling oxygen atoms[29] complete their coordination with a terminal hydrogen, thus yielding di, tris, or tetra silanols ($R_8Si_8O_{10}(OH)_2$, $R_7Si_7O_9(OH)_3$, $R_6Si_6O_7(OH)_4$).[4] These POSS silsesquioxanes are soluble in most organic solvents due to the sheath of R groups surrounding this tiny "silicate" cage (R typically = c-C_5H_9 or c-C_6H_{11}).

5.2.1 Definitions, Structures, and Nomenclature

Structurally, silsesquioxanes consists of sp^3 hybridized Si atoms bound to three oxygen atoms and one R group, where R is typically an organic moiety as mentioned above. When n = 4, 6, 8, 10, or 12, the resulting compounds are called polyhedral oligomeric silsesquioxanes and possess three dimensional, symmetrical structures. In the specific instance where n = 8, the silsesquioxane octamers are referred to as cubic silsesquioxanes or simply "cubes." Alternatively they are called "POSS". Cubes have been the focus of many studies due to their nanometer size, high degree of symmetry, and numerous preparative routes to useful quantities as discussed further in this chapter.[30]

In these studies, our composite precursor is built upon cube as well n = 8 analogs (Figure 5.6). In its structure, an inorganic Si_8O_{12} core is surrounded by eight organic hydrocarbon groups; the inorganic core gives them high thermal stability, while the eight organic groups yield good solubility in common organic solvents and good compatibility or miscibility with organic matrices

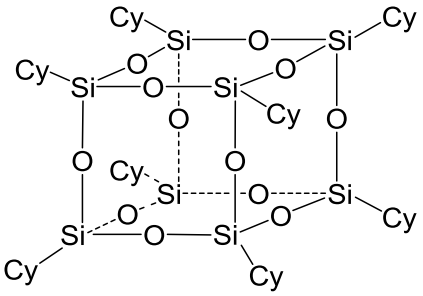

T_8

Figure 5.6: Idealized T_8 silsesquioxane structures (Cy = *c*-C_6H_{11}).

5.2.2 Synthesis of Silsesquioxane Silanols

No industrial methods for the synthesis of oligosilsesquioxanes have so far been described in the literature. However, a great number of reactions leading to the formation of polyhedral silsesquioxane are known. Depending on the nature of the starting materials, all these reactions may be divided into two large groups. The first group includes the reactions giving rise to new Si-O-Si bonds with subsequent formation of the polyhedral framework. The second group of reactions covers the processes involving only variations in the structure and composition of substituents at the silicon atom without affecting the silicon-oxygen skeleton of the molecule. As the interest in POSS derivatives has increased, efforts to synthesize POSS with a variety of both reactive and inert substituents have increased. The polyhedral silicon-oxygen skeleton can be formed by the hydrolytic condensation of trifunctional monomers $XSiY_3$, the condensation of Si-functional oligoorganylcyclosiloxanes $[XYSiO]_m$, the co-condensation of organosilicon monomers and/or oligomers of different structure and composition, and the thermolysis of polyorganylsilsesquioxanes[31]. In some cases, the above reactions can be combined in order to obtain certain oligosilsesquioxanes or to increase the yield. Among the above synthesis methods, the hydrolytic condensation of $XSiY_3$ is the most universal and traditional synthetic route to oligolsilsesquioxanes and their homo derivatives. Most polyhedral compounds of this type known at present have been synthesized by this method, the corresponding organyltrichlorosilanes, less often organyltrialkoxysilanes, as well as trichlorosilane and trimethoxysilane being used as the starting monomers.

$$n\mathrm{XSiY_3} + 1.5n\mathrm{H_2O} \rightarrow (\mathrm{XSiO_{1.5}})_n + 3n\mathrm{HY}$$

(*X* =a chemically stable substituent, such as methyl, phenyl, or vinyl)

(*Y* = a highly reactive substituent, such as Cl, OH or OR)

The hydrolytic condensation of $XSiY_3$ is a complex and time-consuming multistep processes leading to polymers and oligomers which may include oligosilsesquioxanes and their homo derivatives. The reaction rate, the degree of oligomerization and the yield of the polyhedral compounds formed, strongly depend on the concentration of initial monomer in the solution, nature of solvent, character of substituent X in the initial monomer, nature of functional group Y in the initial monomer, type of catalyst, temperature of the reaction and addition of water. The influence of all these factors, both individual and together, has been studied only in general, without any quantitative estimation of their effect on the reaction course. This may be explained by the complicated character of the polycondensation process and the strong mutual effect of the above factors. Cyclohexylsilsesquioxane is most interesting compound for its homo derivative cyclohexyl-trisilanol is the precursor for many functional silsesquioxane monomers.[32] They were both synthesized by the hydrolytic condensation of cyclohexyltrichlorosilane in aqueous acetone and with acid or base as catalyst over a period of several weeks.

5.2.3 Mechanism of Formation of Silsesquioxane Cages and Networks

The preparation of silsesquioxane materials, usually prepared from the acid or base-catalyzed hydrolytic condensation of trifunctional organosilanes, is a multi-step and rather complicated process. The synthesis is very sensitive to a combination of experimental factors (as mentioned previously) due to a statistical distribution of intermediate components and usually produces a wide range of products, from small oligomers and polyhedral silsesquioxanes to mixtures of polymeric resins and gels. Sol-gel networks, polysilsesquioxanes, and polyhedral silsesquioxanes all form by the same general reaction mechanisms (Figure 5.4).

Since a suitable kinetic equation has yet to be determined for the synthesis of silsesquioxanes, no *universal* synthetic protocols have been established.[2] However, control of reaction conditions can be made to favor the formation of one structure (or mixture of structures) preferentially for certain silane monomers. Many procedures for the formation of *specific* silsesquioxanes have been developed recently and account for the increasing number of papers and patents published yearly on silsesquioxanes.

While no universal preparative procedures have been established for the formation of silsesquioxanes, it is generally found that: (1) lower concentrations of silane monomers favor intermolecular condensation and thus polyhedral structures are favored while higher concentrations of monomers favor polymeric structures; (2) low pH favors cyclization

whereas higher pH favors polymerization; (3) water is essential to cyclization but excess water favors polymerization.[2] While the rates of hydrolysis and condensation (as affected by the above factors) determine the final shape of the compound, the general hydrolysis mechanism is similar in any case. The general hydrolytic reaction mechanisms for trialkoxysilanes are shown below in Figure 5.7.

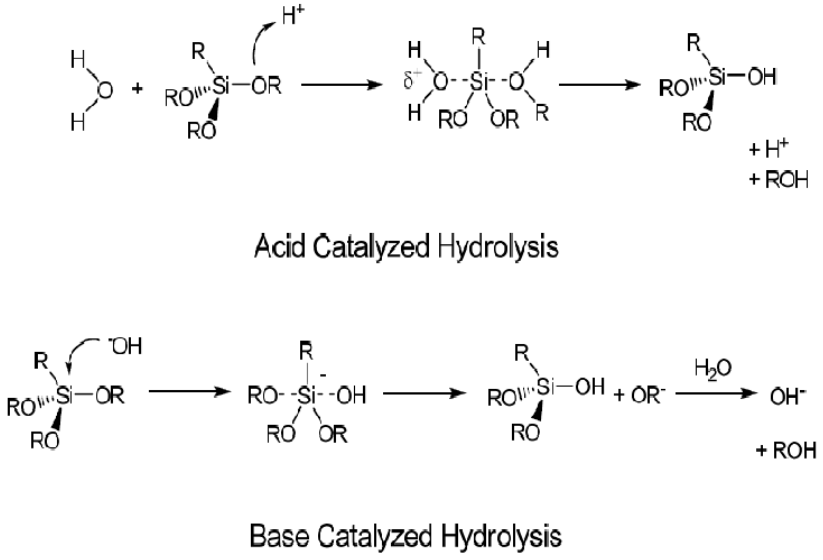

Figure 5.7. Acid and base-catalyzed hydrolysis mechanisms of trialkoxysilane.

Under acidic conditions, an alkoxide group is protonated in a rapid first step. Electron density is withdrawn from the silicon atom, making it more electrophilic and thus more susceptible to attack from water. The rate of the first hydrolysis is the fastest because the penta-coordinate (SN_2) transition state (which is stabilized by electron-donating alkoxy groups)[33] is at a maximum, while each ensuing hydrolysis occurs more slowly as alkoxy groups are displaced as alcohol. Similarly, condensation occurs most rapidly for singly-hydrolyzed species.

Under basic conditions, the alkoxide oxygens tend to repel the –OH nucelophile.

However, once initial hydrolysis has occurred, each subsequent alkoxide group becomes more easily removed from the monomer than the previous one as the negatively-charged transition state is made relatively more stable by hydroxyl groups, which have lower electron density than alkoxy groups.[20] Therefore, highly hydrolyzed species are more prone to attack and condensation occurs most rapidly for fully-hydrolyzed species.

5.3 Inorganic/organic POSS hybrids for optoelectronics

Numerous examples of the application of POSS molecules or materials have been published in the fields of optics and electronics. For example, a series of polyaromatic substituted POSS, **9**-**12**, were prepared from $T_8(CH=CH_2)_8$ through Heck coupling. They were shown both to be photoluminescent and to have charge transport abilities.[34,35] Another photoluminescent POSS compound, having a carbazole-based substituent, has been prepared from $T_8(OSiMe_2H)_8$. It has been shown that the presence of the POSS core did not affect the electronic properties inherent to the carbazole species.[36,37,38] The photoluminescence of products has additionally been used to analyze the purity of potentially photoluminescent POSS compounds, such as $T_8[CH=CHC_6H_4\text{-}4\text{-}C_6H_3\text{-}3,5\text{-}(CO_2Me)_2]_8$ and $T_8[CH=CHC_6H_4\text{-}4\text{-}C_6H_3\text{-}3,4\text{-}(OMe)_2]_8$.[39]

A POSS species has been used in the preparation of a material reported to show quantum dot-like properties, but this has not yet been followed up by more comprehensive studies.[40,41] Two derivatives with multiaryl functional groups, **13** and **14** (Figure 5.8), were seen to behave in the same manner in the solid state as inorganic quantum dot materials, including showing the necessary quantum confinement effect. The cubic T_8 core of the materials appears to isolate the organic arms of the molecule sufficiently from each other to attain quantum confinement. The POSS compound $T_8(CH_2SiMe_2C_6H_4\text{-}4\text{-}NPh_2)_8$ is one example of a series prepared for use in organic light-emitting diodes (OLEDs), the preparation of which has been patented.[42] The POSS materials are included in the devices in a carrier transport layer intercalated between the two electrodes and the light-emitting layer of the system. In these devices, the POSS component controlled the transport of electrons and holes. Improvements in brightness and efficiency were claimed over devices made without the POSS species. A compound with somewhat similar functional groups, **15** (Figure 5.8), has been prepared by Heck coupling for use as an electroluminescent film precursor for OLED applications.[43] The material showed a significant improvement over the parent molecular counterparts in these applications. The POSS-pyrene derivatives **12** (Figure 5.8) have also been tried for application in OLED technology as the light-emitting portion of an OLED device.[44] The POSS species in this application were able to be applied by spin-coating onto glass substrates, potentially offering an advantage over other systems, which require vacuum deposition or have possible problems with purity. Initial results suggested that these materials showed promise, although synthetic modification would likely be required. Other POSS with chromophore substituents have also been prepared and showed good film-forming and

luminescence properties.[45,46] They have been used as emitting material in double-layer OLEDS[57] or deposited on quartz or indium tin oxide plates for use as electroluminescent nanoparticles.[47] In addition, simpler POSS derivatives have been used in materials where they do not contribute directly to the electrical or luminescent properties, although their presence results in changes in behavior of the systems. For instance, $\{T_8[(CH_2)_3NH_3]_8\}Cl_8$ has been introduced into photoluminescent materials to pack between poly(electrolyte) multilayers and thereby stop the diffusion of the quantum dot materials into the film.[48] In an electrochemical system, thermolysis of $T_8(OSiMe_2H)_8$ in pyridine afforded a threedimensional network where the POSS units are linked through -$OSiMe_2O$- bridges.

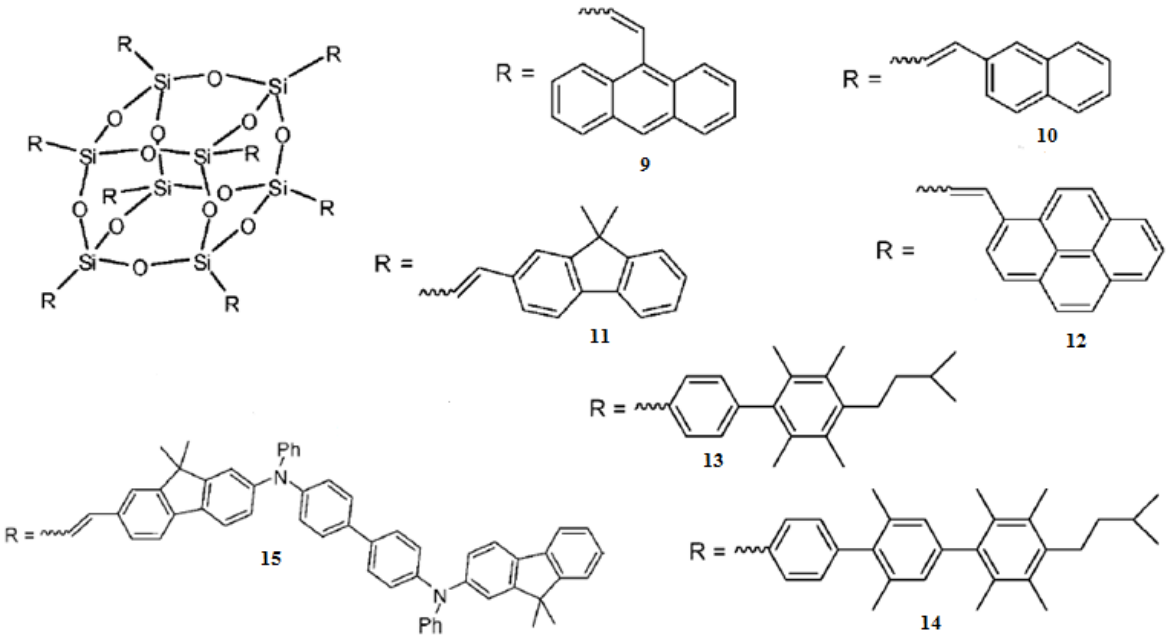

Figure 5.8: POSS compounds

Moreover, a POSS functionalised with a primary ammine unit has been recently used as a substituent to transform the perylene dihanydride in the corresponding bisimide.[49] Thanks to the introduction of the POSS this new perylene bisimide becomes very soluble in most organic solvent; this notwithstanding, probably for the low steric effect of isobutyl substituents, the molecules can form dimer by π-π interactions.

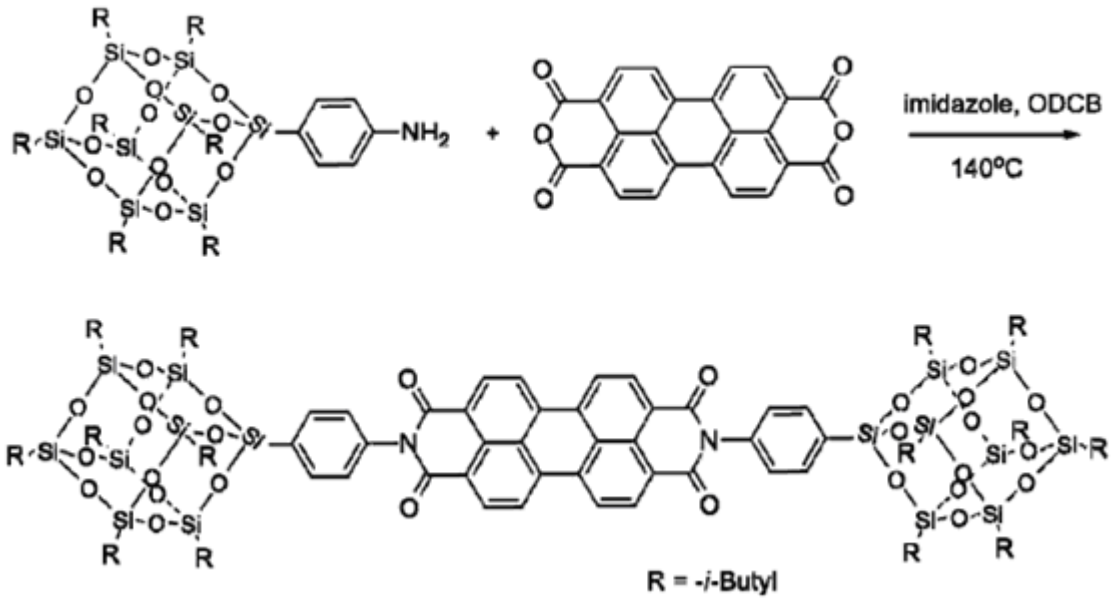

Figure 5.9: Synthesis of Hybrid organic-inorganic

5.4 Discussion of Results and Analysis

5.4.1 Synthesis of POSS

In this thesis two different typologies of POSS have been used: the first is the uncompletely condensed [(*c*-C_6H_{11})$_7$$Si_7O_9(OH)_3$] or $Cy_7T_7(OH)_3$. Even if it is commercially available we preferred to prepare it according to the basic hydrolysis methodology[50], developed by Feher and reported below:

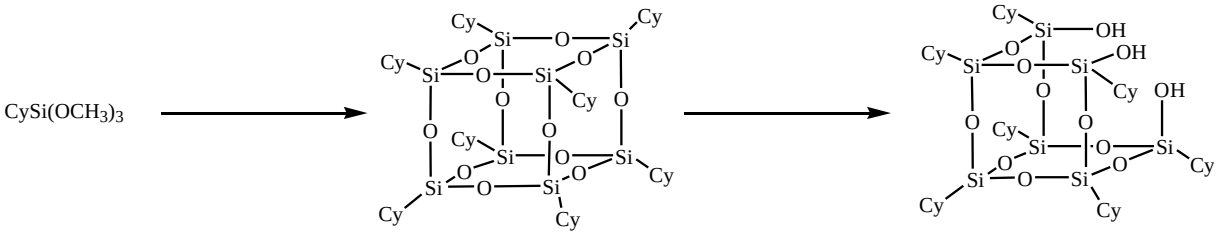

16 **17**

Cy=c-C_6H_{11}

While the second POSS used in this thesis is completely condensed [(*c*-C_6H_{11})$_7$$(CH=CH_2)Si_7O_{12}$] or Cy_7VyT_8.

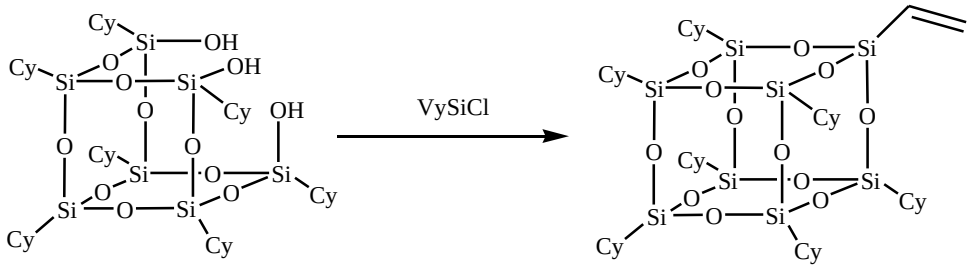

18

For the second product, we followed the published procedure describing the corner capping reaction of $VySiCl_3$ in the presence of triethylamine[51].

5.4.2 Synthesis of perylene bis-imides

The solubility of the perylene bis-imides varies significally depending to the N-terminal groups. It has been verified that the high solubility in organic solvents has been obtained when N-terminal groups are secondary alkyl residuals having two long chains (so called "swallow tails")[52]. In particular, 1-hexylheptyl chain has been selected for it offers the best compromise between synthetic accessibility and solubility increase. The first step thus involved the synthesis of the 1-hexylheptilamine, which was prepared following the scheme below with some modifications with the synthesis reported in the literature[53].

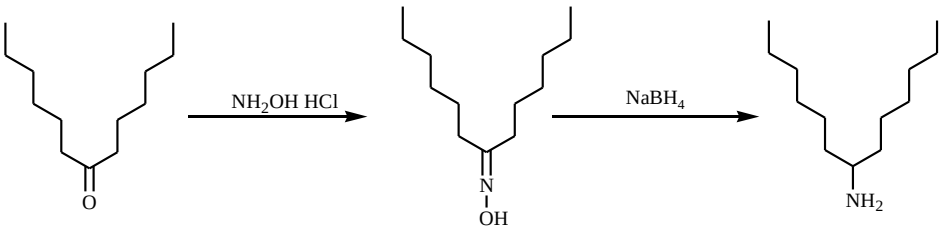

19 **20** **21**

The 7-tridecanone **19** is commercial and relatively inexpensive. The oxime **20** was synthesized through condensation of the corresponding ketone with the hydroxylamine hydrochloride. The further step is the reduction of oxime **20** with $NaBH_4$ to give tridecan-7-amine. Previous trials to perform the reduction with Na were less successful giving low yield. Then, the amine was used for the condensation reaction with perylene dianhydride **21** to give the perylene bis-imide **22**.

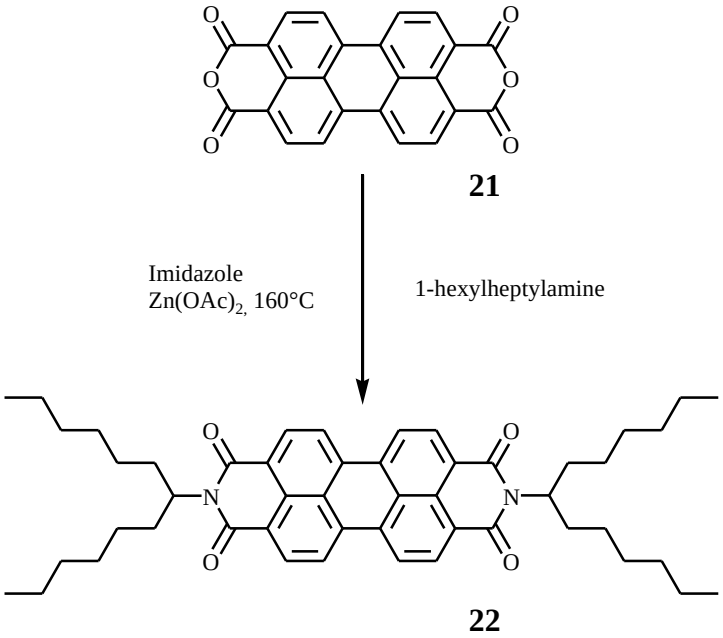

The reaction happens in molten imidazole at 160 °C and is catalysed by $Zn(OAc)_2$, the latter acting as Lewis' acid. The symmetric perylene bisimide, differently from its precursor dianhydride **21**, is soluble in almost all polar and non polar organic solvents. Moreover, this compound has a fluorescence quantum yield close to 100%, even in presence of O_2[54]. The next step involves the selective hydrolisis of one of the two imides through saponification of the compound **22** resulting in potassium salts **23** through the reaction with t-butanol and KOH and subsequent treatment with hydrochloridric acid. The time of hydrolysis is very important to obtain **24** with good yield as an excessive reaction time leads to the production of a high percentage of the starting dianhydride, while low reaction times leave a lot of unreacted starting material.

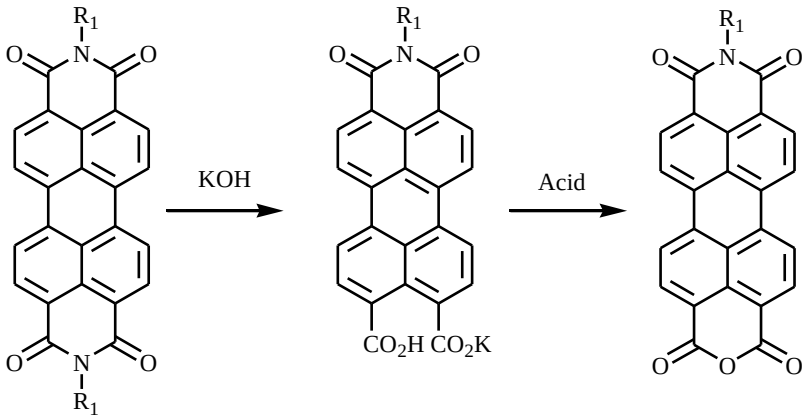

22 **23** **24**

$R_1 = (CH_3(CH_2)_4CH_2)_2CH-$

The product was purified through washings with ethanol and pentane and was crystallized in methylene chloride and hexane. The characterization of the compounds **22** and **24** was performed by ^{1}H NMR, ^{13}C NMR, elementary analysis and mass spectroscopy. A first purity check is performed by ^{13}C NMR: compound **22** displays a characteristic peak at 54.78 ppm, while **24** shows a peak of 54.93 ppm for the R_2N-C*H-$(CH_2)_2$ group. It was found that working at 80 °C for 40 minutes leads to the hydrolysis of the bisimide with a 92% yield.

Once obtained, monoimide **24** was then reacted with different primary amines to give a family of asymmetric perylene bisimides **25** endowed with a good solubility, and bearing a functional group suitable for further reactions.

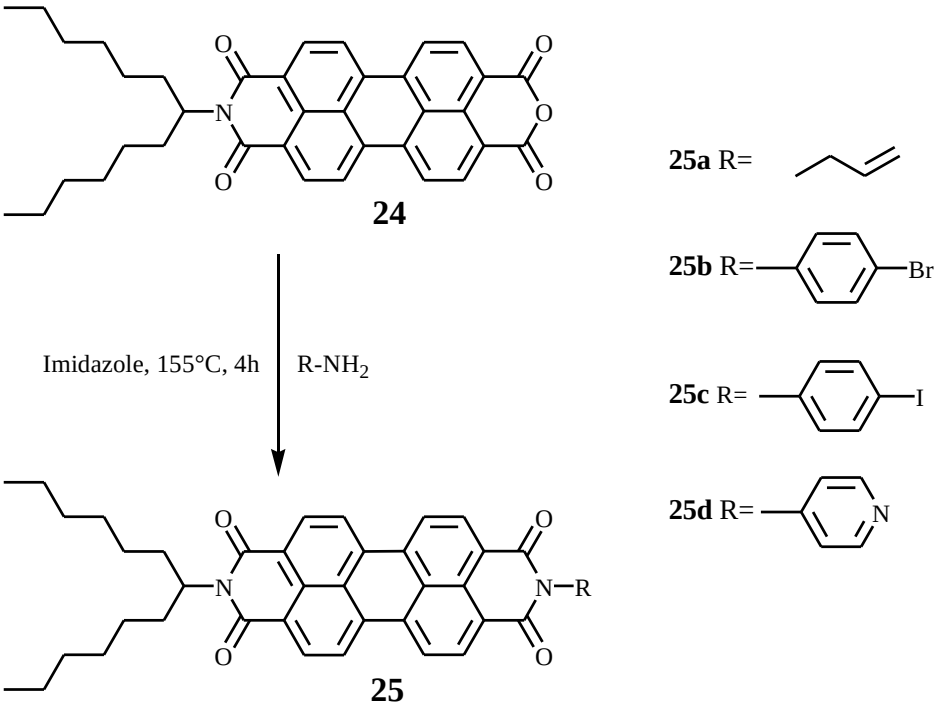

24

25

Compounds **25a**, **25b**, **25c** and **25d** were obtained by using the same procedure described for the synthesis of bisimide **22**, that is by reacting **24** with the desired primary amine in presence of imidazole and $Zn(OAc)_2$. The products obtained in such a way were purified through washings with ethanol and pentane and with successive crystallizations in methylene chloride and pentane, resulting in a red solid with high yield. The characterization of the compounds was performed through ^{1}H NMR, ^{13}C NMR, elementary analysis and mass spectroscopy (see experimental part).

5.4.3 Synthesis of Perylene-POSS hybrids

As a first approach for the synthesis of a perylene-POSS hybrid, we investigated the corner capping between incompletely condensed silsesquioxane **17** (prepared as described in 5.6.3) and a perylene derivative bearing the $Si(OMe)_3$ moiety. This latter has been prepared by silylation of the allyl group of **25a**, performed by $HSi(OMe)_3$ and Karstedt catalyst:

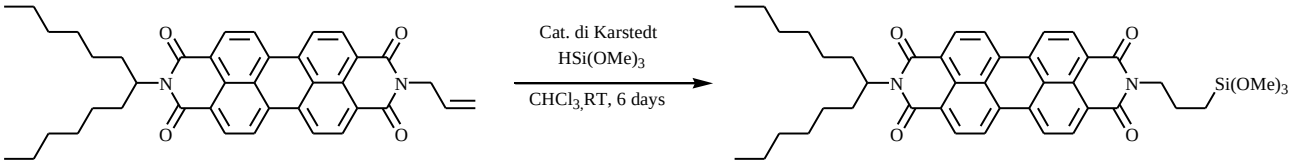

25a **26**

The reaction was followed via ^{1}H-NMR spectroscopy, observing the disappearance of the typical allylic signals of **25a** (δ=6.0 ppm) and the appearance of a peak at δ=3.6 ppm for the methoxy group of **26**. Once formed, product **26** was used directly without further purification, due to his sensitivity to moisture.

Corner capping reaction of **26** with silsesquioxane **17** was successfully performed in dry toluene and in the presence of para-toluensulfonic acid as a catalyst. Previous attempts of condensation in $CHCl_3$ or toluene at reflux gave negative results. Only in presence of acid it was possible to obtain the organic-inorganic hybrid **27** after 24h at 80°C:

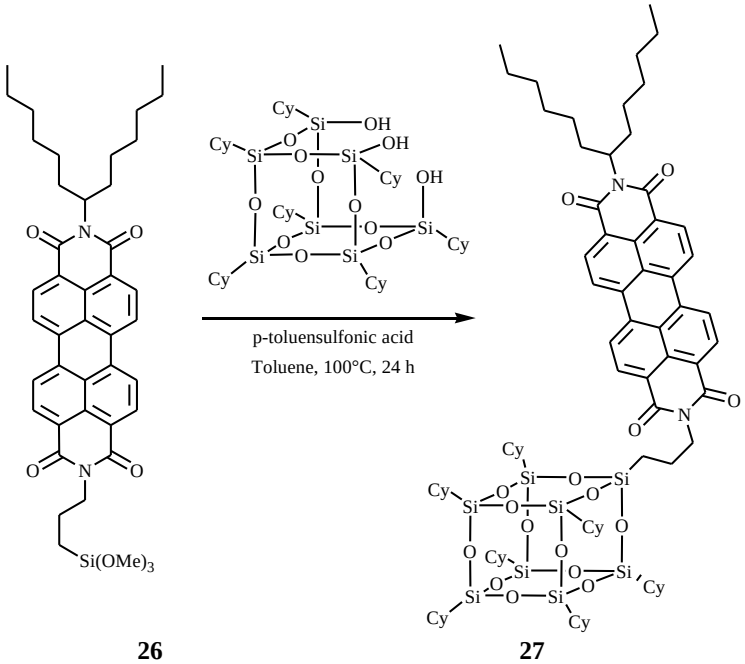

26 **27**

Compound **27** was purified through chromatography on silica (CH_2Cl_2/hexane) yielding a brilliant red coloured solid with a 23% yield. It has been characterized by NMR (^{1}H, ^{13}C, ^{29}Si)

spectroscopy, mass spectroscopy, elemental analysis (see experimental part) and also an optical characterization has been performed (quantic yield, absorbance and PL).

Absorption and emission spectra in $CHCl_3$ display the typical features of the monomeric perylene unit, with mirror images and three resolved peaks for the π-π transition. (Figure 5.10)

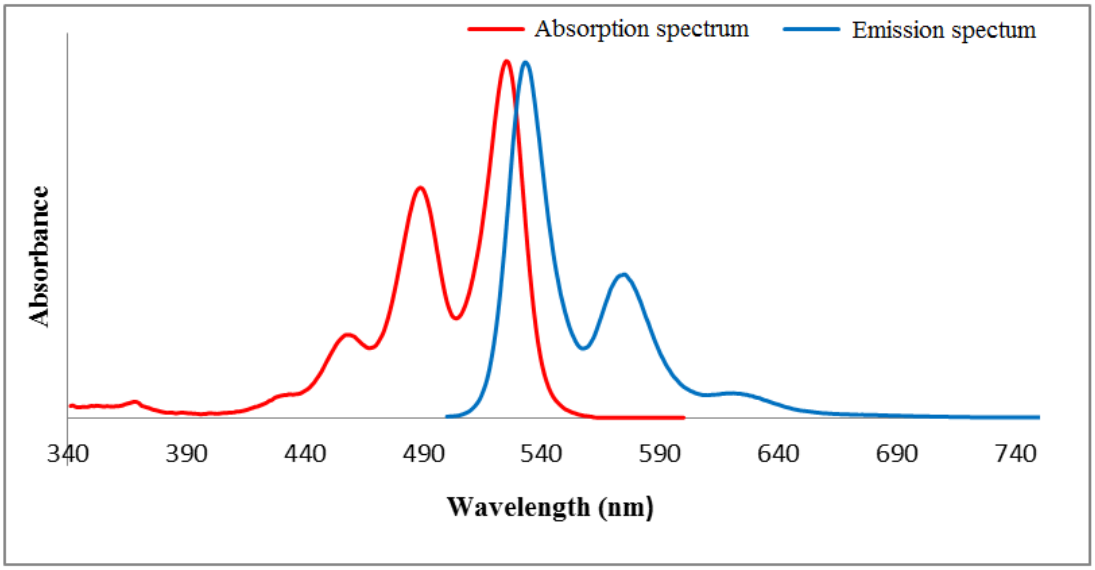

Figure 5.10: Absorption spectrum (*UV-VIS* in $CHCl_3$, in red) of compound **27** compared with the relative emission spectrum (fluorescence in $CHCl_3$, in blue)

The fluorescence quantum yield in $CHCl_3$ solution, using as standard the perylene bisimide **22** (100% quantic yield), was equal to 73%. The compound displays at the solid state an emission band centred at 650 nm (Figure 5.11). Measurements of the fluorescence quantum yield in the solid state and in solution are under investigation in order to establish whether the silsesquioxane fragment is able to inhibit the Aggregation Caused Quenching (ACQ) phenomenon, which is one of the major obstacles in the preparation of emitting devices starting from luminescent molecules.

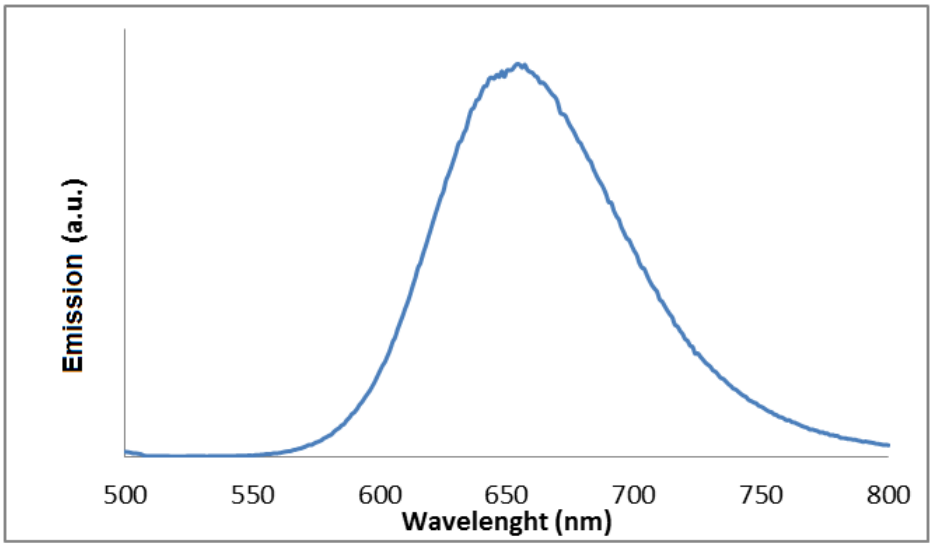

Figure 5.11: Emission spectrum of compound **27** in solid state

A second approach for the synthesis of an organic-inorganic hybrid was performed by investigating the Heck coupling reaction of perylene derivatives with the vinyl group of silsesquioxane **18** prepared as described in paragraph 5.6.4.

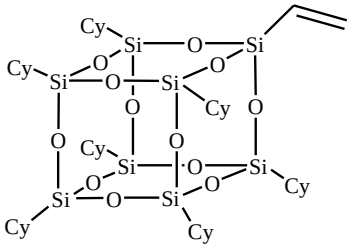

18

The first trials to react POSS **18** with the perylene bisimide containing the p-bromophenyl group were not successful. After a number of trials with different solvents, temperatures and reaction times we hypothesized that the main reason for the negative results could be a low reactivity of the bromine atom of the perylene bisimide. A simple shift to compound **25c**, which bears the p-iodophenyl group, was successful:

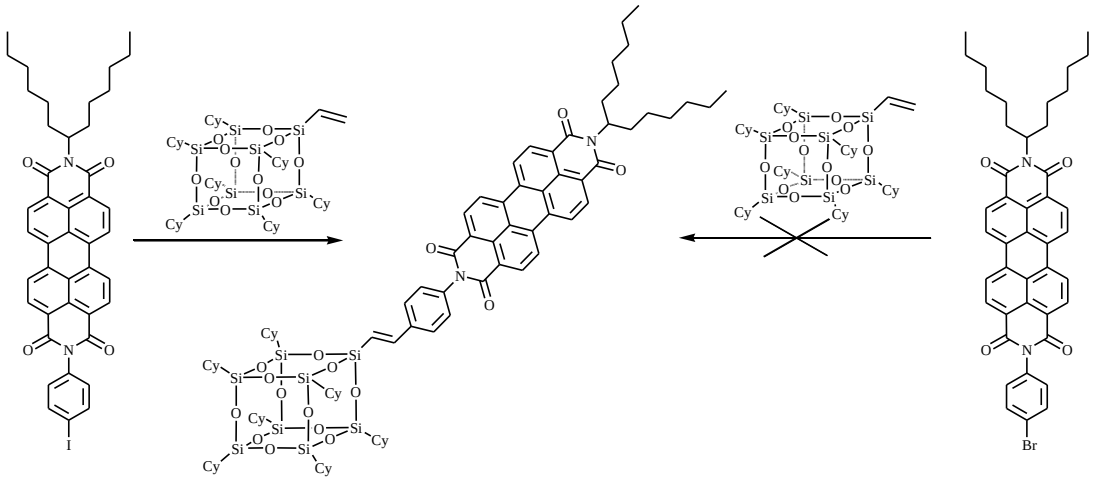

25c **28** **25b**

The reaction was performed in dry toluene in presence of diciclohexylmethylamine (which operates as Base/HI scavenger) and palladium(0): [Pd[P(*t*Bu)$_3$]$_2$] as catalyst. The formation of compound **28** was followed through ^{1}H NMR spectroscopy by observing the disappearance of the vinyl signals typical of **18** and the appearance of new signals relative to the trans double bond of **28**. So far the best yield that been obtained after a one week of reaction at 80 °C working with stoichiometric ratio perylene/POSS of 1:1; longer reactions times did improved in the reaction yield. After purification by chromatography, product **28** was obtained with a 37% yield. It has been fully characterized through NMR spectroscopy (^{1}H, ^{13}C, ^{29}Si), mass spectroscopy, elemental analysis (see experimental section) and also optical characterization has been performed (absorption, emission, PL and quantum yield). Also for this derivative, the absorption and emission spectra in $CHCl_3$ display the typical features of the monomeric perylene unit (Figure 5.10).

The fluorescence quantum yield in $CHCl_3$ using as standard the perylene bisimide **22** (100% quantum yield)[55] was equal to 90%. The compound displays at the solid state an emission band centred at 650 nm (Figure 5.11). Measurements of the fluorescence quantum yield in the solid state and in solution are under investigation in order to establish weather the silsesquioxane fragment is able to inhibit the Aggregation Caused Quenching (ACQ).

5.5 Conclusions

We synthetized a family of non-symmetrically substituted perylene bisimides that, excluding allyl derivative, was never synthesized. The compounds were all obtained with high yield and present good solubility in almost organic solvent. They have been reacted with two different typologies of POSS (completely and not completely condensed) and in both cases two organic-inorganic hybrids were prepared. A full spectroscopical characterization of the new compounds has been accomplished and their optical properties were studied. In particular, they presented very high quantum yields in solution and higher solubility, which allows a purification by column chromatography. Solid state quantum yield are currently under investigation in order to evaluate whether the introduction of POSS cages could have a positive effect in reducing the ACQ phenomenon.

5.6 Experimental section

5.6.1 General methods

All reagents and solvents were purchased from Sigma Aldrich and were used as received or purified using standard procedures. NMR spectra were recorded at room temperature on a Bruker Avance DRX 400 MHz. The chemical shifts δ are expressed in ppm relative to tetramethylsilane as internal standard. The multiplicity of the ^{1}H spectra is expressed as follows:

s = singlet; d = doublet; dd = doublet of doublet; t = triplet; m = multiplet.

When possible mass spectra (VG Autospec M256) and elemental analysis (Perkin-Elmer CHN 2400) have also been performed.

5.6.2 Synthesis of Octa(cyclohexylsilsesquioxane) (*c*-$C_6H_{11})_8Si_8O_{12}$ (16):

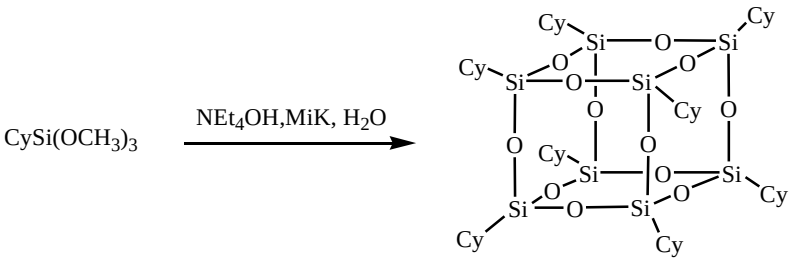

Cyclohexyltrimethoxylsilane (20 g, 97.88 mmol) was hydrolyzed with water (5.1 ml, 283 mmol) and Net_4OH (1.48 ml, 36 mmol) as catalyst, in methyl isobutyl-ketone (100 ml). The reaction solution was refluxed 2 days and then stirred at room temperature 3 days, with formation of white microcrystals. The reaction crude was filtered and washed several times with hot acetone to give (*c*-$C_6H_{11})_8Si_8O_{12}$ in 86 % yield.

^{1}H NMR (400 MHz, $CDCl_3$): (ppm) 0.78 (s, 8H, CH), 1.25 (s, 42H, CH_2CH), 1.76 (s, 42H, CH_2CH)

^{29}Si NMR (79.5 MHz, $CDCl_3$): (ppm) -68.69 ppm

^{1}H NMR (400 MHz, $CDCl_3$):

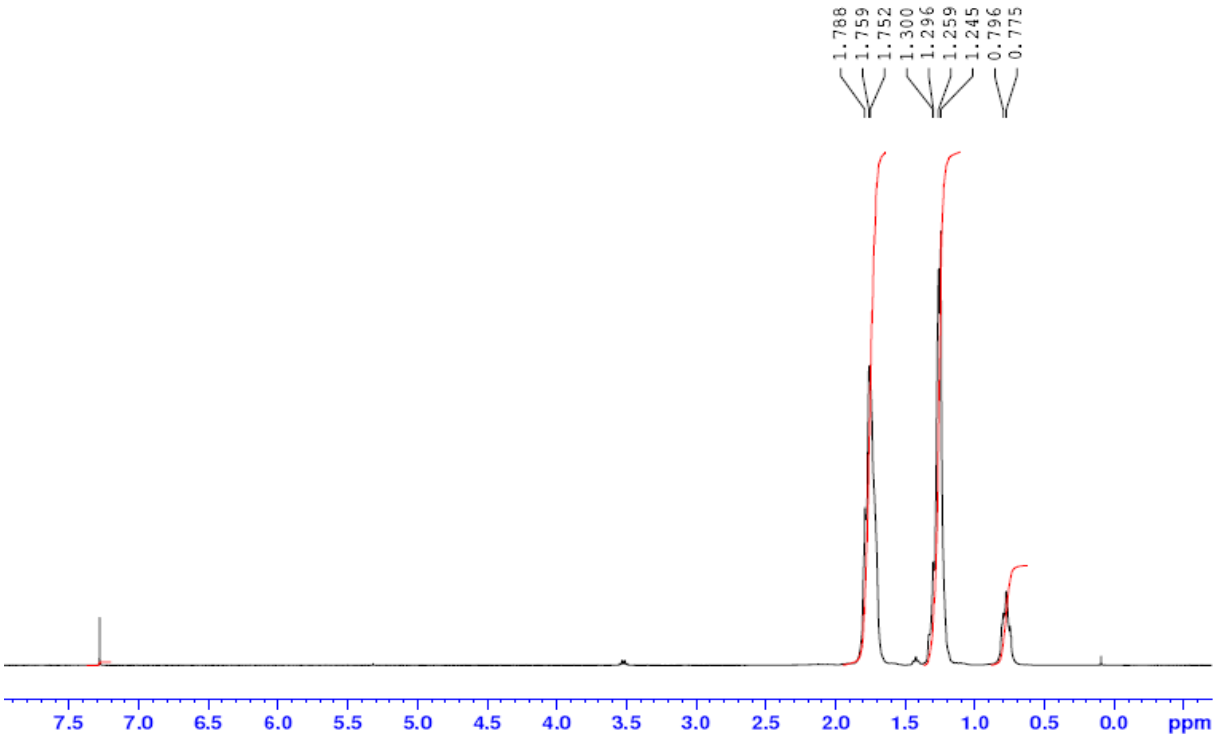

^{29}Si NMR (79.5 MHz, $CDCl_3$):

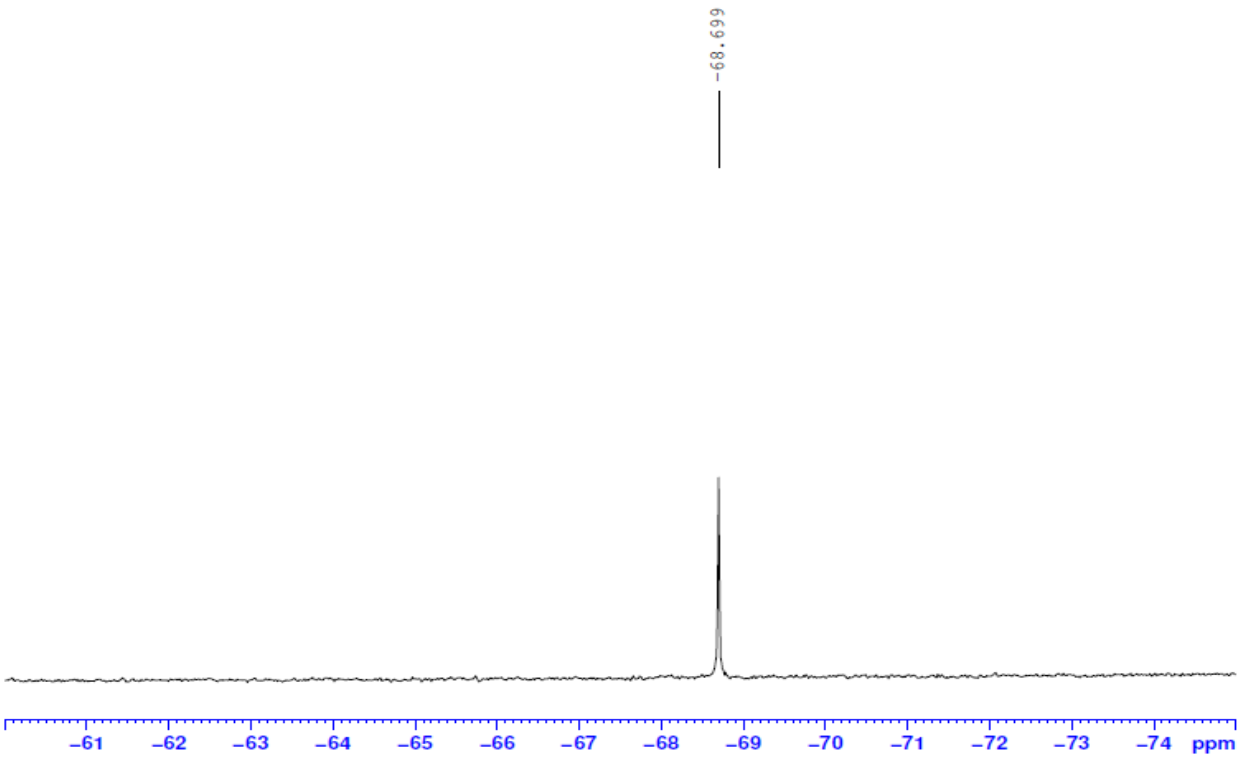

5.6.3 Synthesis of *endo*-$_{C3}$-(*c*-C_6H_{11})$_7Si_7O_9(OH)_3$ (17):

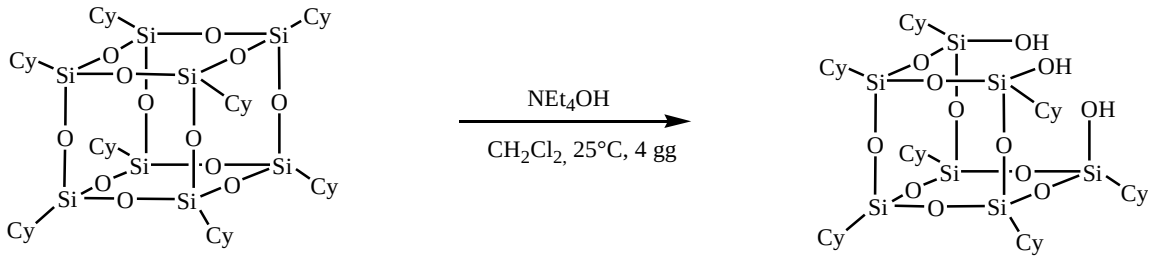

endo-$_{C3}$-(*c*-C_6H_{11})$_7Si_7O_9(OH)_3$ (7.2 g, 6.6 mmol) was prepared by a slightly modification of the procedure described for the basic catalyzed cleavage of **16**.[56] The reaction is performed at 25 °C in CH_2Cl_2 with excess of 35% aqueous Et_4NOH (27.5g, 187 mmol). After 4 days the cleavage is selective towards the formation of **17** that can be purified by chromatography on silica with CH_2Cl_2 (1.94 g, yield 30%).

^{1}H NMR (400 MHz, $CDCl_3$): (ppm) 0.75-0.78 (s, 7H, CH), 1.26-1.30 (s, 35H, CH_2CH), 1.75 (s, 35H, CH_2CH), 6.5 (m, 3H, OH)

^{29}Si NMR (79.5 MHz, $CDCl_3$): δ =-60.1, -67.7, and -69.4 ppm (3+1+3)

^{1}H NMR (400 MHz, $CDCl_3$):

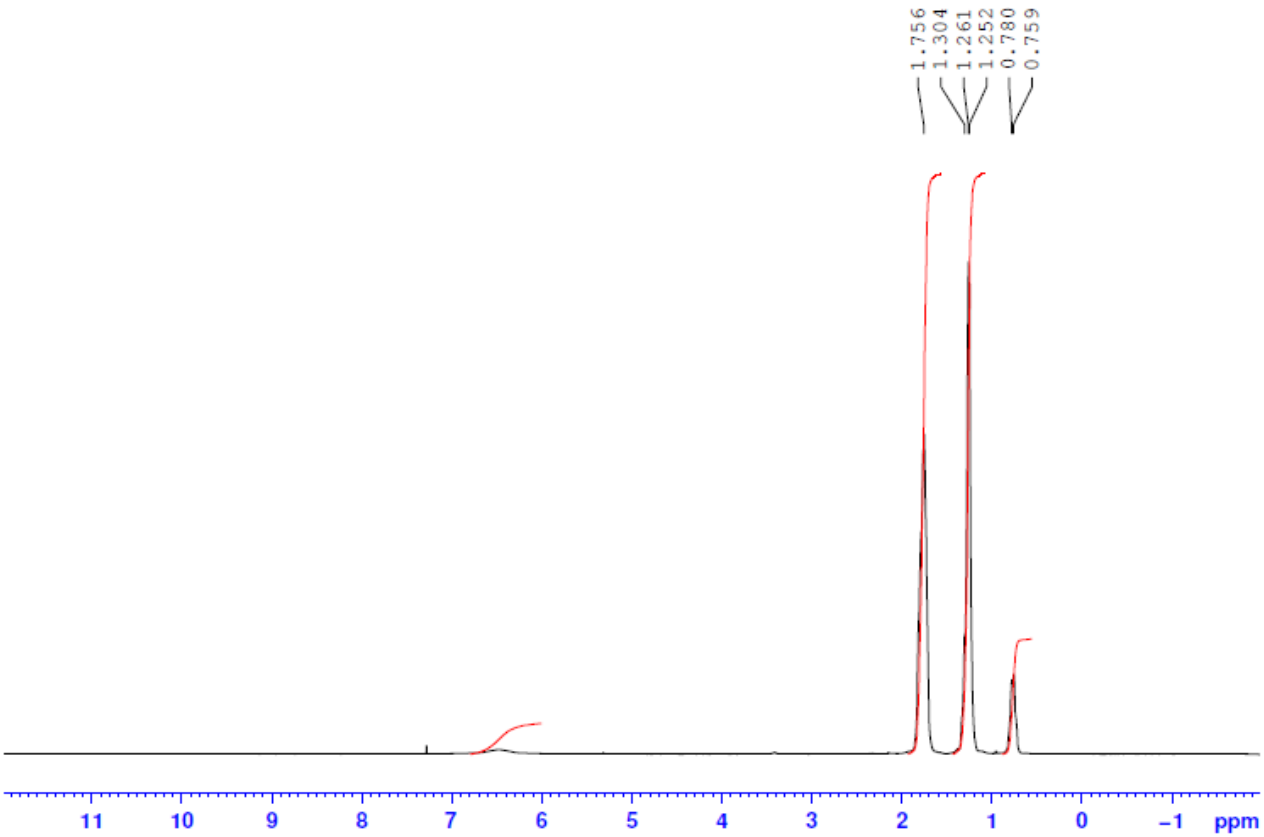

^{29}Si NMR (79.5 MHz, $CDCl_3$):

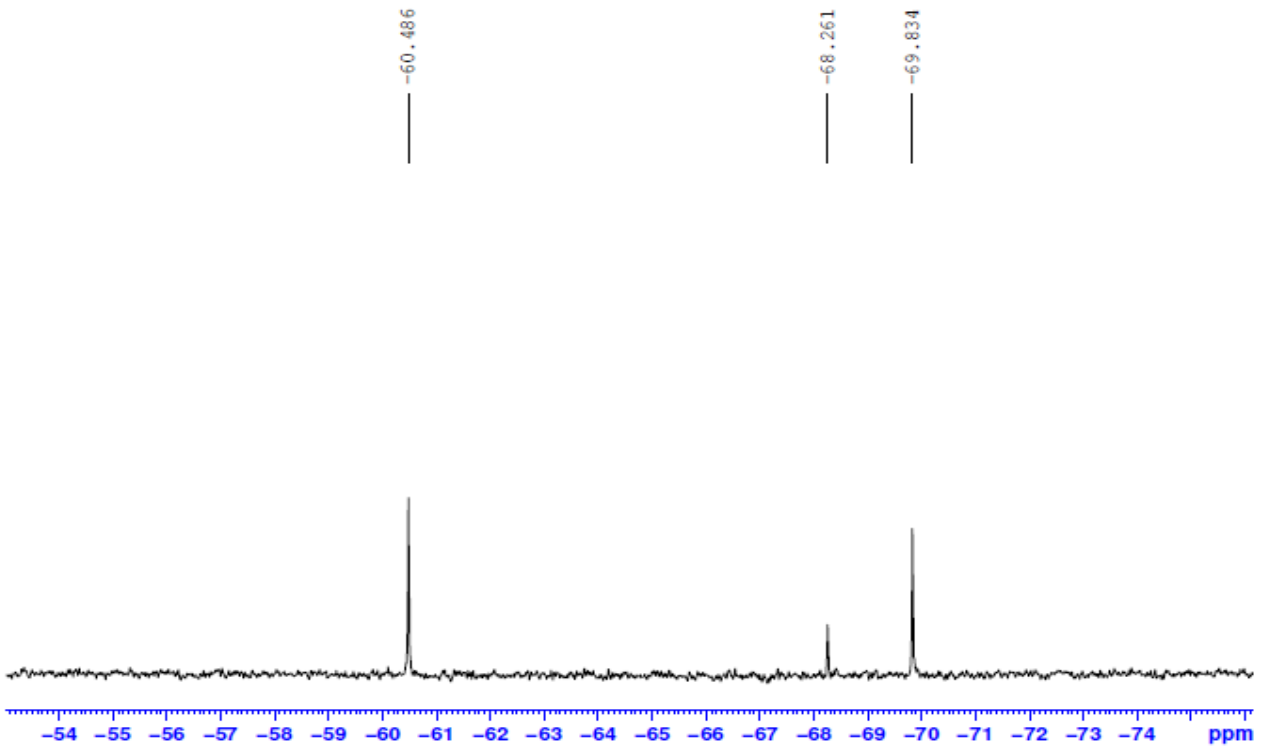

5.6.4 Synthesis of -(*c*-$C_6H_{11})_7Si_8O_{12}$ $CH=CH_2$ (18):

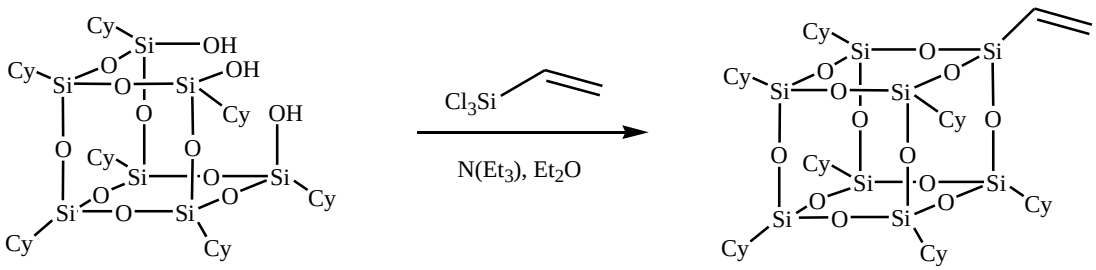

To a suspension of **17** (1 g, 1.03 mmol) in diethyl ether (60 ml) and NEt_3 (0.71 ml, 5.15 mmol), vinyltrichlorosilane (0.2 ml, 1.5 mmol) was added at room temperature. The mixture was stirred overnight at room temperature and then filtered to remove Et_3NHCl. The salt washed with ether (2 x 30 ml), brine, dried over $MgSO_4$ and the organic phases evaporated under reduced pressure to yield a white powder. The solid crystallized from dichloromethane/methanol to give **18** (650 mg, 59% yield).

^{1}H NMR (400 MHz, $CDCl_3$): (ppm) 0.78 (s, 7H, CH), 1.25-1.28 (s, 35H, CH_2CH), 1.74-1.76 (s, 35 H, CH_2CH), 5.86-6.10 (m, 3H, vinyl)

^{29}Si NMR (79.5 MHz, $CDCl_3$): δ = -68.50, -68.63, -80.64 (*Si*$CH=CH_2$). (3:4:1)

^{1}H NMR (400 MHz, $CDCl_3$):

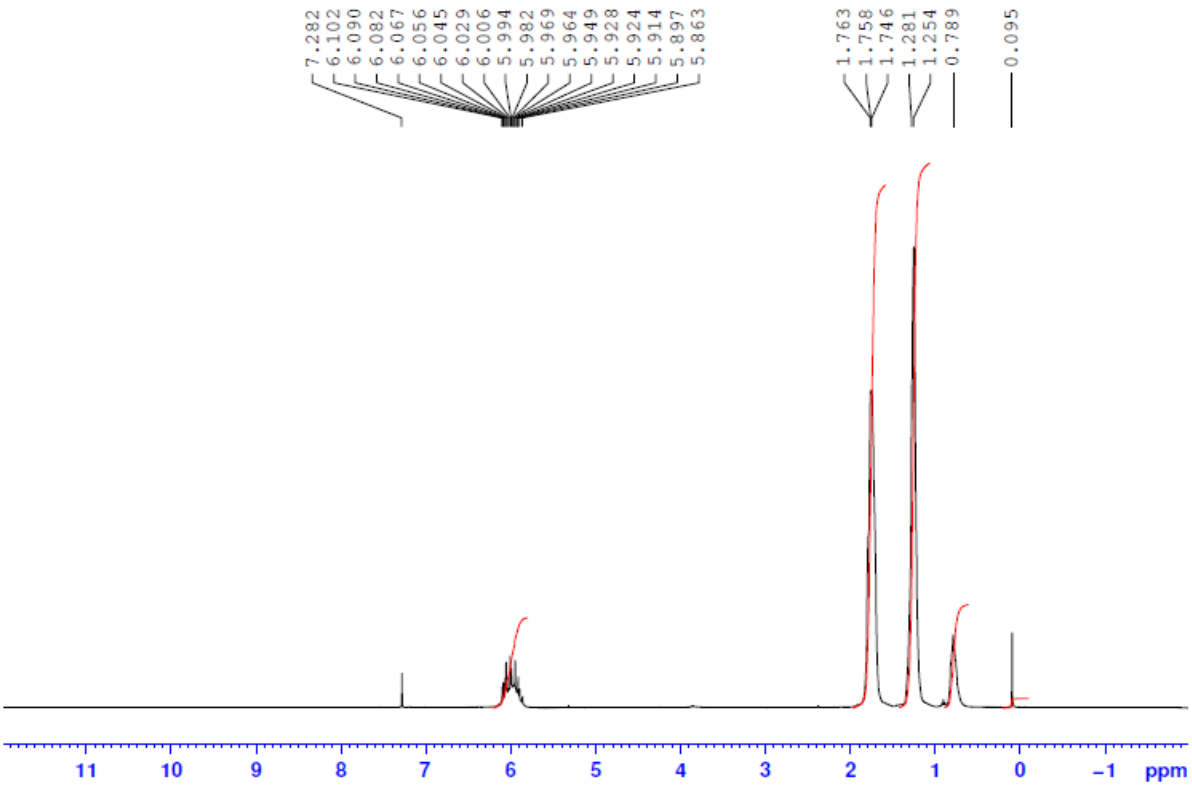

^{29}Si NMR (79.5 MHz, $CDCl_3$):

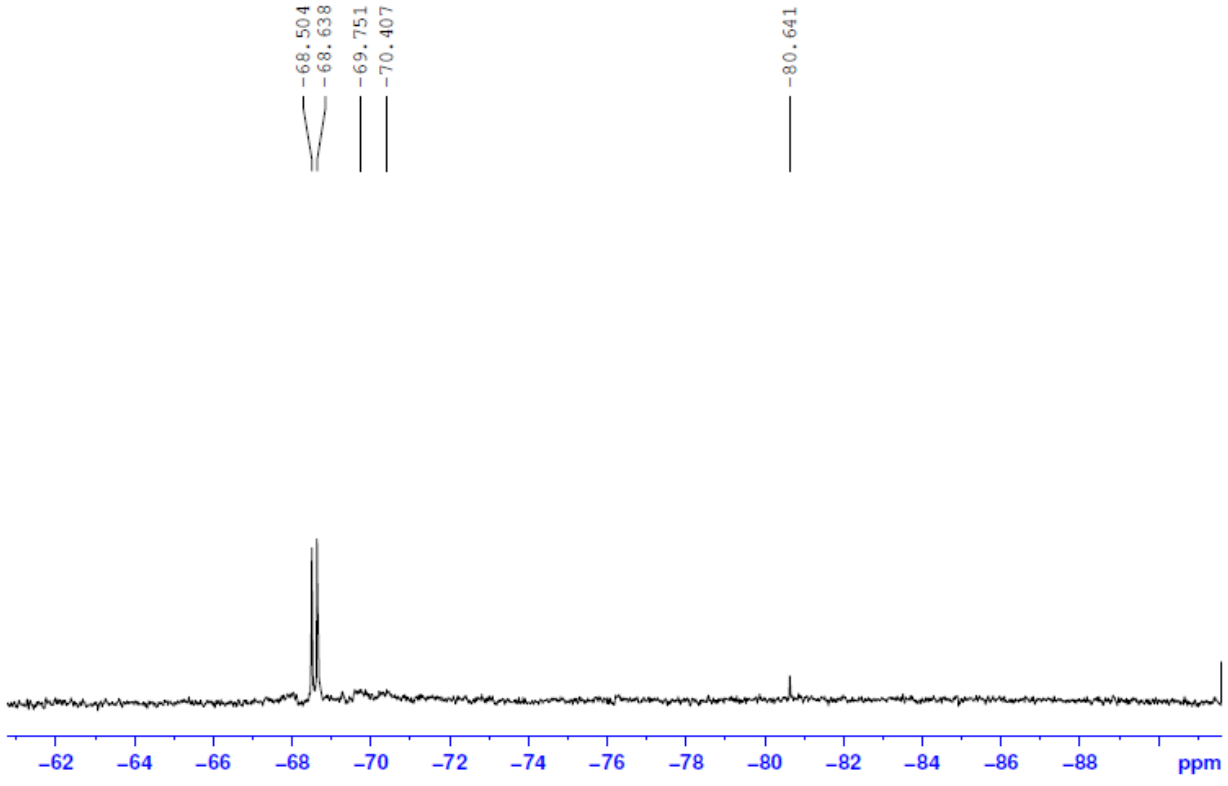

5.6.5 Synthesis of Tridecan-7-one oxime (20)

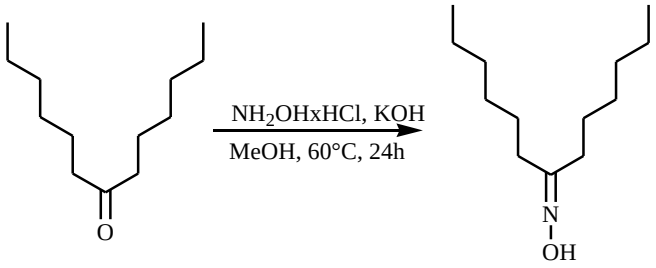

A suspension of 7-tridecanone (10 g, 126 mmol), hydroxylamine hydrochloride (6 g, 215 mmol), and 85% KOH (12 g, 430 mmol) in 250 mL methanol was stirred at 60°C for 24 h. After filtration, the filtrate was concentrated under reduced pressure and acidified with 2 N HCl. The resultant solution added to ether was washed with 2 N HCl and brine, dried over $MgSO_4$, and concentrated in vacuum to yield a pale yellow oil (10.7 g, quantitative yield).

^{1}H-NMR (400 MHz, $CDCl_3$): (ppm) 0.88–0.91 (t, 6H, CH_3), 1.30–1.31 (m, 12H, $6CH_2$), 1.52 (m, 4H, $2CH_2$), 2.20 (t, 4H, $2CH_2CH_2CNOH$), 2.33–2.35 (t, 4H, $2CH_2CHOH$).

^{1}H-NMR (400 MHz, $CDCl_3$):

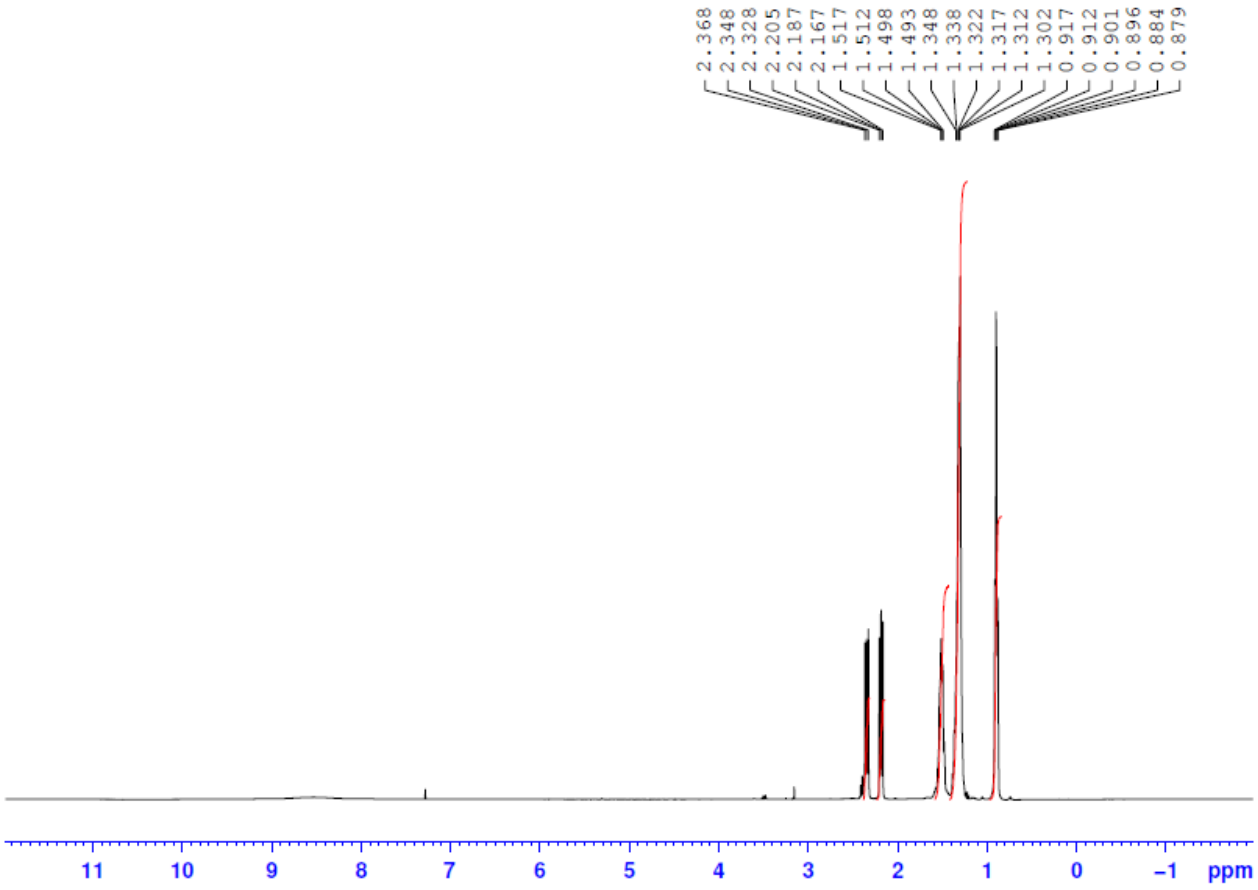

5.6.6 Synthesis of Tridecan-7-amine (21)

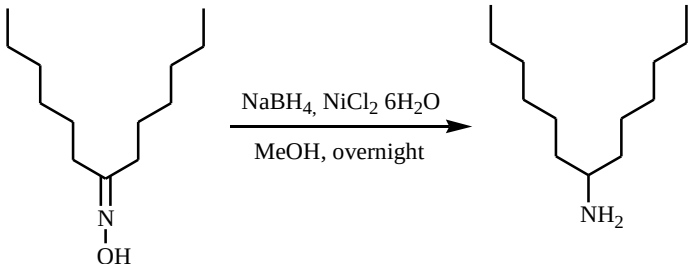

A solution of compound **20** (10.7 g, 129 mmol) and $NiCl_2x6H_2O$ (22,5 g, 94.6 mmol) in methanol was carefully added with $NaBH_4$ (8.3 g, 224 mmol), and the reaction mixture was stirred at room temperature for 24h. After, the mixture was filtrated on celite, and concentrated under reduced pressure. The resultant solution added to KOH 20% and extracted with CH_2Cl_2.The organic phase was washed with brine, dried over $MgSO_4$, and concentrated in vacuum to yield a colorless oil (7.66 g, 83% yield).

^{1}H-NMR (400 MHz, $CDCl_3$): (ppm) 0.87 (t, 6H, CH_3), 1.34 (m, 16H, $8CH_2$), 1.4 (m, 2H, C*H*$_2$CHNH$_2$), 1.46 (m, 2H,C*H*$_2$CHNH$_2$), 2.70 (m, 1H, C*H*NH$_2$);

^{1}H-NMR (400 MHz, $CDCl_3$):

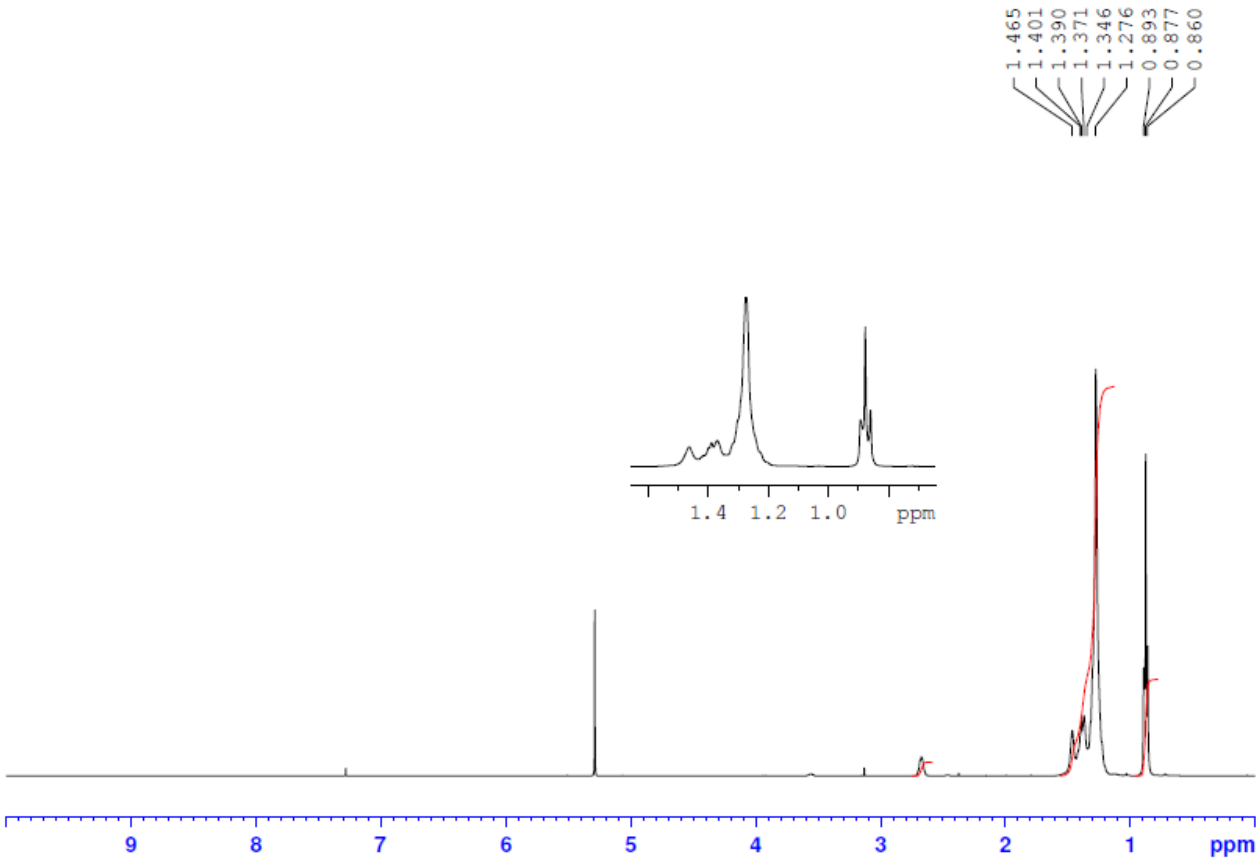

5.6.7 Synthesis of *N*,*N*-Bis(1-hexylheptyl)perylene-3,4,9,10-tetracarboxylbisimide (22)

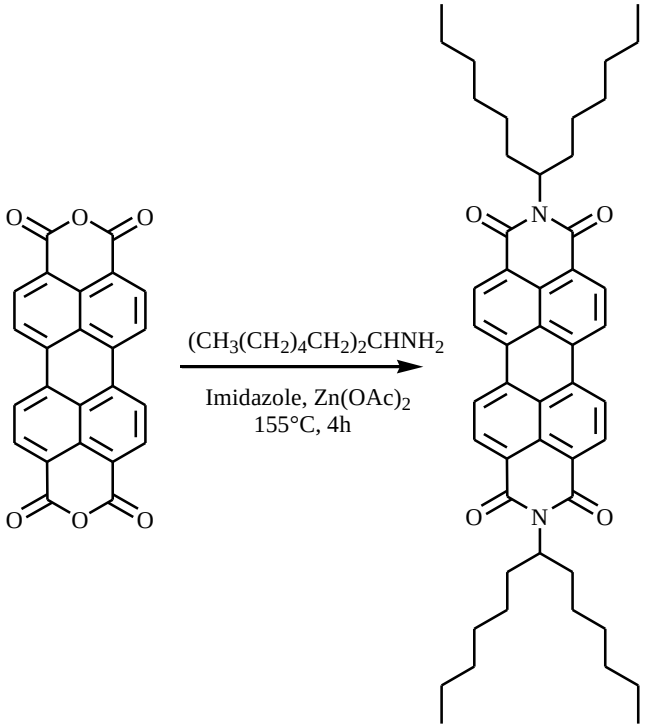

Compound **21** (1.79 g, 6.01 mmol) and perylene-3,4,9,10- tetracarboxylic dianhydride (1.00 g, 2.55 mmol), zinc acetate (210 mg, 1.14 mmol), and imidazole (3.00 g, 44.1 mmol) were stirred at 155°C for 4 h. The reaction mixture was then added with HCl conc. and stirred overnight. The resultant red precipitate was collected by filtration and washed with water and methanol to yield a red powder (2.12 g, 82.5% yield).

^{1}H-NMR (400 MHz, $CDCl_3$): (ppm) 0.8–0.9 (t, 12H, $4CH_3$), 1.15–1.4 (m, 32H, $16CH_2$), 1.8–1.9 (m, 4H, $2CH_2CHN$), 2.2 2.3 (m, 4H, $2CH_2CHN$), 5.15–5.25 (m, 2H, 2CHN), 8.6–8.7 (m, 8H, perylene).

^{13}C-NMR (100 MHz, $CDCl_3$): (ppm) 14.03, 22.58, 26.94, 29.21, 31.76, 32.38, 54.78, 122.95, 126.43, 129.58, 134.47.

^{1}H NMR (400 MHz, $CDCl_3$):

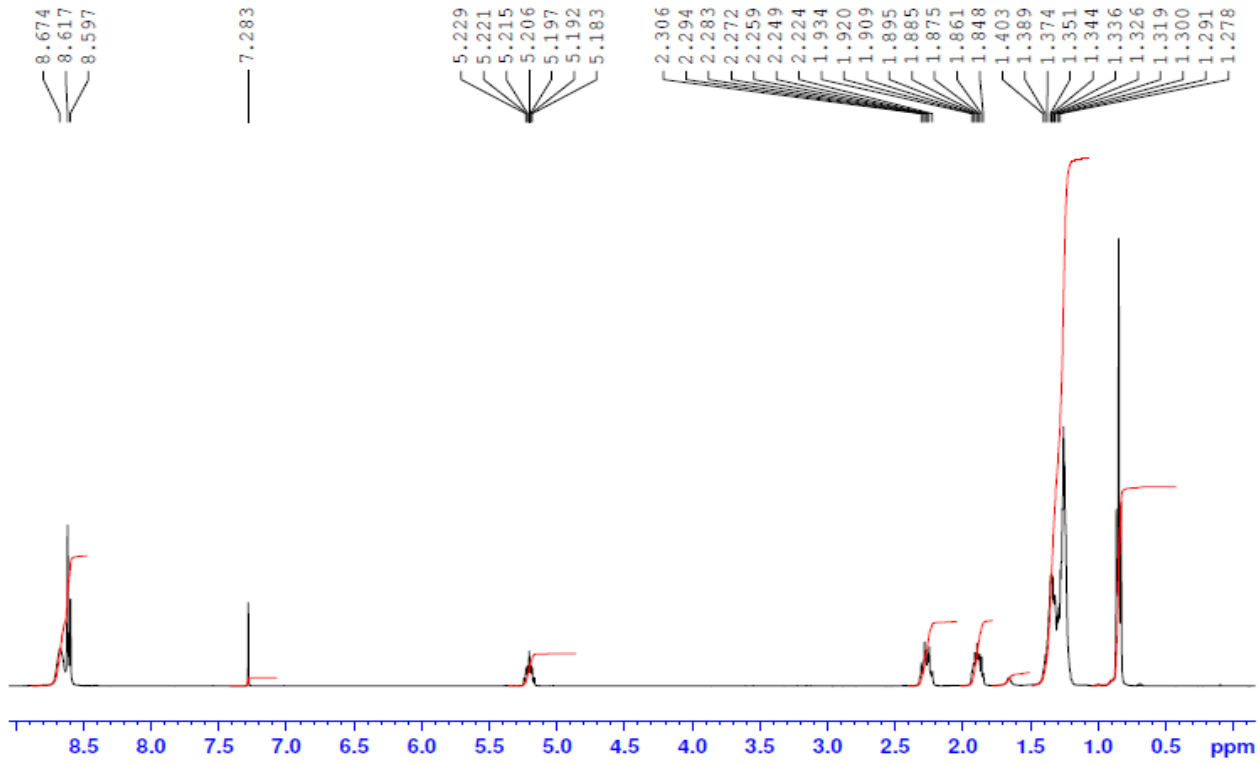

^{13}C NMR (100 MHz, $CDCl_3$):

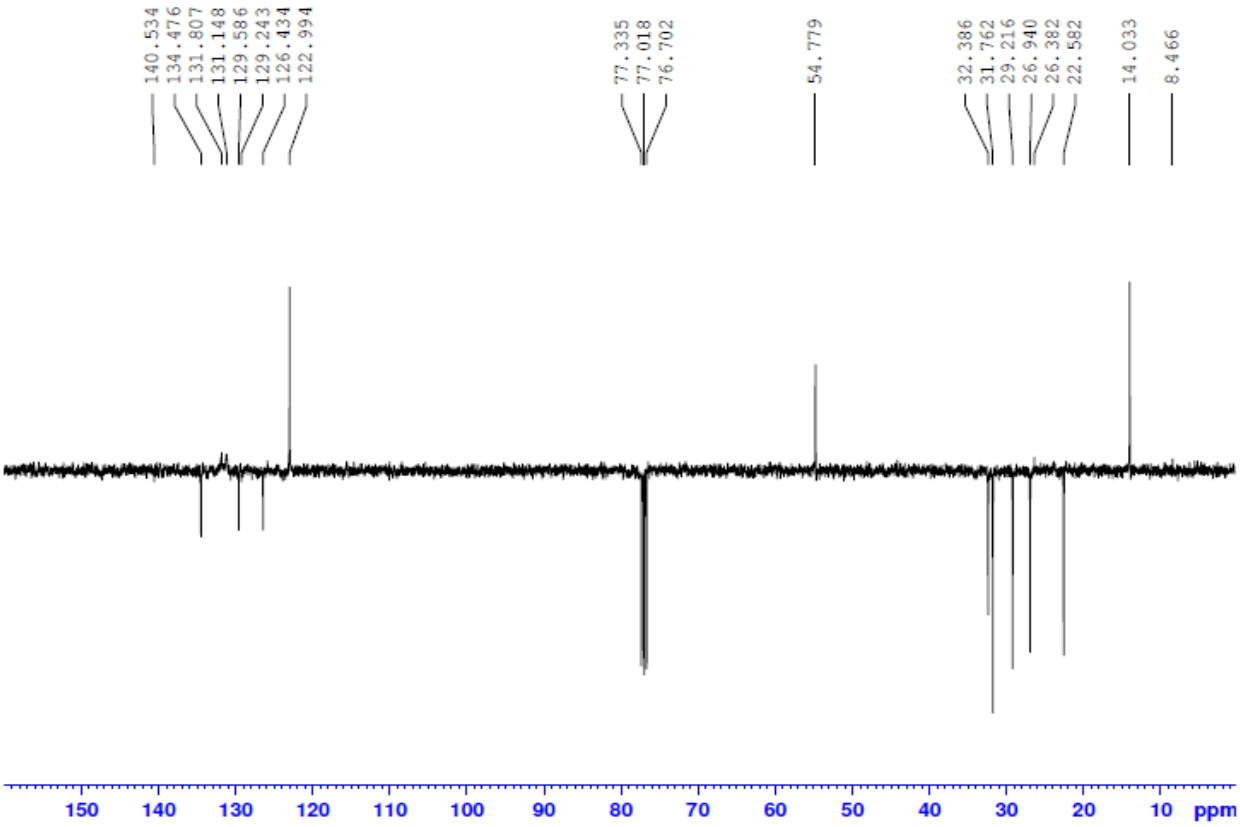

5.6.8 Synthesis of *N*-(1-Hexylheptyl)perylene-3,4,9,10-tetracarboxyl-3,4-anhydride-9,10-imide (24)

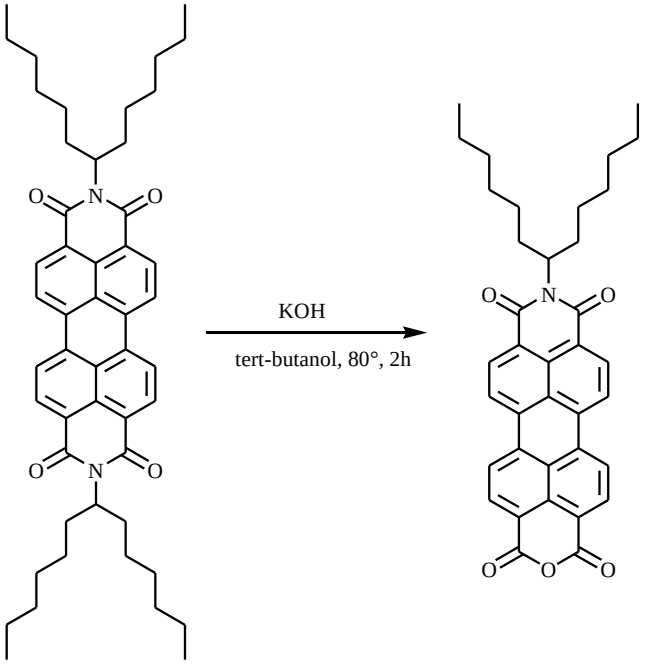

Compound **22** (4.5 g, 6.0 mmol) was added to 120 mL *tert*-butanol containing potassium hydroxide (1.1 g, 20.55 mmol) and the mixture was refluxed at 80°C for 30 min. The reaction was stopped and HCl conc. was then added to the reaction mixture. After stirring overnight, a red precipitate was collected by filtration, washed with water, pentane and methanol to yield a red powder (3.48 g, 92% yield).

^{1}H-NMR (400 MHz, $CDCl_3$): (ppm) 0.8–1.0 (t, 6H, CH_3), 1.2–1.5 (m, 16H, $8CH_2$), 1.8–1.9 (m, 2H, C*H*$_2$CHN), 2.2–2.3 (m, 2H, C*H*$_2$CHN), 5.15–5.2 (m, 1H, CHN), 7.5–7.6 (d, 2H, perylene), 7.7–7.8 (d, 2H, perylene), 8.65– 8.75 (d, 4H, perylene);

^{13}C-NMR (100 MHz, $CDCl_3$): (ppm) (ppm) 14.02, 22.57, 26.92, 29.19, 31.74, 32.35, 54.93, 106.19, 119.01, 123.01, 123.90, 133.52, 136.39.

Elemental analysis $C_{37}H_{35}NO_5$: found %C 77.35; %H 6.14; %N 2.44; calculated %C 77.46; %H 6.15; %N 2.44.

^{1}H NMR (400 MHz, $CDCl_3$):

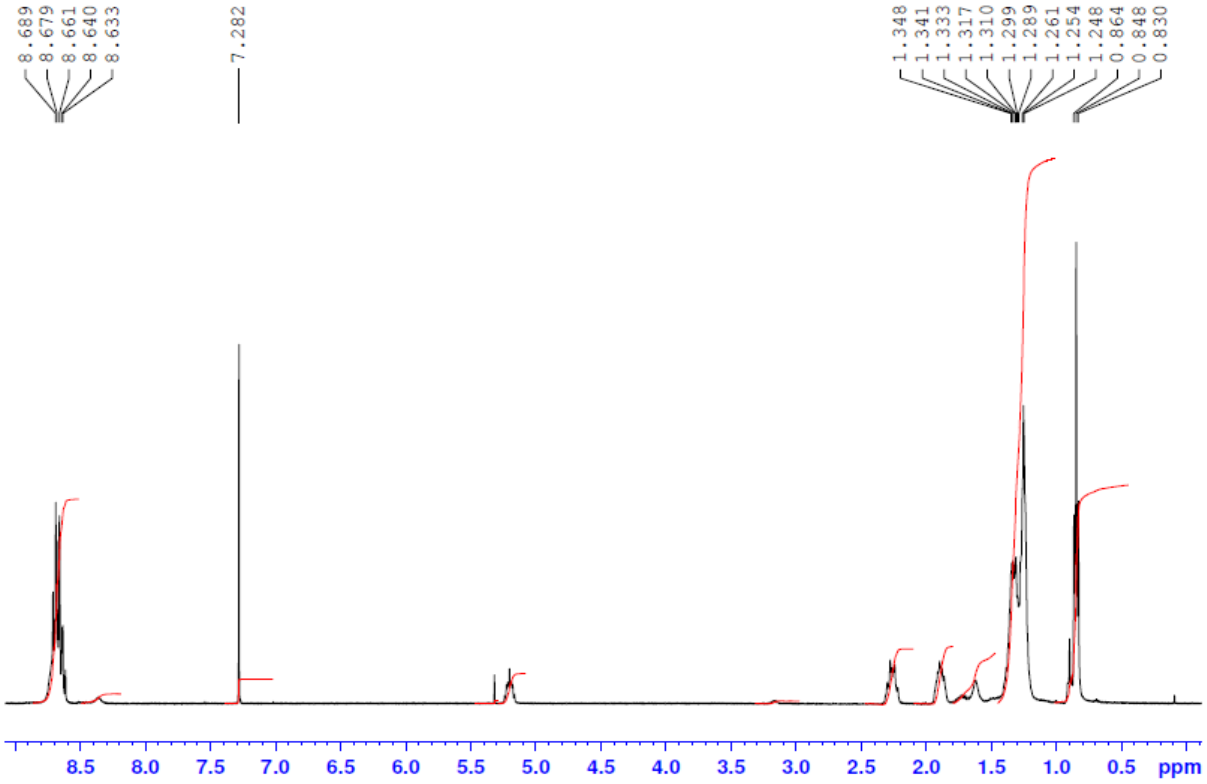

^{13}C NMR (100 MHz, $CDCl_3$):

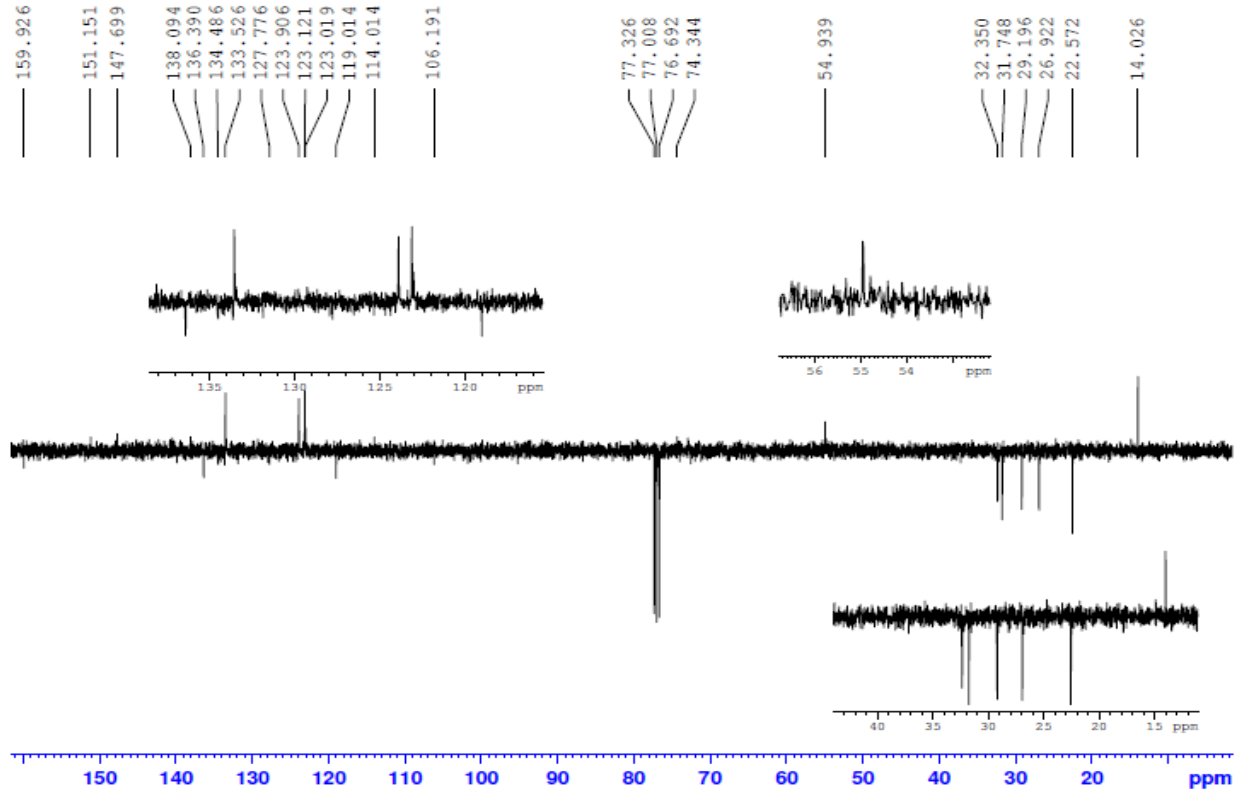

5.6.9 Synthesis of 2-Allyl-9-(1-hexylheptyl)anthra[2,1,9-def;6,5,10-d'e'f']diisoquinoline-1,3,8,10-tetraone (25a):

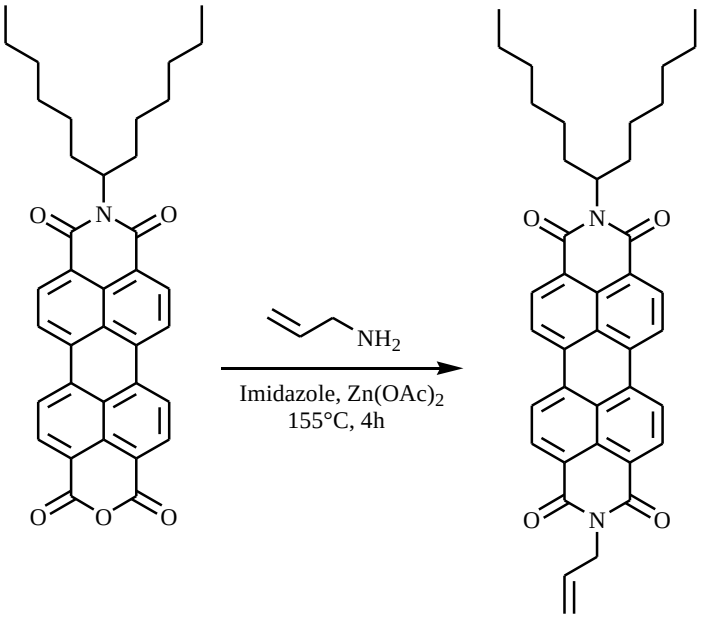

Compound **24** (0.3 g, 0.52 mmol), imidazole (13.0 g) and a very small amount of $Zn(OAc)_2$ were heated together at 140°C, then added dropwise with allyl amine (0.12 mg, 2.09 mmol), and stirred at 140°C for 4 h. The mixture was allowed to cool to 60°C, then treated with acetic acid (160 mL), and 2M HCl (50 mL), collected by vacuum filtration, washed with water, pentane, ethanol and purified by column chromatography (silica gel, chloroform) to give a bright-red solid (300 mg, 93%).

^{1}H NMR (400 MHz, $CDCl_3$): (ppm) 0.83 (t, J=7.0 Hz, 6H; 2xCH_3), 1.23–1.38 (m, 16H; 8xCH_2), 1.88–1.91 (m, 2H; CH_2), 2.25–2.29 (m, 2H; CH_2), 4.82 (t, J=5.9 Hz, 2H; N-CH_2), 5.16–5.21 (m, 1H; N-CH), 5.24–5.26 (m, 1H; olefin CH_2), 5.35–5.38 (m, 1H; olefin CH_2), 5.98–6.05 (m, 1H; olefin CH), 8.55–8.68 ppm (m, 8H; 8 aromatic CH).

^{13}C NMR (100 MHz, $CDCl_3$): (ppm) 14.05, 22.60, 26.98, 29.25, 31.77, 32.38, 42.55, 54.88, 118.15, 122.71, 125.98, 126.06, 129.08, 129.34, 133.88, 134.37, 162.76.

^{1}H NMR (400 MHz, $CDCl_3$):

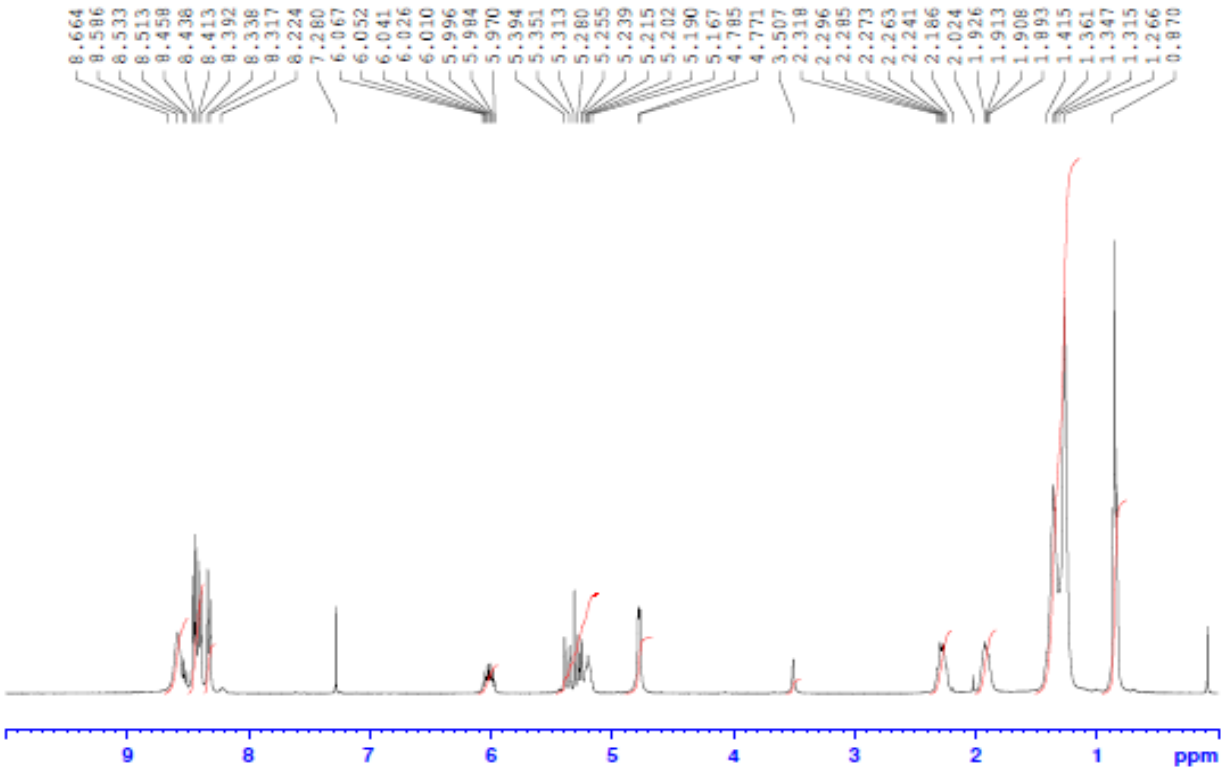

^{13}C NMR (100 MHz, $CDCl_3$):

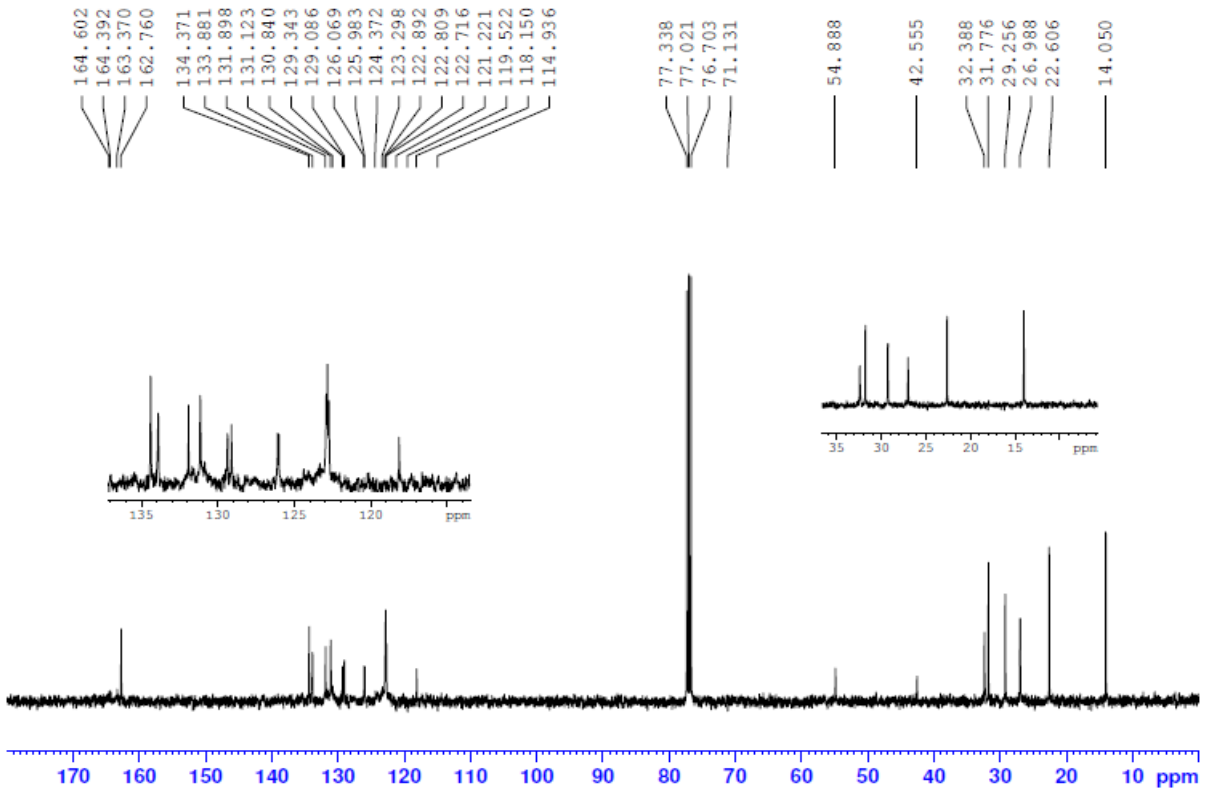

5.6.10 Synthesis of 2-(1-Hexyl-heptyl)-9-(4-iodo-phenyl)-anthra[2,1,9-def;6,5,10-d'e'f']diisoquinoline-1,3,8,10-tetraone (25c):

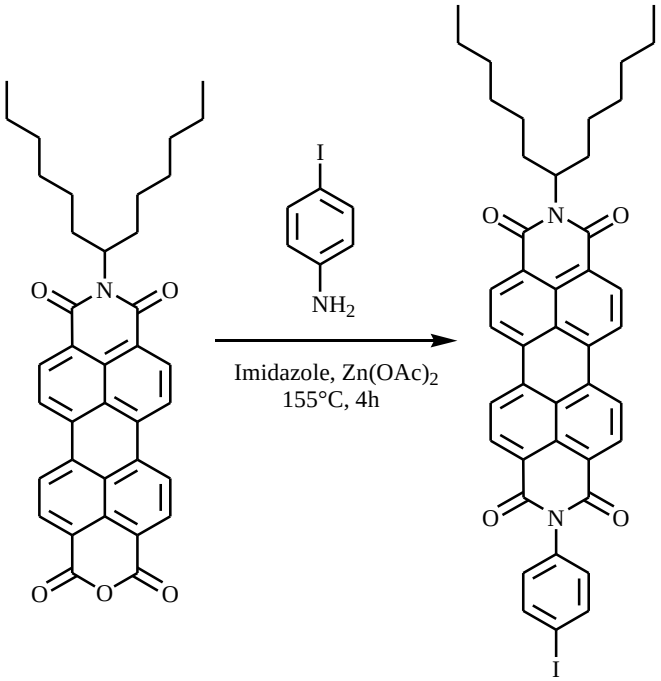

Compound **24** (0.5 g, 0.87 mmol), imidazole (20.0 g), p-iodoaniline (0.23 g, 1.05 mmol) and a very small amount of $Zn(OAc)_2$ were stirred at 140°C for 4 h. The mixture was allowed to cool to 60°C, then treated with acetic acid (160 mL), precipitated with 2M HCl (100 mL), collected by vacuum filtration, washed with water, pentane and ethanol to give a bright-red solid (600 mg, 91%).

^{1}H NMR (400 MHz, $CDCl_3$): δ (ppm) 0.83 (t, 6H, 2 CH_3), 1.23-1.38 (m, 16H, 8CH_2), 1,88-1.91 (m, 2H, CH_2CHN), 2.25-2.29 (m, 2H, CH_2CHN), 7.2-7.9 (m, 4H, aromatic), 8.55-8.68 (m, 8H, aromatic).

^{13}C NMR (100 MHz, $CDCl_3$): δ (ppm) 14.03, 22.58, 26.94, 29.21, 31.76, 32.37, 54.87, 94.64, 123.04-138.66, 163.32

Elemental analysis $C_{43}H_{39}N_2O_4$: found %C 66.67; %H 5.07; %N 3.62; calculated %C 66.37; %H 5.13; %N 3.61.

^{1}H NMR (400 MHz, $CDCl_3$):

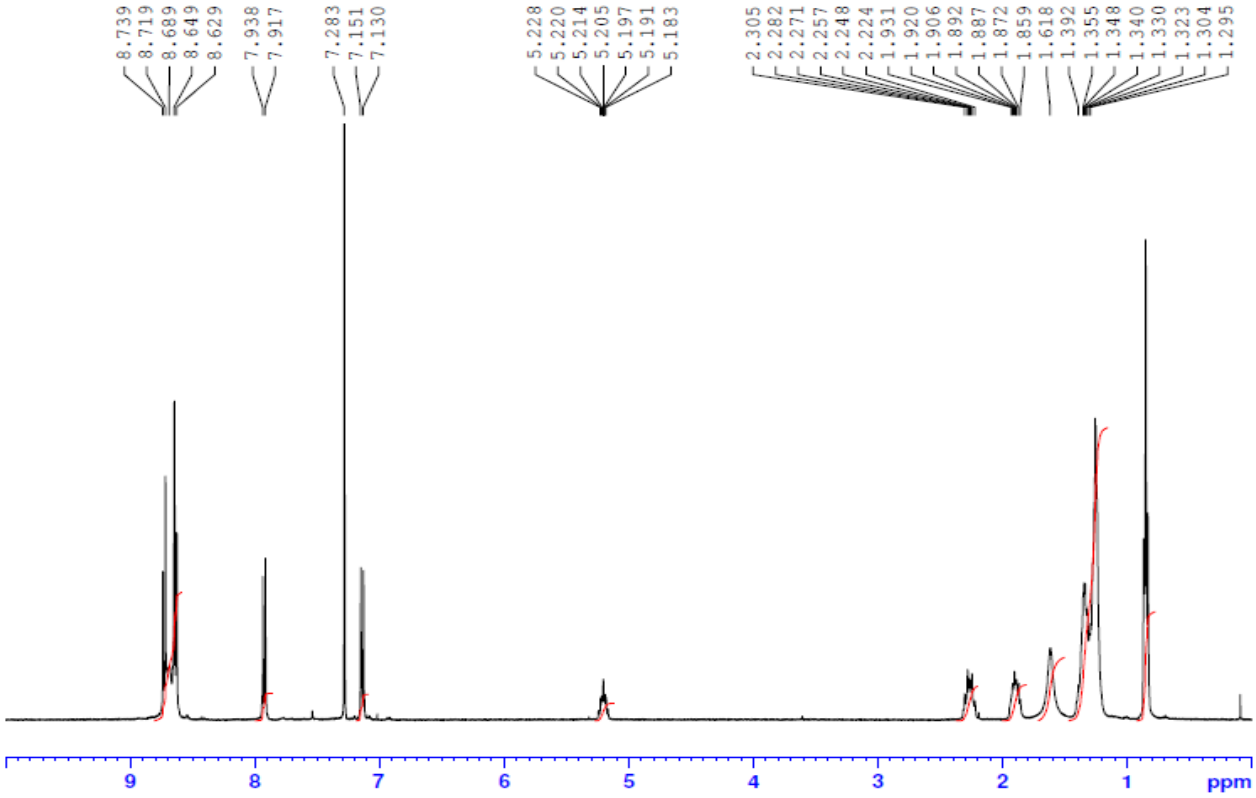

^{13}C NMR (100 MHz, $CDCl_3$):

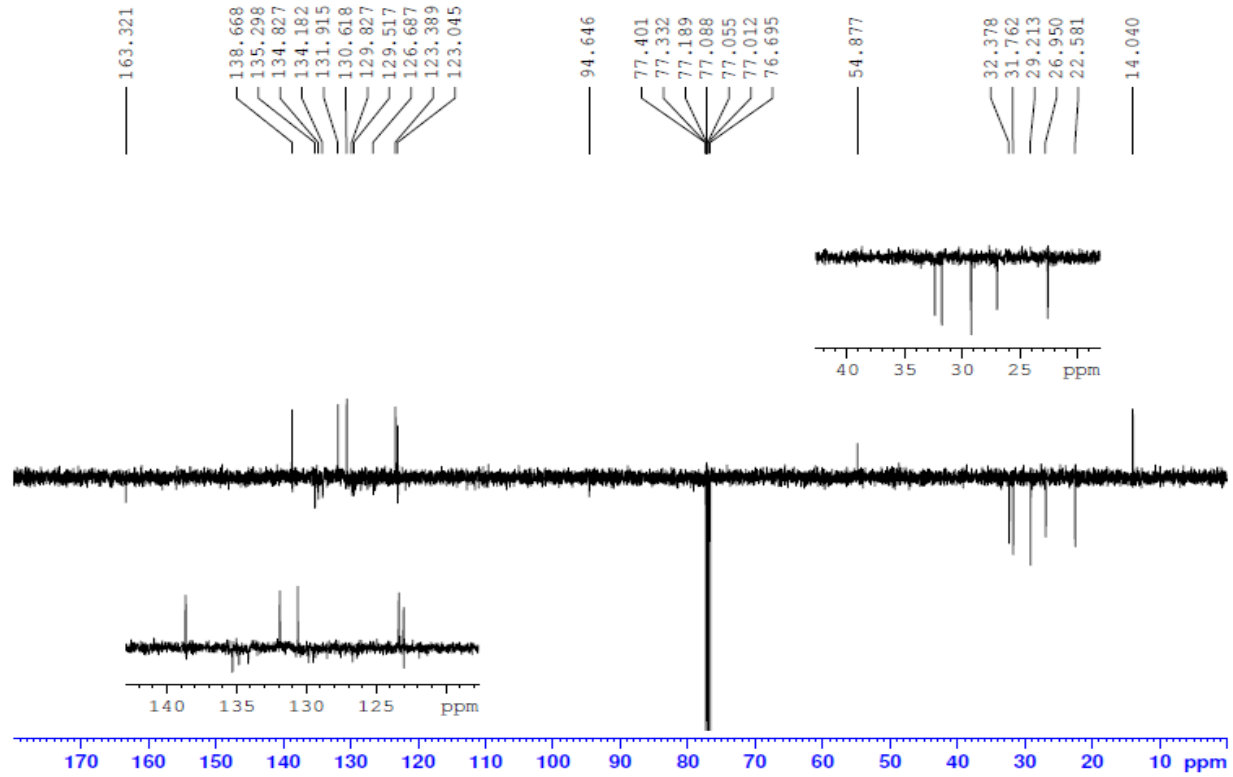

5.6.11 Synthesis of 2-(1-Hexyl-heptyl)-9-(4-bromo-phenyl)-anthra[2,1,9-def;6,5,10-d'e'f']diisoquinoline-1,3,8,10-tetraone (25b):

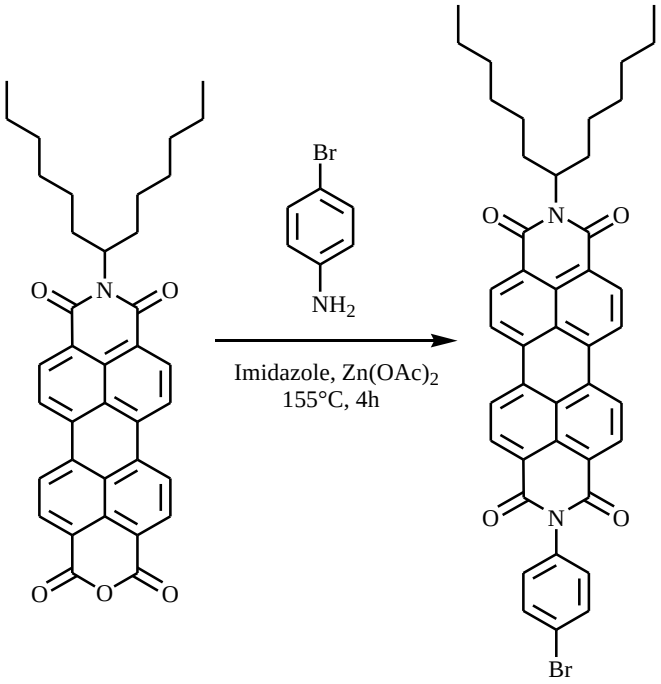

Compound **24** (1.00 g, 1.74 mmol), imidazole (40.0 g), p-bromoaniline and a very small amount of $Zn(OAc)_2$ were stirred at 140°C for 4 h. The mixture was allowed to cool to 60°C, then treated with acetic acid (160 mL), precipitated with 2M HCl (200 mL), collected by vacuum filtration, washed with water, pentane and ethanol to give a bright-red solid (690 mg, 65%).

^{1}H NMR (400 MHz, $CDCl_3$): δ (ppm) 0.83 (t, 6H, 2 CH_3), 1.23-1.38 (m, 16H, 8CH_2), 1,88-1.91 (m, 2H, CH_2CHN), 2.25-2.29 (m, 2H, CH_2CHN), 7.2-7.9 (m, 4H, aromatic), 8.55-8.68 (m, 8H, aromatic).

^{13}C NMR (100 MHz, $CDCl_3$): δ (ppm) 14.06, 22.59, 26.98, 29.21, 31.76, 32.76, 54.90, 122.95, 123.31, 126.25, 126.53, 129.42, 129.69, 130.42, 131.77, 132.67, 134.02, 135.13, 163.26.

Elemental Analysis $C_{43}H_{39}BrN_2O_4$: found %C 70.97; %H 5.40; %N 3.85; calculated %C 69.87; %H 5.5; %N 3.72.

^{1}H NMR (400 MHz, $CDCl_3$):

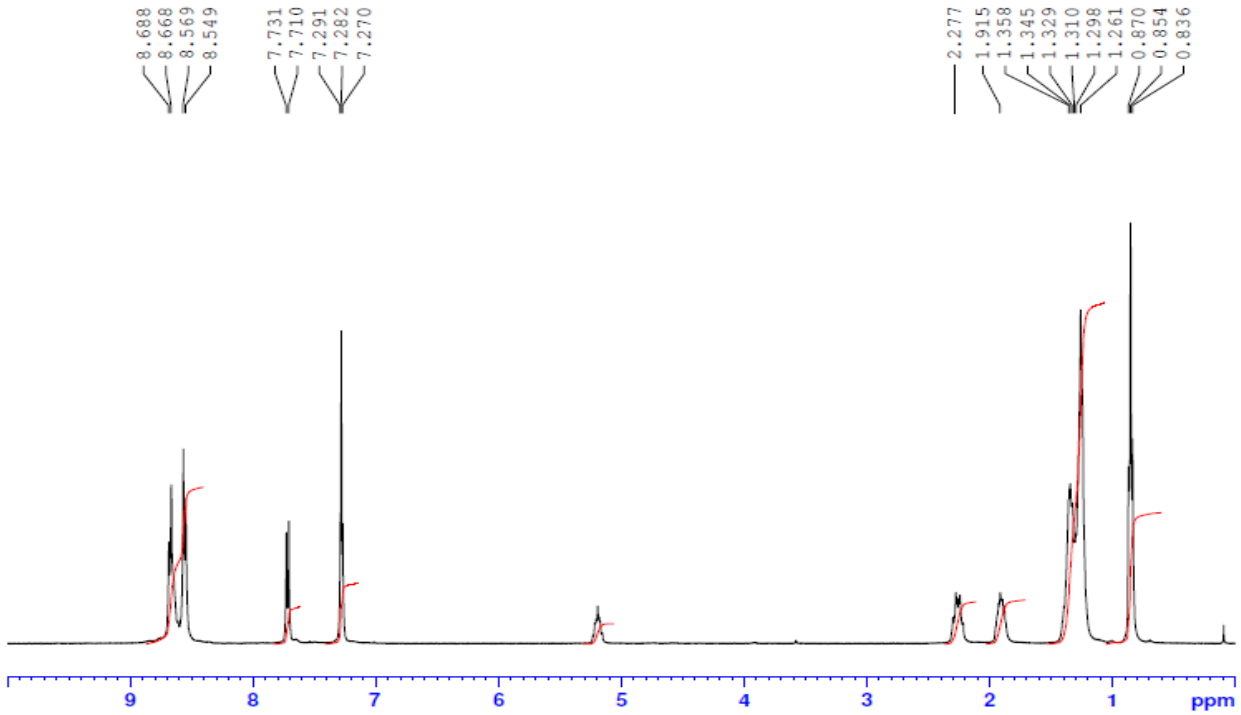

^{13}C NMR (100 MHz, $CDCl_3$):

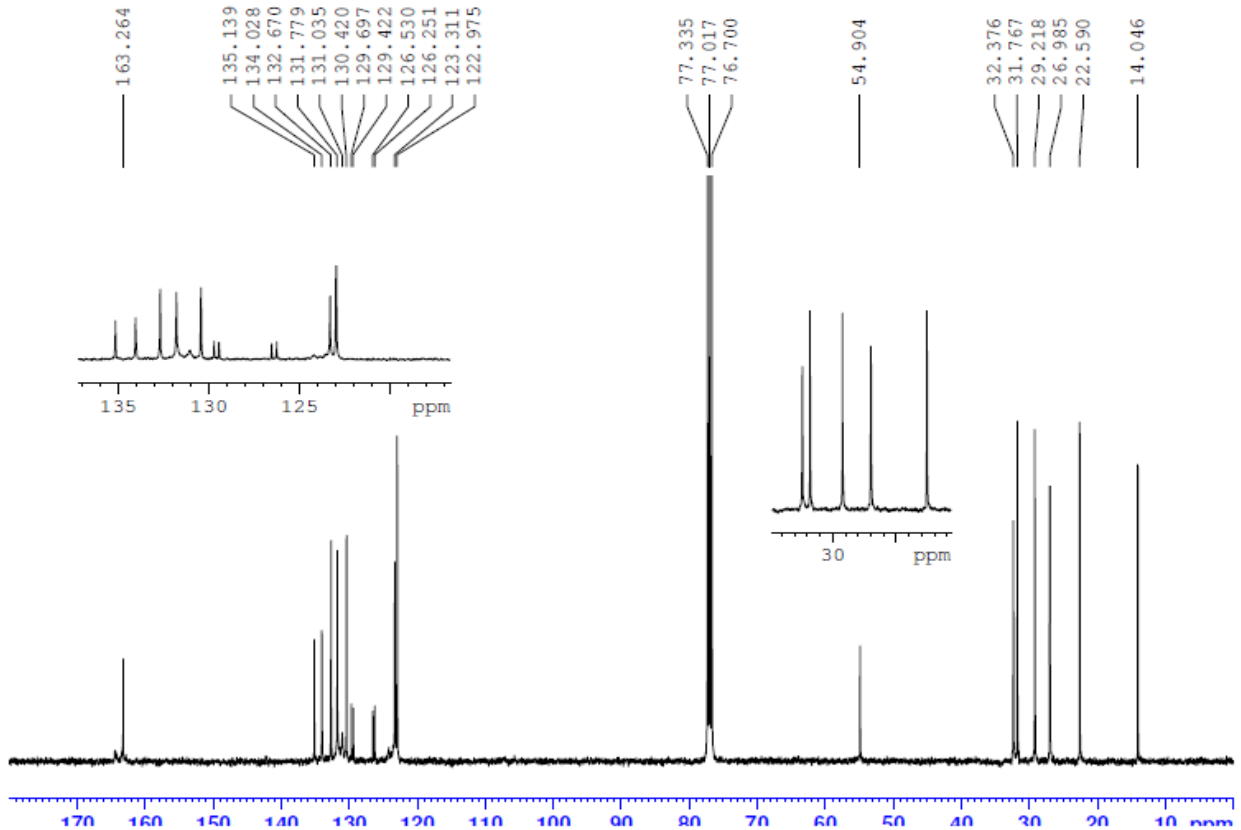

5.6.12 Synthesis (*c*-$C_6H_{11})_7Si_8O_{12}$-2-Propyl-9-(1-hexyl-heptyl)-anthra[2,1,9-def;6,5,10-d'e'f']diisoquinoline-1,3,8,10-tetraone (27):

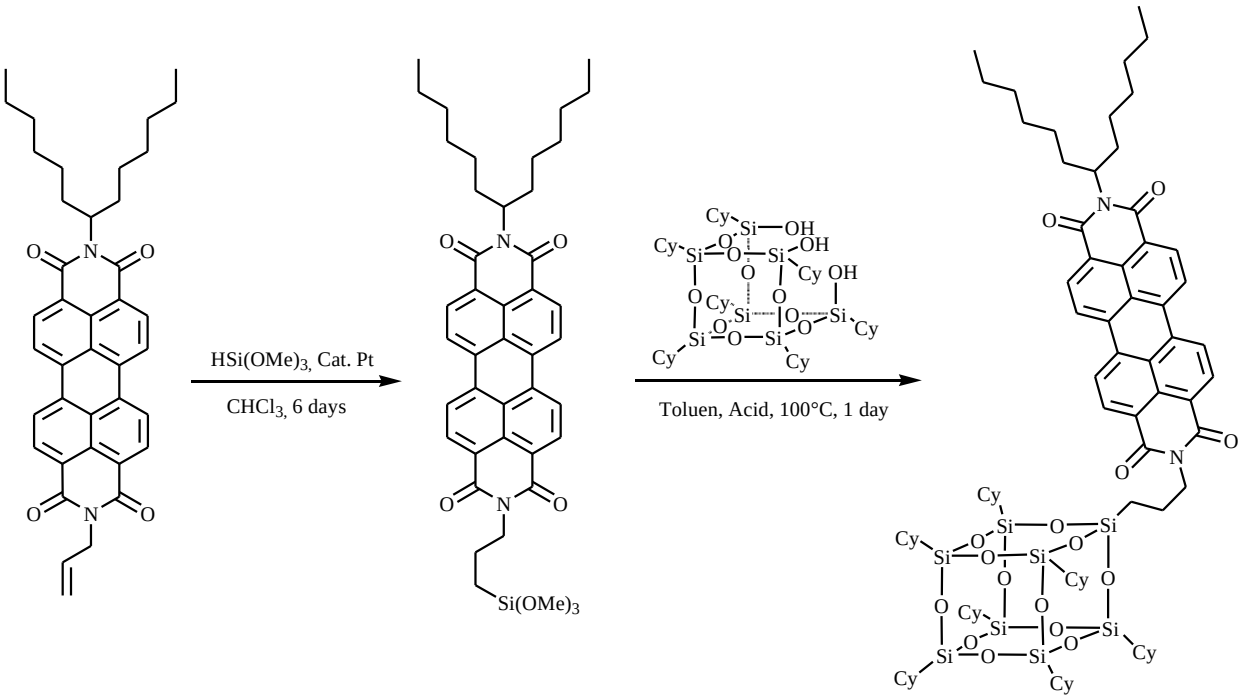

Compound **25a** (300 mg, 0,49 mmol) was dissolved in anhydrous chloroform (40 mL) under nitrogen, then trimethoxysilane (4 mL, 0.55 mmol) and Karstedt catalyst (10 mg) were slowly added dropwise. The mixture was stirred for 7 days, then concentrated under vacuum. The resulting solid dissolved in dry toluene (50 ml), added to compound **17** (0.476 g, 0.5 mmol) together with p-toluensulfonic acid (a few mg) and stirred at 100°C for 24h. The reaction mixture was concentrated under reduced pressure and purified by chromatography on silica gel (CH_2Cl_2:Hexane, 8:2) to give a red solid (193 mg, 23% yield).

^{1}H NMR (400 MHz, $CDCl_3$): δ (ppm) 0.76 (m, 7H, Cy), 0.85 (m, 6H, $2CH_3$), 1.24-1.34 (m, 55H, Cy + alchylic chain + 2 CH_2), 1.74 (m, 35H, Cy), 1.88 (m, 2H, CH_2CHN), 2.28 (m, 2H, CH_2CHN), 4.19-4.22 (m, 2H, CH_2-N),5.19-5.22 (m, 1H, CH-N), 8.41-8.61 (m, 8H, aromatic perylene).

^{13}C NMR (100 MHz, $CDCl_3$): δ (ppm) 14.03, 22.58, 22.68, 26.83, 26.89, 26.93, 27.49, 28.93, 31.76, 32.38, 42.99, 54.06, 68.16, 122.51, 123.86, 126.37, 129.38, 136.09, 163.19.

^{29}Si NMR (79.5 MHz, $CDCl_3$): δ (ppm) -67.06 (1), -68.7 (7).

Elemental Analysis $C_{82}H_{118}N_2O_{16}Si_8$: found %C 59.99; %H 7.55; %N 1.42; calculated %C 61.08; %H 7.38; %N 1.74.

Mass: [M^+] 1613 (FAB^+)

^{29}Si NMR (79.5 MHz, $CDCl_3$):

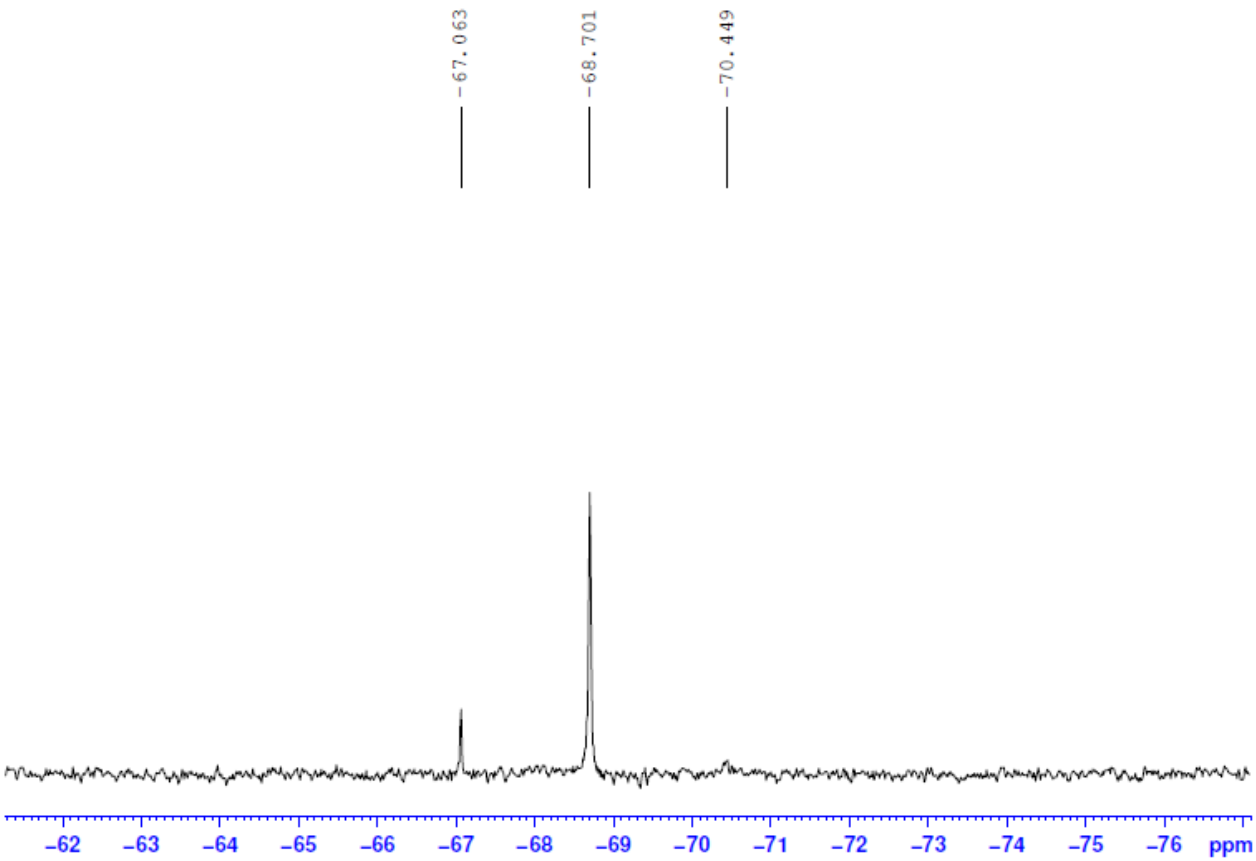

^{1}H NMR (400 MHz, $CDCl_3$):

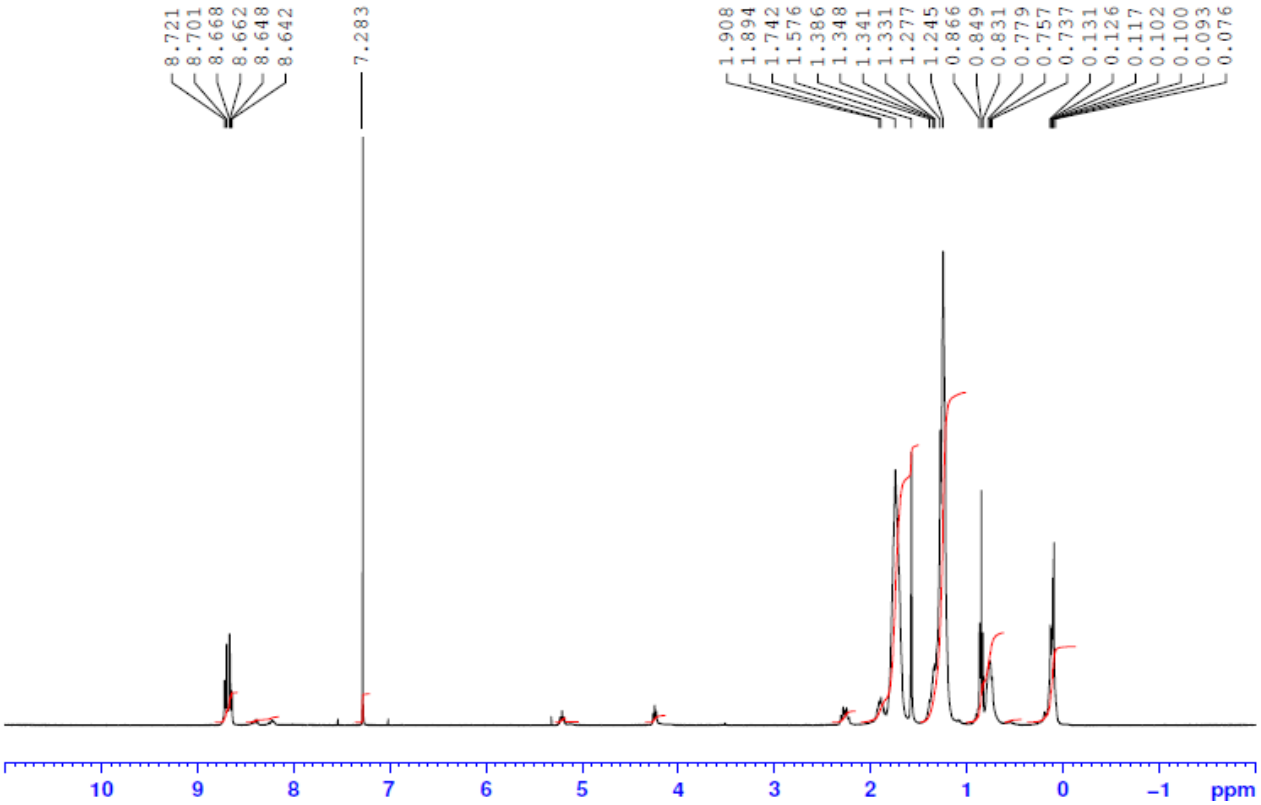

^{13}C NMR (100 MHz, $CDCl_3$):

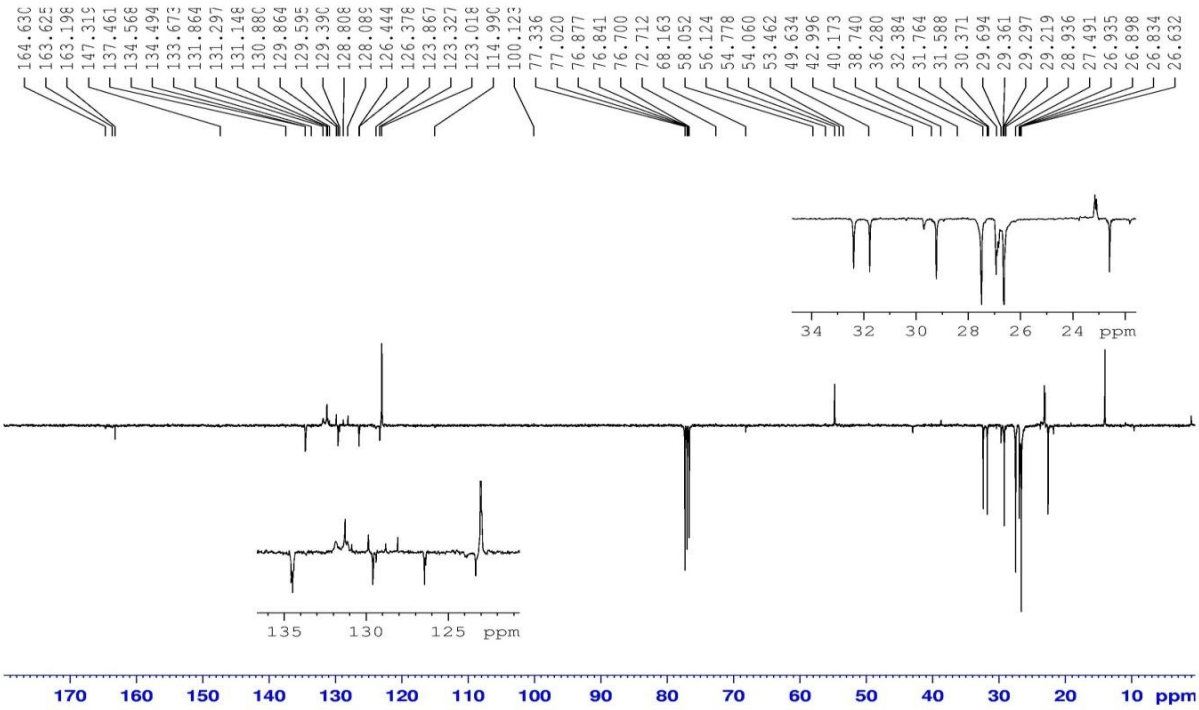

5.6.13 Synthesis of vinylsilsesquioxane-4-[2-(1-Hexyl-heptyl)-9-(phenyl)-anthra[2,1,9-def;6,5,10-d'e'f']diisoquinoline-1,3,8,10-tetraone] (28)

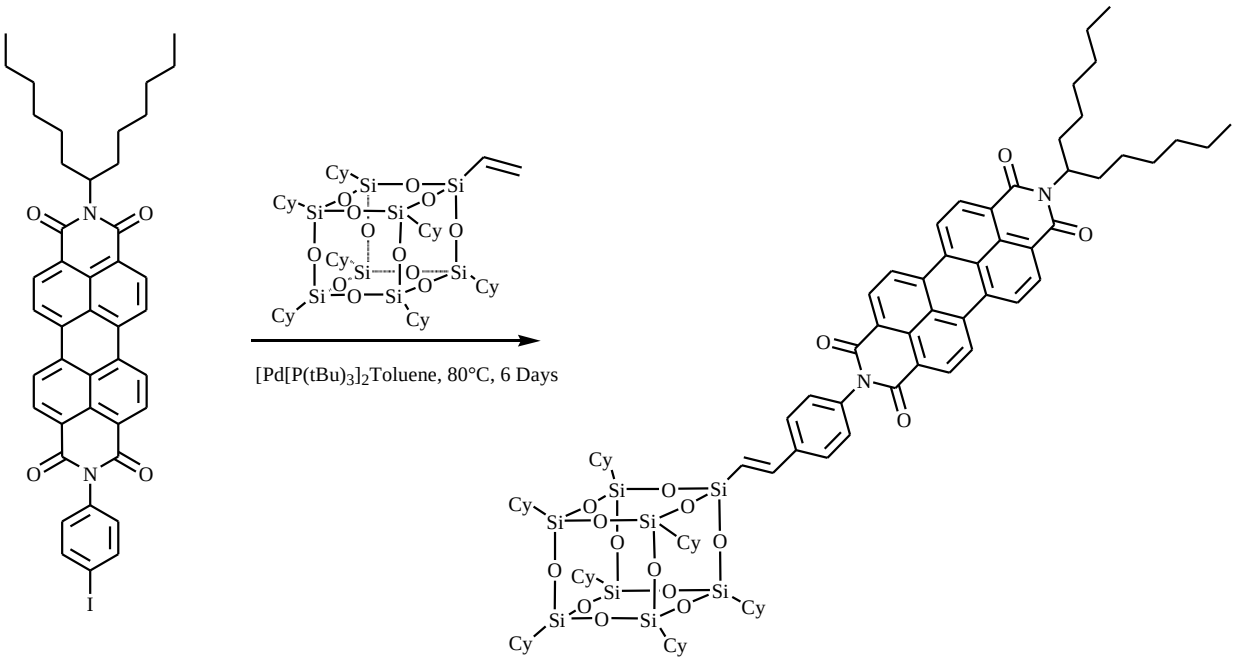

Compound **25c** (313 mg, 0.4 mmol), compound **18** (416 mg, 0.4 mmol) and bis(tri-t-butylphosphine)-palladium(0) [Pd[P(*t*Bu)$_3$]$_2$] were added into a 100-ml Schlenk flask under N_2 atmosphere. Anhydrous toluene (40 ml), and dicyclohexylmethylamine (Cy_2NCH_3) (0.103 ml, degassed under nitrogen for 15 min prior to use) were added, then 3 freeze-pump-thaw cycles were performed. The reaction was stirred for 6 days at 80°C. On reaction completion, the mixture was filtered on celite and the solution concentrated in vacuum. The solid was purified by column chromatography (CH_2Cl_2:Hexane, 1:1) followed by crystallization on pentane/methanol o give a red solid (677 mg, 37% yield).

^{1}H NMR (400 MHz, $CDCl_3$): δ (ppm) 0.81-0.92 (m, 13H, Cy(7H) $2CH_3$), 1.26-1.33 (d, 51H, Cy + alchilic chain), 1.34-1.57 (m, 35H, Cy), 1.72 (m, 2H, CH_2CHN), 2.19 (m, 2H, CH_2CHN), 5.17-5.22 (m, 1H, CH-N), 6.24-6.28 (d, 1H, CH=CH), 7.32 (d, 1H, CH=CH), 7.36-7.39 (d, 2H, aromatic phenyl), 7.71-7.64 (d, 2H, aromatic phenyl), 8.74-8.77 (m, 8H, aromatic perylene).

^{13}C NMR (100 MHz, $CDCl_3$): δ (ppm) 14.03, 22.50, 23.19, 26.67, 26.93, 27.50, 29.21, 31.61, 32.38, 54.84, 120.56, 123.04, 123.45, 128.26, 128.79, 131.17, 146.97.

^{29}Si NMR (79.5 MHz, $CDCl_3$): -68.23, -68.44, -68.63, -79.28. (3:3:1:1)

Elemental Analysis $C_{82}H_{118}N_2O_{16}Si_8$: found %C 62.53; %H 7.06; %N 1.78; calculated %C 62.48; %H 7.11; %N 1.67.

Mass: [M^+] 1672 (FAB^+)

^{1}H NMR (400 MHz, $CDCl_3$):

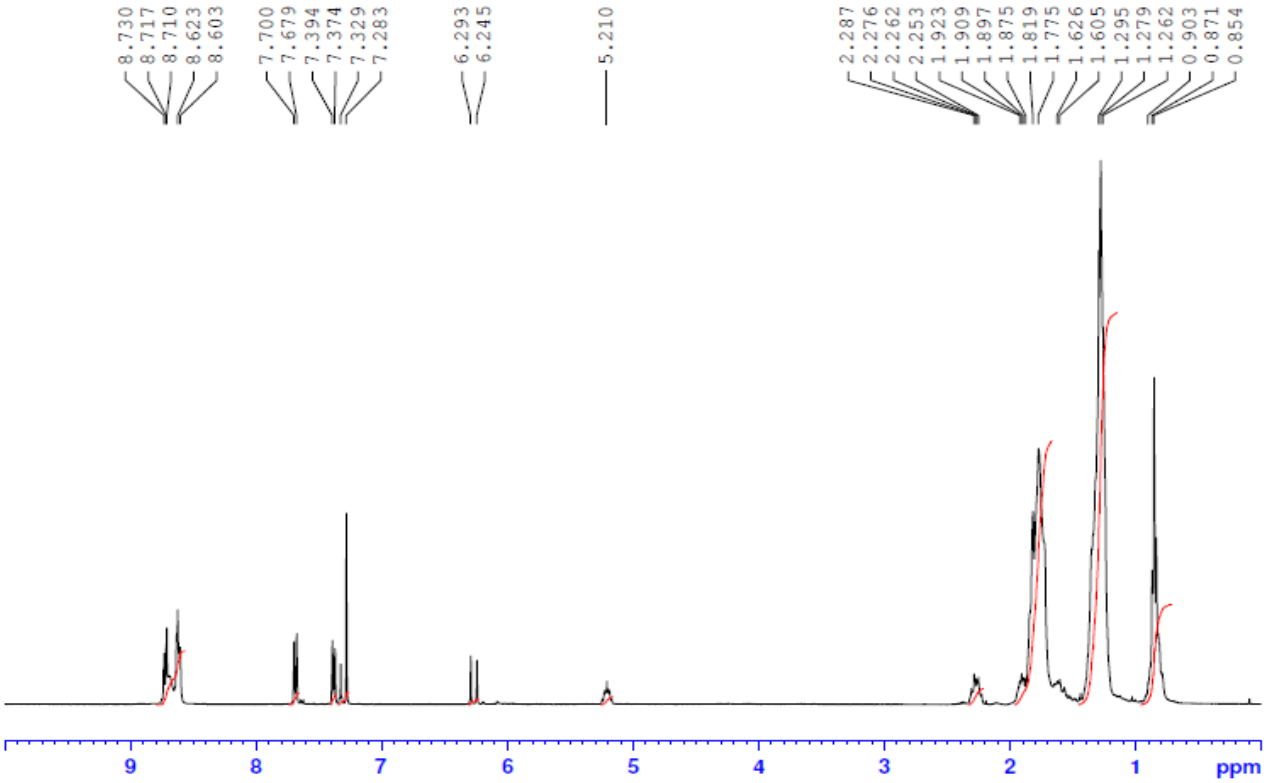

^{13}C NMR (100 MHz, $CDCl_3$):

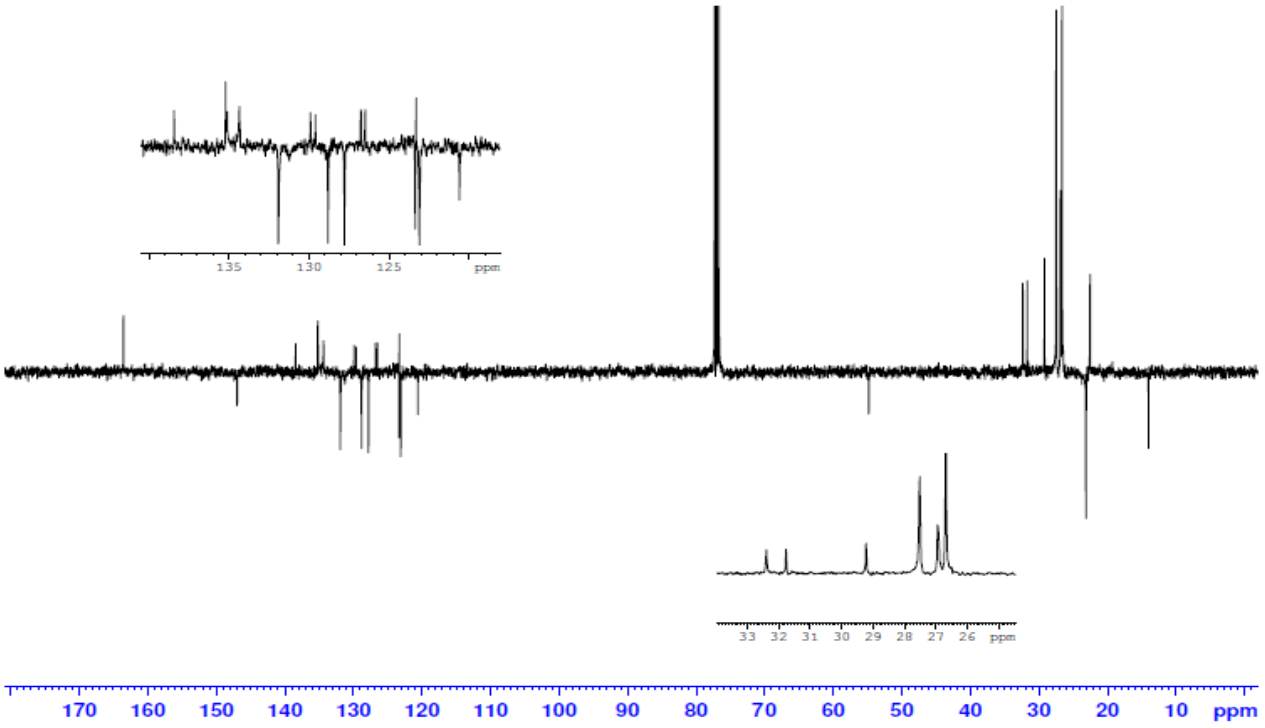

^{29}Si NMR (79.5 MHz, $CDCl_3$):

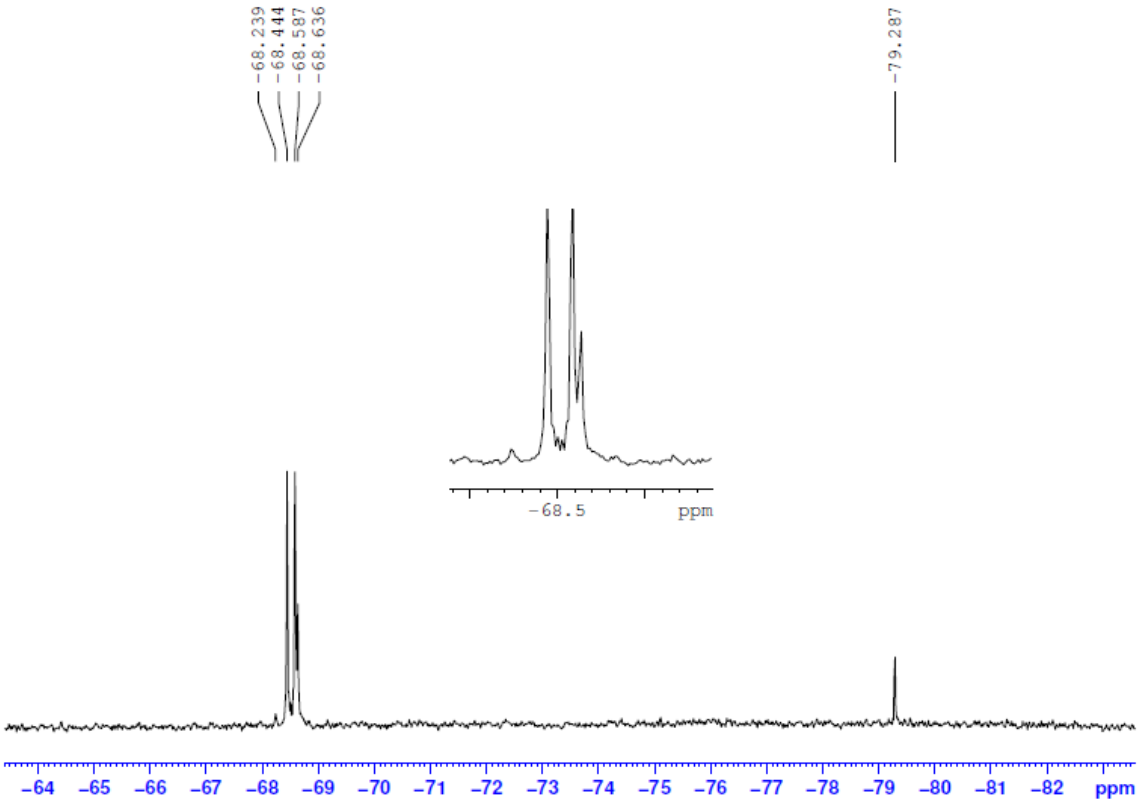

5.7 References

[1] V. Balzani, S. Campagna (Eds.), "Photochemistry and Photophysics of Coordination Compounds" Parts I & II, Topics in Current Chemistry, Volumes 280 and 281, Springer, Berlin, Heidelberg, Germany, 2007.

[2] (a) L.R. Dalton, P.A. Sullivan, D.H. Bale *Chem. Rev.* **2010**, *110*, 25; (b) P.A. Sullivan, L.R. Dalton *Acc. Chem. Res.* **2010**, *43*, 10.

[3] S. Xiao, M. Nguyen, X. Gong, Y. Cao, H. Wu, D. Moses, A.J. Heeger *Adv. Funct. Mater.* **2003**, *13*, 25.

[4] (a) M.Y. Lo, C. Zhen, M. Lauters, G.E. Jabbour, A. Sellinger *J. Am. Chem. Soc.* **2007**, *129*, 5808. (b) X. Yang, J.D. Froehlich, H.S. Chae, S. Li, A. Mochizuki, G.E. Jabbour *Adv. Funct. Mater.* **2009**, *19*, 2623.

[5] M. Kardos, *Chem. Abstr.* **1914**, *8*, 22317

[6] M. Kardos, *Chem. Abstr.* **1915**, *9*, 6398

[7] W. A. Fisher in *Pigment Handbook Volume I: Properties and Economics*, T. C. Patton (Ed.). John Wikey & Sons: New York, 1973

[8] K.-Y. Law, *Chem. Rev.* **1993**, *93*, 449.

[9] M. Sadrai, G. R. Bird, *Opt. Commun*. **1984**, *51*, 62.

[10] M. Sadrai, L. Hadel, R. R. Sauers, S. Husain, K. Krogh-Jespersen, J. D. Westbroo, G. R. Bird, *J. Phys. Chem.* **1992**, *96*, 7988.

[11]H. Suzuki, S. Hoshino, *J. Appl. Phys.* **1996**, *79*, 8816.

[12] H. Langhals, *Heterocycles* **1995**, *40*, 477

[13] Y. Nagao, *Prog. Org. Coat.* **1997**, *31*, 43.

[14] Y. Nagao, T. Naito, Y. Abe, T. Misono, *Dyes Pigm*. **1996**, *32*, 71.

[15] Y. Nagao, T. Misono, *Bull. Chem. Soc. Jpn.* **1981**, *54*, 1191.

[16] H. Kaiser, J. Lindner, H. Langhals, *Chem. Ber.* **1991**, *124*, 529.

[17] H. Tröster, *Dyes Pigm.* **1983**, *4*, 171.

[18] A. Rademacher, S. Märkle, H. Langhals, *Chem. Ber.* **1982**, *115*, 2927.

[19] Baney, R.H.; Itoh, M.; Sakakibara, A.; Suzuki, T. *Chem.Rev*. **1995**, *95*, 1409.

[20] Pescarmona, P.P.; Maschmeyer, T. *J. Aust. Chem*. **2001**, *54*, 583.

[21] Feher, F.J.; Newman, D.A.; Walzer, J.F. *J. Am. Chem. Soc*. **1989**, *111*, 1741.

[22] a) Feher, F.J.; Budzichowski, T.A.; Blanski, R.L.; Weller, K.J.; Ziller, J.W. *Organometallics* **1991**, *10*, 2526. b) Feher, F.J.; Soulivong, D.; Eklud, A.G.; Wyndham, K.D. *Chem.Commun*. **1997**, *13*, 1185.

[23] a) Feher, F.J.; Blanski, R.L. *J. Am. Chem. Soc*. **1992**, *114*, 5886. b) Severn, J.R.; Duchateau, R.; van Santen, R.A.; Ellis, D.D.; Spek, A.L. *Organometallics* **2002**, *1*, 4. c) Duchateau, R.; Abbenhuis, H.C.L.; van Santen, R.A.; Meetsma, A.; Thiele, S.K.-H.; van Tol, M.F.H. *Organometallics* **1998**, *26*, 5663. d) Hanssen, R.W.J.M.; van Santen, R.A.; Abbenhuis, H.C.L. *Eur. J. Inorg. Chem*. **2004**, *4*, 675.

[24] Maxim, N.; Magusin, P.C.M.M.; Kooyman, P.J.; van Wolput, J.H.M.C.; van Santen, R.A.; Abbenhuis, H.C.L. *Chem. Mater*. **2001**, *13*, 2958.

[25] Bonhomme, C.; Toledano, P.; Maquet, J.; Livage, J.; Bohnomme-Coury, L. *J. Chem. Soc., Dalton Trans*. **1997**, *9*, 1617.

[26] a) Bassindale, A.R.; Pourny, M.; Taylor, P.G.; Hursthouse, M.B.; Light, M.E. *Angew. Chem., Int. Ed*. **2003**, *42*, 3488; (b) Bassindale, A.R.; Parker, D.J.; Pourny, M.; Taylor, P.G.; Horton, P.N.; Hursthouse, M.B. *Organometallics* **2004**, *23*, 4400.

[27] a) Feher, F.J.; Newman, D.A.; J. Am.Chem. *J. Am. Chem. Soc*. **1990**, *112*, 1931. b) Feher, F.J.; Budzichowski, T.A.; Rahimian, K.; Ziller, J.W. *J. Am. Chem. Soc*. **1992**, *114*, 2859. c) Feher, F.J.; Philipps, S.H. *J. Organomet. Chem*. **1996**, *521*, 391.

[28] a) Shchegolikhina, O.I.; Pozdnyakova, Y.A.; Molodtsova, Y.A.; Korkin, S.D.; Bukalov, S.S.; Leites, L.A.; Lyssenko, K.A.; Peregudov, A.S.; Auner, N.; Katsoulis, D.E. *Inorg. Chem*. **2002**, *41*, 6892. b) Gavioli, G.; Battistuzzi, R.; Santi, P.; Zucchi, C.; Palyi, G.; Ugo, R.; Vizi-Orsz, A.; Shchegolikhina, O. I.; Pozdniakova, Yu. A.; Lindeman, S. V.; Zhdanov, A. A. *J. Organomet. Chem.* **1995**, *485*, 257. c) Zucchi, C.; Mattioli, M.; Cornia, A.; Fabretti, A. C.; Gavioli, G.; Pizzardi, M.; Ugo, R.; Shchegolikhina, O. I.; Zhdanov, A. A.; Palyi, G. *Inorg. Chim. Acta* **1998**, *280*, 282. d) Cornia, A.; Fabretti, A. C.; Gavioli, G.; Zucchi, C.; Pizzotti, M.; Vizi-Orosz, A.; Shchegolikhina, O. I.; Pozdniakova, Yu. A.; Pa´lyi, G. *J. Cluster Sci.* **1998**, *9*, 295.

[29] Marks, T. J.; Stair, P. C. *Top. Catal.* **2005**, *34*, 1.

[30] a)Tamaki, R.; Tanaka, Y.; Asuncion, M.Z.; Choi, J.; Laine. R.M. *J. Am. Chem. Soc*. **2001**, *123*, 12416. b)Brick, C.M.; Tamaki, R.; Kim, S.G.; Asuncion, M.Z.; Roll, M.F.; Nemoto, T.; Ouchi, Y.; Chujo, Y.; Laine, R.M. *Macromolecules* **2005**, *38*, 4655. c) Roll, M.F.; Asuncion, M.Z.; Kampf, J.; Laine, R.M. *ACS Nano* **2008**, *2*, 320.

[31] G. Li, L. Wang, H. Ni and C. U. Pittman, Jr. *J. Inorg Organome Polym.* **2001**, 11, 123.

[32] M. G. Voronkov and V. I . Lavrentyev, *Top. Curr. Chem.* **1982**, *102*, 199.

[33] Wright, J.D.; Sommerdijk, N.A.J.M. *Sol-Gel Materials: Chemicals and Application*, Taylor and Francis, London, **2001**.

[34] Choi, J.; Yee, A. F.; Laine, R. M. *Macromolecules* **2003**, *36*, 5666.

[35] Huang, J.; Xiao, Y.; Mya, K. Y.; Liu, X.; He, C.; Dai, J.; Siow, Y. P. *J. Mater. Chem.* **2004**, *14*, 2858.

[36] Imae, I.; Kawakami, Y. *J. Mater. Chem.* **2005**, *15*, 4581.

[37] Imae, I.; Kawakami, Y. *Proc. SPIE-Int. Soc. Opt. Eng.* **2005**, *5937*, 1N/1.

[38] Imae, I.; Kawakami, Y.; Ooyama, Y.; Harima, Y. *Macromol. Symp.* **2007**, *249-250*, 50.

[39] Vautravers, N. R.; Andre´, P.; Slawin, A. M. Z.; Cole-Hamilton, D. J. *Org. Biomol. Chem.* **2009**, *7*, 717.

[40] He, C.; Xiao, Y.; Huang, J.; Lin, T.; Mya, K. Y.; Zhang, X. *J. Am. Chem. Soc.* **2004**, *126*, 7792.

[41] Xiao, Y.; Tripathy, S.; Lin, T.; He, C. *J. Nanosci. Nanotechnol.* **2006**, *6*, 3882.

[42] Park, J.-J.; Lee, T.-W.; Kakimoto, M.-A.; Pu, L.-S. U.S. *Chem. Abstr.* **2007**, *146*, 261764.

[43] Sellinger, A.; Tamaki, R.; Laine, R. M.; Ueno, K.; Tanabe, H.; Williams, E.; Jabbour, G. E. *Chem. Commun.* **2005**, 3700.

[44] Lo, M. Y.; Zhen, C.; Lauters, M.; Jabbour, G. E.; Sellinger, A. *J. Am. Chem. Soc.* **2007**, *129*, 5808.

[45] Cho, H.-J.; Hwang, D.-H.; Lee, J.-I.; Jung, Y.-K.; Park, J.-H.; Lee, J.; Lee, S.-K.; Shim, H.-K. *Chem. Mater.* **2006**, *18*, 3780.

[46] Chen, K.-B.; Chang, Y.-P.; Yang, S.-H.; Hsu, C.-S. *Thin Solid Films* **2006**, *514*, 103.

[47] Cho, H.-J.; Hwang, D.-H.; Lee, J.-I.; Jung, Y.-K.; Park, J.-H.; Lee, J.; Lee, S.-K.; Shim, H.-K. *Chem. Mater.* **2006**, *18*, 3780.

[48] Hsiao, B. S.; Chu, B.; Fu, X.; Blanski, R. L.; Phillips, S. H. *Chem. Abstr.* **2003**, *138*, 107668.

[49] Ren X., Sun B., Tsai C., Tu Y., Leng S., Li K., Kang Z., Van Horn R. M., Li X., Zhu M., Wesdemiotis C., Zhang W., and Cheng S. Z. D., *J. Phys. Chem. B* **2010,** *114*, 4802.

[50] Feher, F. J.; Terroba, R.; Ziller, J. W. *Chem. Commun*. **1999**, 2309.

[51] Stockey E. G., Bolf A. G., Jones P. F., Schwab J. J., Chaffee K. P., Haddad T. S., Lichtenhan J. D., *Applied Organometallic Chemistry*, **1999**, *13*, 311.

[52] S. Demmig, H. Langhals, *Chem. Ber*. **1988**, *121*, 225.

[53] S. Nobuaki, A. Tomoyuki, *Org. Biomol. Chem.*, **2007**, *5*, 762.

[54] H. Langhals, J. Karolin, *J. Chem. Soc., Faraday Trans*., **1998**, *94*, 2919.

[55] H. Langhals, A. J. Esterbauer, *Chem. Eur. J.*, **2009**, 15, 4793.

[56] Feher, F. J.; Terroba, R.; Ziller, J. W. *Chem. Commun*. **1999**, 2309.